



ScuDo
Scuola di Dottorato - Doctoral School
WHAT YOU ARE, TAKES YOU FAR



Doctoral Dissertation
Doctoral Program in Metrology (32th Cycle)

Applications of Microwave Resonators to Thermal Metrology

Giovanni Gugliandolo

Supervisor
Prof. Vito Fericola, Supervisor

Doctoral Examination Committee:
Prof. Giovanni Crupi, Referee, University of Messina, Italy
Dr. Peter Pavlasek, Referee, Slovak Institute of Metrology, Slovakia

Politecnico di Torino
March 4, 2020

This thesis is licensed under a Creative Commons License, Attribution - Noncommercial - NoDerivative Works 4.0 International: see www.creativecommons.org. The text may be reproduced for non-commercial purposes, provided that credit is given to the original author.

I hereby declare that, the contents and organisation of this dissertation constitute my own original work and does not compromise in any way the rights of third parties, including those relating to the security of personal data.

.....

Giovanni Gugliandolo
Turin, March 4, 2020

Summary

This thesis deals with two applications of microwave sensing devices to thermal metrology. In the first case, a Whispering Gallery Mode (WGM) resonator is used as a sensor for temperature measurements. In particular, the prototype sensor is made of a cylindrical sapphire resonator hosted in a gold plated copper cavity. Two coaxial cables protrude inside the cavity exciting the whispering gallery modes of the cylindrical sapphire. The system affords a high quality factor that enables high resolution temperature measurements. This work further develops the principle of the Sapphire Whispering Gallery Thermometer (SWGT) which was developed by Strouse in 2007 [1]. It was shown that a temperature measurement uncertainty of 10 mK was achievable, albeit the sensing device exhibited some mechanical instabilities, especially at temperatures below -20 °C, so that it was not possible to use it as a thermometer without recurrent recalibrations. In this thesis the design of a new WGM resonator is reported. Its mechanical stability was improved so that the temperature working range was extended. Moreover, the quality factor of the new resonator was 90 % higher in comparison to that achieved in the earlier work. This further improved the temperature measurement resolution. The fabricated prototype was investigated in a temperature range from approximately -40 °C to 30 °C, i.e., from the triple point of mercury and the melting point of gallium. A Vector Network Analyzer (VNA) was employed for the resonant frequency estimation and an ASL F900 Precision Thermometry bridge was used for Standard Platinum Resistance Thermometer (SPRT) resistance measurement. Five different whispering gallery modes were investigated in a frequency range spanning from 6 GHz to 14 GHz, however, only the $\text{WGM}_{n=5}$ ($f = 12.25$ GHz) was chosen for temperature sensing because of the good compromise between quality factor and relative sensitivity. A fifth-order polynomial function was used as a calibration curve with sub-millikelvin residuals, approximately one order of magnitude better to that reported in the literature in the same temperature range. Measurement

reproducibility and repeatability were also investigated for such a SWGT thermometer; the estimates are 14 μ K and 0.4 mK, respectively. An uncertainty analysis is also reported in this thesis. The calibration procedure generated a combined uncertainty of 3 mK for the device under calibration. Considering the promising results obtained in this work, the SWGT confirms to be a promising alternative to platinum resistance thermometer, both as transfer standard in industrial applications and as interpolating instrument for the dissemination of the kelvin and the temperature scale.

The second microwave device described in this thesis is a sensor-integrated antenna used as sensing node for humidity measurements. The main goal of this research activity was the integration of a relative humidity sensor into a rectangular patch antenna (2.45 GHz) in order to overcome the antenna performance degradation which often occurs during the integration process: the antenna is affected by the presence of the sensor and, at the same time, the sensing performance are affected by the antenna. The main idea was to employ an aperture coupled patch antenna that ensures a weak coupling between the sensing element and the antenna itself. Two Rogers RO4003 substrates were used for this purpose: a patch antenna and a ground plane with aperture in the first substrate; a feedline and a ground plane with aperture in the other substrate. An interdigitated capacitor (IDC) was placed at the end of the feedline and a BaTiO₃ – based sensing material was deposited between its fingers. A change in the surface impedance of the deposited material (this is what happens during a water vapour exposure) is transduced into a change on the antenna resonant frequency. The frequency shift was large enough to be recorded, but not so much to detune the antenna out of its working band. Measurements were carried out inside a Thunder Scientific 2500 humidity generator between 10 %rh and 95 %rh in the temperature range from 1°C to 40 °C. The prototype sensing properties and the antenna performances are still under investigation. However, the achieved results show that this device could be used for IoT (Internet of Things) applications or as a sensing node in a Wireless Sensor Network (WSN) for environmental monitoring.

Acknowledgment

In this thesis, I would like to acknowledge different people who supported me during my PhD course. First, I would like to express the deepest appreciation to my supervisor, Professor Vito Fericola, who sustained my work and provided me everything needed to go on with my research activity. Secondly, I would like to thank Professor Krishna Naishadham from the Georgia Institute of Technology. He introduced me to the interesting research topic of sensor-integrated antennas and he supported me during my whole research activity. I hereby wish to thank Dr. Denis Smorgon, I honestly believe that his advice and guidance have had a crucial role in the improvement of my professional knowledge. Thank you to Dr. Shahin Tabandeh, a colleague and a good friend at the same time. I really have to express my gratitude to him because of his useful and constructive recommendations that improved my work. In addition, I want to say thank you to Dr. Lucia Rosso for her constant support during my activity. I say thanks to the whole staff of the thermometric building in particular Dr. Rugiada Cuccaro, Giulio Beltramino and Mauro Banfo for the help they gave to me during the last three years. I am particularly grateful for the assistance given by Dr. Giuseppina Lopardo and Roberto De Matteis. Their support in the measurement process was greatly appreciated. Special thanks should be given to Dr. Pier Paolo Capra, who assisted me from the first day of my PhD course. I am grateful for his valuable and constructive suggestions. Assistance provided by Simone Corbellini, Roberto Gavioso and Daniele Madonna Ripa, was also greatly appreciated. Furthermore, I would like to extend my gratitude to the INRiM guests with whom I shared my office, in particular Peter Rothmund from Justervesenet (Norwegian Metrology Service). With his work, he inspired and motivated me in my research activity.

Last but not the least, I would like to express my deep gratitude to Professor Nicola Donato and Professor Giovanni Neri from University of Messina for the time they spent helping me. They allowed me to work in their laboratories and use

their facilities always giving to me patient guidance and enthusiastic encouragement. I really appreciated their generous help. In particular, Professor Donato assisted me during this PhD course with his paternal help, advice and encouragement. Probably, without his assistance, I would not have reached this goal. I cannot thank him enough for his generous support.

Thank you.

*To Shahin, Lucia and
the other colleagues
who supported me in
this research.*

Contents

1. Microwave Resonators and Applications	22
1.1 Introduction	22
1.2 Microwave Resonators	25
1.3 Microwave Resonators as Sensors	27
1.3.1 Basic principles of microwave sensors	27
1.3.2 Microstrip resonators and applications	28
1.3.3 Cavity resonators and applications	30
1.3.4 Dielectric resonators and applications	30
1.3.5 Microwave Sensors: features	31
2. Thermometry based on Whispering Gallery Mode Resonators.....	34
2.1 Introduction	34
2.2 Whispering Gallery Mode Resonators	35
2.2.1 WGM theory	35
2.2.2 Sensing mechanism.....	37
2.2.3 Mode Splitting on WGM resonators.....	37
2.3 WGM Thermometry – State of The Art	41
2.4 Experimental activity.....	42
2.4.1 New Resonator design	42
2.4.2 Measurements vs. Simulations comparison.....	46
2.4.3 Experimental setup	47
VNA R&S ZNB20	48
SPRT and Fluke 1586A	48
ASL F900 Precision Thermometry Bridge.....	49
Vacuum system.....	50
2.4.4 Software developed.....	50
2.5 Measurements and Results	54

2.5.2 WGM5: calibration against SPRT	57
2.5.3 WGM resonator: calibration using a deviation function.....	59
2.5.4 WGM resonator: calibration using the thermodynamic temperature scale	64
2.5.4 SWGT resonant frequency vs. SPRT resistance.....	66
2.5.5 SWGT stability and repeatability of the ice melting point	67
2.5.6 Uncertainty Budget Analysis	70
2.6 Conclusions	71
3. Sensor-Integrated Aperture Coupled Patch Antenna for Humidity Measurements	73
3.1 Introduction	73
3.2 Antenna design and fabrication	74
3.3 Preliminary measurements	81
3.4 Sensing material synthesis.....	83
3.5 Sensing material deposition and testing	84
3.6 Data analysis.....	88
3.7 Conclusions	91
4. Conclusions and future perspectives.....	92
5. Appendix A.....	101

List of Tables

Table 1 Scattering Parameters definition	24
Table 2 Frequency range and Q factors of different microwave resonators ...	31
Table 3: WGM with $n = 2, \dots, 6$. Simulated and measured resonant frequency (f) and Q factor.....	47
Table 4 ZNB specifications from the datasheet	48
Table 5 T and T_{90} temperatures for the explored fixed points. The INRiM SPRT resistance is also reported in the table	64
Table 6 Main uncertainty contributions from the SWGT calibration. The values in the gray cells refer to the uncertainty contributions of the microwave sensor ..	70
Table 7 Uncertainty contributions due to the frequency measurements.	71
Table 8 Prototype dimensions after the optimization process.....	78
Table 9 ACP + IDC simulation, main results	78
Table 10 Comparison between the Sapphire Whispering Gallery Thermometer (SWGT) and the Standard Platinum Resistance Thermometer (SPRT)	93

List of Figures

Figure 1 Electromagnetic spectrum.....	23
Figure 2 Generic two port network	23
Figure 3 Lumped element RLC series circuit schematic	25
Figure 4 Lumped element RLC parallel circuit schematic	26
Figure 5 Working principle schematic for a microwave sensor.....	28
Figure 6 Microstrip structure. ‘ W ’ is the microstrip width, ‘ h ’ the substrate thickness, ‘ t ’ the metallization thickness and ‘ ϵ_r ’ is the substrate relative dielectric constant.	29
Figure 7 Resonators topologies working area	32
Figure 8 Whispering gallery mode in a spherical resonator.....	36
Figure 9 (a) perturbation azimuthal position; (b) resonator S_{21} magnitude at different perturbation azimuthal angles (θ) with $\varphi = 10^\circ$. The mode splitting is maximized when the perturbation is in the equatorial plane. If the particle is far from the equator, it does not interfere with the electromagnetic field and the mode splitting disappears ($\theta = 40^\circ$, $\varphi = 10^\circ$).	38
Figure 10 (a) Perturbation position along the equatorial plane. (b) Resonant peak when the particle is in the equatorial plane ($\theta = 0$). For WGM at 13.5 GHz, at $\varphi = 0^\circ, 30^\circ, 60^\circ, 90^\circ$, the mode splitting disappears.	39
Figure 11 Mode splitting with the perturbation in the equatorial plane and $0^\circ < \varphi < 30^\circ$	40
Figure 12 Mode splitting at different perturbation size ($\varphi = 10^\circ$; $\theta = 0^\circ$)	40
Figure 13 Resonator cavity: old design with a central body and two disks	42
Figure 14 New cavity design, 3D model.....	43
Figure 15 Copper cavities before the coaxial cables soldering and gold plating	44
Figure 16 Copper cavity after its fabrication. Before the gold plating procedure, the copper cavity was nickel plated in order to improve the gold adhesion on copper.	

All the external edges were rounded to avoid the gold detachment from the cavity and so the copper oxidation. The three panels in this picture report three different views of the cavity: **(a)** bottom part of the hollow body with the cap; **(b)** top part of the cavity; **(c)** 17.6-mm cylindrical sapphire placed inside the cavity.44

Figure 17 Measurements acquired at different antennas size: (a) S_{21} magnitude as a function of the antennas length; (b) Quality Factor as a function of the antennas length.46

Figure 18 CST Simulation Results: electric energy densities at resonances. Five different WGMs are considered in this work: **(a)** WGM $n = 2$; **(b)** WGM $n = 3$; **(c)** WGM $n = 4$; **(d)** WGM $n = 5$; **(e)** WGM $n = 6$47

Figure 19 WGM resonator and SPRT inside the bath. The WGM resonator is suspended for the vibrations rejection.47

Figure 20 INRiM SPRT used in the experiment. The last 50 mm were inserted in the cavity metal block.....49

Figure 21 ASL F900 with the temperature-controlled reference resistance ...50

Figure 22 GUI for ASL F900 python program51

Figure 23 Plots displayed by the ZNB20 software. Acquisition of the WGM $_n=2$ at 6.58 GHz.....52

Figure 24 Lorentzian fitting algorithm performances: (a) the S_{21} magnitude acquired with the VNA and the fitted functions are reported in this plot, they are well over imposed; (b) The lorentzian fitting residuals for the real and imaginary part are reported in this graph. They are always less than 4×10^{-5} in magnitude....53

Figure 25 Telegram bot with data regarding two measurement sessions54

Figure 26 Measurements made on five different WGMs in the temperature range $-40\text{ }^\circ\text{C} / 0\text{ }^\circ\text{C}$. **(a)** Fractional change as a function of the temperature; **(b)** Quality Factor change with temperature, the highest Q factor is associated with the WGM5 ($f = 12.2\text{ GHz}$).....55

Figure 27 SPRT standard deviation at different temperatures (a), resonant frequency standard deviation as a function of temperature (b).56

Figure 28 Fifth order polynomial calibration curve in the temperature range from $-40\text{ }^\circ\text{C}$ to $30\text{ }^\circ\text{C}$57

Figure 29 Calibration fit residuals. As shown in the plot, in the considered range they are always within $\pm 600\text{ }\mu\text{K}$ 57

Figure 30 Standard deviation of the SPRT measurements. During the experiment, the SPRT was placed inside the copper block through the designed hole.....58

Figure 31 Standard deviation of the WGM frequency measurements at each temperature step.....58

Figure 32 Sapphire permittivity as a function of temperature. Third-order fitting performed on Egorov and Volovikov data.	60
Figure 33 Sapphire thermal expansion coefficient along the crystallographic z-axis as a function of temperature. Third-order fitting on White raw data, a subrange of White measurements is considered.	61
Figure 34 Comparison between the measured (Calibration function) and calculated (Reference function) normalized frequency shift.	62
Figure 35 Difference between Calibration function and Reference function .	62
Figure 36 SWGT residuals when a deviation function is used for the calibration	63
Figure 37(a) Differences between thermodynamic temperatures and the ITS-90. In (b) a subrange is reported. Data published in [62].	65
Figure 38 The estimated values of $T-T_{90}$ are compared with the estimations reported in the literature by J. Fischer and R. Underwood	66
Figure 39 Residuals from the SWGT resonant frequency vs SPRT resistance fitting. The SPRT resistance in the plot was expressed in terms of its corresponding temperature in order to improve the legibility of the plot. The residuals were converted in temperature as well by considering the SWGT sensitivity to temperature variations.....	67
Figure 40 SWGT resonance frequency and quality factor deviations with the resonator placed inside the melting ice bath	68
Figure 41 SWGT inside the dewar with melting ice	68
Figure 42 SWGT and SPRT stability comparison	69
Figure 43 SWGT and SPRT measurement repeatability comparison	70
Figure 44 Side view and top view of an ACP antenna coupled to a microstrip line	75
Figure 45 ACP Antenna in the computer simulator (3D exploded view)	76
Figure 46 Simulation results: Electric energy density on rectangular patch and IDC at 2.45 GHz. The electric energy density is higher along the patch radiator boundaries and the feedline. On the contrary, its value is low between the IDC fingers because of the weak coupling.	77
Figure 47 IDC + ACP antenna 3D model, bottom view (left) and top view (right)	78
Figure 48 Integrated IDC dimensions	79
Figure 49 Fabricated prototype. Top view and bottom view of each board. ..	79
Figure 50 ACP Antenna into its plastic frame. The two screws A and B move the antenna substrate along the y direction. Screws C and D move the antenna along	

the x direction. Screws E, F, G, H are used to stop the two substrates in the position chosen.	80
Figure 51 Simulated and measured $ S_{11} $ at resonance (2.45 GHz).	80
Figure 52 Simulated and measured S_{11} phase at resonance (2.45 GHz)	81
Figure 53 IDC + ACP frequency shift at different humidity concentrations. The shift is relative to the resonant frequency in dry air (0 %rh). This test was carried out at room temperature (24 °C)	82
Figure 54 Experimental setup for the temperature measurements.	82
Figure 55 Antenna frequency shift, test at different temperatures. Measurements performed without any sensing material deposited on the IDC	83
Figure 56 SEM and TEM analysis of the $\text{BaTiO}(\text{C}_2\text{O}_4)_2/\text{CO}(\text{NH}_2)_2$ nanoparticles	84
Figure 57 BaTiO_3 nano-powder between the fingers of the IDC.....	85
Figure 58 Resonant frequency shift for different humidity concentration values. Measurements carried out at 23 °C.....	85
Figure 59 Resonant frequency shift for different humidity concentration values. Measurements carried out at 10 °C.....	86
Figure 60 Resonant frequency shift for different humidity concentration values. Measurements carried out at 30 °C.....	87
Figure 61 Resonant frequency shift for different humidity concentration values. Measurements carried out at 40 °C.....	87
Figure 62 Sensing mechanism schematic.....	88
Figure 63 Frequency shift as a function of relative humidity. Each line represents the sensor response at different temperatures. Experimental data fits very good with an exponential function.....	89
Figure 64 Frequency shift as a function of the operating temperature. Each color represents the sensor response at different relative humidity values.....	89
Figure 65 Resonance frequency variations as a function of relative humidity and temperature. A two dimensional calibration function was used to describe the sensor behavior.	90
Figure 66 The calibration fit residuals reported in the graph are within ± 0.1 MHz. This value corresponds to approximately 1 %rh ($T = 40$ °C, %rh > 40 %).	90
Figure 67 Number of connected devices (billions) between 2014 and 2022. Data from www.ericsson.com	94

List of symbols

a	<i>Sapphire disk diameter</i>
c	<i>Speed of light in vacuum</i>
C	<i>Capacity</i>
E_l	<i>Energy loss per second</i>
E_r	<i>Percentage error</i>
E_s	<i>Average energy stored</i>
f	<i>Frequency</i>
f_0	<i>Resonant frequency</i>
h	<i>Substrate high</i>
Im	<i>Imaginary part</i>
k	<i>Coverage factor</i>
L	<i>Inductance</i>
l	<i>Whispering gallery mode number (radial direction)</i>
L_a	<i>Substrate length</i>
L_h	<i>Cylindrical sapphire disk height</i>
m	<i>Whispering gallery mode number (polar direction)</i>
n	<i>Whispering gallery mode number (azimuthal direction)</i>
P	<i>Partial pressure</i>
P_s	<i>Saturation pressure</i>
Q	<i>Quality factor</i>
R	<i>Resistance</i>
r	<i>Radial direction</i>

Re	<i>Real part</i>
S_d	<i>Deviation function</i>
S_m	<i>Calibration function</i>
S_s	<i>Reference function</i>
$S_{SWG T}$	<i>SWG T temperature sensitivity</i>
T	<i>Temperature</i>
$\tan\delta$	<i>Loss tangent</i>
W_a	<i>Substrate width</i>
x_f	<i>Fitting value</i>
x_m	<i>Measured value</i>
Z	<i>Impedance</i>
Δf	<i>Frequency shift</i>
ΔT_{SPRT}	<i>SPRT temperature variation</i>
$\Delta\omega$	<i>-3dB Bandwidth $\cdot 2\pi$</i>
ϵ_1	<i>Sapphire dielectric constant along z axis</i>
ϵ_0	<i>Vacuum permittivity</i>
ϵ_{eff}	<i>Effective dielectric constant</i>
ϵ_r	<i>Permittivity</i>
$\epsilon(f)$	<i>Complex permittivity</i>
$\epsilon_r'(f)$	<i>Relative dielectric constant</i>
$\epsilon_r''(f)$	<i>Relative loss factor</i>
ϵ_{\perp}	<i>Sapphire dielectric constant along x and y axis</i>
θ	<i>Azimuthal direction</i>
λ	<i>Wavelength</i>
σ_{bath}	<i>Standard deviation bath temperature measurements</i>
σ_f	<i>Standard deviation frequency measurements</i>
ϕ	<i>Polar direction</i>
ω	<i>Angular frequency</i>

List of acronyms

<i>BC</i>	<i>Before Christ</i>
<i>ACP</i>	<i>Aperture Coupled Patch</i>
<i>AM</i>	<i>Amplitude Modulation</i>
<i>CNC</i>	<i>Computer Numerical Control</i>
<i>CNT</i>	<i>Carbon Nanotube</i>
<i>EM</i>	<i>Electromagnetic</i>
<i>FEM</i>	<i>Finite Element Method</i>
<i>FM</i>	<i>Frequency Modulation</i>
<i>IDC</i>	<i>Interdigitated Capacitor</i>
<i>INRIM</i>	<i>Istituto Nazionale di Ricerca Metrologica</i>
<i>ISM</i>	<i>Industrial, Scientific and Medical</i>
<i>ITS-90</i>	<i>International Temperature Scale of 1990</i>
<i>MOM</i>	<i>Method of Moments</i>
<i>MUT</i>	<i>Material Under Test</i>
<i>NPL</i>	<i>National Physical Laboratory</i>
<i>PCB</i>	<i>Printed Circuit Board</i>
<i>PID</i>	<i>Proportional-Integral-Derivative</i>
<i>PRT</i>	<i>Platinum Resistance Thermometer</i>
<i>RF</i>	<i>Radio Frequency</i>
<i>RMSE</i>	<i>Root Mean Squared Error</i>
<i>SEM</i>	<i>Scanning Electron Microscope</i>
<i>SMA</i>	<i>SubMiniature version A</i>

<i>SOLT</i>	<i>Short, Open, Load, Thru</i>
<i>SPRT</i>	<i>Standard Platinum Resistance Thermometer</i>
<i>SQUID</i>	<i>Superconducting Quantum Interference Device</i>
<i>SWGT</i>	<i>Sapphire Whispering Gallery Thermometer</i>
<i>TE</i>	<i>Transverse Electric</i>
<i>TEM</i>	<i>Transverse Electro-Magnetic</i>
<i>TM</i>	<i>Transverse Magnetic</i>
<i>UHF</i>	<i>Ultra High Frequency</i>
<i>VHF</i>	<i>Very High Frequency</i>
<i>VNA</i>	<i>Vector Network Analyzer</i>
<i>WGM</i>	<i>Whispering Gallery Mode</i>
<i>WSN</i>	<i>Wireless Sensor Network</i>

Chapter 1

Microwave Resonators and Applications

1.1 Introduction

Since ancient times, people showed interest on electricity and electromagnetism. In 6th century BC, Thales of Miletus, a Greek philosopher, studied the static electricity. He observed how rubbed amber was able to attract small objects like hairs. In 1690, Christiaan Huygens published “Treatise on Light” in which he described for the first time the wave theory of light. A great improvement on electromagnetic theory was given in 1865 by James Clerk Maxwell with the paper entitled “A Dynamical Theory of the Electromagnetic Field” in which he unified electricity, magnetism and light. In this work he described the electromagnetic radiation in which the electric and magnetic field are coupled each other travelling together as waves with a certain speed that he estimated to be 310,740,000 m/s. In 1888, Heinrich Hertz was able to produce and detect microwaves in the UHF band by using the first antenna prototype. He observed how the radio waves can travel through some materials and, on the contrary, can be reflected by others. With his experiments he explained some electromagnetic properties like refraction, reflection, polarization and interference.

At the beginning of the development of modern microwave techniques [2], only the lower part of microwave spectrum was exploited because of the limited number of applications. When the scientific community became more confident with radio waves, the lower range of RF spectrum started to be saturated and the need of wider bandwidth was absolutely essential. At the same time, international conventions on the frequency spectrum were established. It was only during the World War II that microwave techniques received a great improvement with the development of radar equipments and in wireless communications. In recent years, the microwave techniques have been characterized by a continuous development in RF solid state

devices and integrated circuits. Their applications spread over different field such as wireless communications, networking, sensing and security [3].

As the working frequency increases, the wavelength decreases as:

$$\lambda = \frac{c}{\sqrt{\epsilon_r f}} \quad (1.1)$$

Where c is the speed of light in vacuum, ϵ_r is the permittivity of the medium in which the wave is propagating, f is the working frequency. Above certain frequencies, the size of the components used becomes comparable to the wavelength so that the lumped element approximation is not valid anymore because voltage and current vary in amplitude and phase along the circuit. The *Transmission Line Theory* gives the right tools to study such cases. Still, the frequency at which the microwave range starts is not defined uniquely, however in literature [2] it is usual to start speaking about microwaves at that frequencies in which the lumped element circuit approximation is not valid anymore. Usually this happens for frequencies above 1 GHz. On the contrary, the ending part of the microwave spectrum corresponds to that frequencies for which optical techniques must be used to describe the signal transmission.

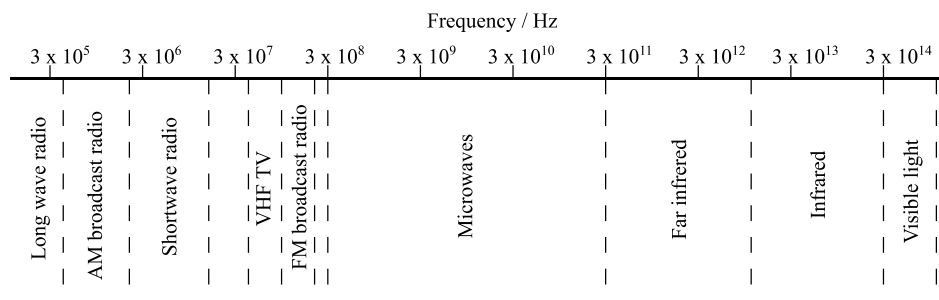


Figure 1 Electromagnetic spectrum

At low frequency, every electrical network can be fully defined by voltage and current at its input and output port. The z , y , g and h parameters are defined for this purpose. Similarly, at high frequency, a transmission line can be employed with reasonable simplicity considering the energy flow through its ports. As instance, let's consider a simple two port network as shown in figure 1.

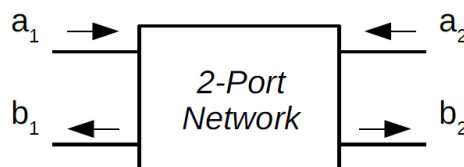


Figure 2 Generic two port network

It is possible to define at each port i an incident wave (a_i) and a reflected wave (b_i), so that:

$$\begin{cases} b_1 = a_1 S_{11} + a_2 S_{12} \\ b_2 = a_1 S_{21} + a_2 S_{22} \end{cases} \quad (1.2)$$

Or in matrix form:

$$\begin{bmatrix} b_1 \\ b_2 \end{bmatrix} = \begin{bmatrix} S_{11} & S_{12} \\ S_{21} & S_{22} \end{bmatrix} \begin{bmatrix} a_1 \\ a_2 \end{bmatrix} \quad (1.3)$$

The network is so described by a $[S]$ matrix that is called Scattering Matrix. The terms S_{ij} are called scattering parameters, they are complex numbers and are defined as reported in Table 1.1:

Table 1 Scattering Parameters definition

$S_{11} = \left. \frac{b_1}{a_1} \right _{a_2=0}$	Reflection coefficient at port 1 when port 2 is terminated with matched load ($a_2 = 0$)
$S_{12} = \left. \frac{b_1}{a_2} \right _{a_1=0}$	Reverse transmission coefficient when port 1 is terminated with matched load ($a_1 = 0$). It represents the attenuation of wave travelling from port 1 to port 2.
$S_{21} = \left. \frac{b_2}{a_1} \right _{a_2=0}$	Forward transmission coefficient when port 2 is terminated with matched load ($a_2 = 0$). It represents the attenuation of wave travelling from port 1 to port 2
$S_{22} = \left. \frac{b_2}{a_2} \right _{a_1=0}$	Reflection coefficient at port 2 when port 1 is terminated with matched load ($a_1 = 0$)

The parameters S_{11} and S_{22} are defined as the ratio between reflected wave and incident wave at each port when there is no incident wave at the opposite port (matched load). They are called reflection coefficients at port 1 and port 2 respectively. The parameters S_{21} and S_{12} are defined as the ratio between the reflected wave at the not excited port ($a_i = 0$) and the incident wave at the opposite port. They are called forward and reverse transmission coefficients respectively. Components and networks at microwave range are usually described by the scattering matrix. These parameters can be calculated using the network analysis techniques or measured directly with a Vector Network Analyzer (VNA).

1.2 Microwave Resonators

One of the most used microwave devices are the microwave resonators. They are employed in the design of filters, frequency meters, oscillators and tuned amplifiers.

The resonance phenomenon was firstly observed by Galileo Galilei in 1638. As he wrote in “Dialogues Concerning Two New Sciences” [4]:

“Even as a boy, I observed that one man alone by giving these impulses at the right instant was able to ring a bell so large that when four, or even six, men seized the rope and tried to stop it they were lifted from the ground, all of them together being unable to counterbalance the momentum which a single man, by properly-timed pulls, had given it”.

However, Galileo Galilei is not considered as the man that discovered the resonance phenomenon, but certainly he is the pioneer of the scientific research behind it [5].

The working principle of a microwave resonator is similar to that of lumped element resonant circuit: at a certain frequency the network impedance changes so that the energy coming from the generator is completely transmitted/absorbed or reflected by the network itself. For a lumped-element RLC series circuit (Figure 2) the input impedance can be written as [3]:

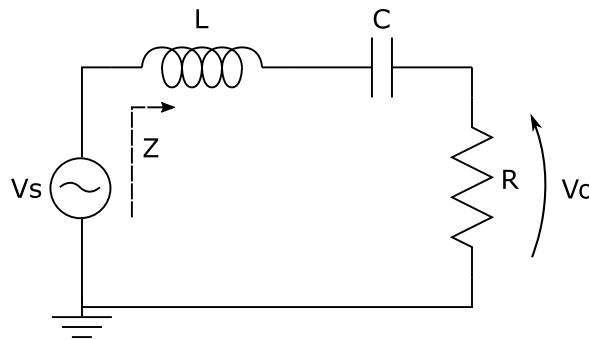


Figure 3 Lumped element RLC series circuit schematic

$$Z = j\omega L + \frac{1}{j\omega C} + R = R + j\omega L \left(1 - \frac{1}{\omega^2 LC}\right) \quad (1.3)$$

At resonance, the impedance is purely real. This occurs when $\text{Im}(Z) = 0$ or $\omega = \pm \frac{1}{\sqrt{LC}}$, the impedance reaches its minimum value.

In order to understand the resonance phenomenon and the cancellation of the reactive components, it is worth to note that the capacitor and inductor voltages are

always shifted by 180°: when one reactance is dropping, the other is increasing. Resonance occurs when the two magnitudes are the same [6], or:

$$\omega L = \frac{1}{\omega C} \quad (1.4)$$

The dual principle is valid for the Lumped-Element RLC parallel circuit. In this case (Figure 1.4) the role of voltages and currents are interchanged and, at resonant frequency, the admittance reaches its minimum value. Usually, the resonance in the case of a parallel RLC circuit is called antiresonance.

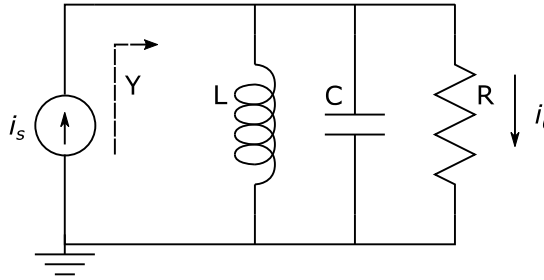


Figure 4 Lumped element RLC parallel circuit schematic

An important parameter that characterizes a resonator is the quality factor (Q). It is a measure of the resonator losses and is defined as [3]:

$$Q = \omega \frac{E_s}{E_l} \quad (1.5)$$

Where E_s is the average energy stored and E_l is the energy loss per second due to dielectric, conductor and radiation losses. It is possible to prove [3] that the quality factor can be expressed as:

$$Q = \frac{\omega_0}{\Delta\omega} \quad (1.6)$$

Where $\Delta\omega$ is the half-power bandwidth of the resonator and ω_0 is angular resonant frequency. This quality factor does not take into account the loading effect caused by the connected circuit. When the loading effect is included the Q is called *loaded* Quality Factor (Q_L).

At microwave range, it is not possible to describe a network as a lumped-element circuit. This is the reason why at high frequency resonators are described using the transmission line theory. However, at frequencies near resonance, a microwave resonator can usually be modelled by either a series or parallel RLC lumped-element equivalent circuit. So there are:

- short circuited $\lambda/2$ line, can be modelled as a series RLC circuit;
- short circuited $\lambda/4$ line, can be modelled as a parallel RLC circuit;

- open circuited $\lambda/2$ line, can be modelled as a parallel RLC circuit.

All of them can be studied as lumped element circuits with an equivalent value of R, L and C [3].

1.3 Microwave Resonators as Sensors

1.3.1 Basic principles of microwave sensors

Microwave resonators are commonly employed for accurate measurements of electromagnetic properties in dielectric materials like permittivity, loss tangent and surface impedance [7]. Moreover, they can be also employed as sensors of different physical quantities that affect the complex permittivity or the dielectric losses of the Material Under Test (MUT).

Microwave sensors firstly appeared in the 60's, but their development was slow. During the last twenty-five years the design of microwave sensors has been facilitated by the improvement of microwave components that become smaller, faster and cheaper [8]. Today microwave sensors are used for a variety of applications in the industry, medicine, and for research purposes. They are based on the interaction of microwaves with matter. This interaction may be in the form of reflection, refraction, scattering, emission, absorption, or change of speed and phase.

When an electric field is applied across a dielectric material, the atomic charges and molecular dipoles in the dielectric are displaced from their equilibrium positions and the material is said to be polarized. Dielectric analysis involves the determination of this polarization in materials subjected to a time varying electric field.

The permittivity is the main dielectric parameter and represents the measurements of the maximum dipolar polarization that can be attained by the material under specific condition (temperature, chemical state, etc.). The permittivity is a frequency-dependent complex number with following expression [9]:

$$\varepsilon(f) = \varepsilon_0(\varepsilon_r'(f) - j\varepsilon_r''(f)) \quad (1.8)$$

where:

- f is the frequency;
- ε_0 is a constant, which represents the vacuum permittivity;
- the real part $\varepsilon_r'(f)$ is known as the *relative dielectric constant*, which characterizes the material's ability to store and release electromagnetic energy;

- the imaginary part $\epsilon_r''(f)$ is known as the *relative loss factor*, which characterizes the material's ability to absorb (attenuate) electromagnetic energy to create heat.

Microwave sensors are based on the fact that electromagnetic waves are very sensitive to the dielectric properties of the material in which they exist. The interaction between microwaves and the medium of propagation is completely determined by the medium dielectric properties.

The range of applicability of these sensors is very large because dielectric properties are also sensitive indicators of numerous physical and chemical properties of the material, such as the moisture content, temperature, biomass, density, bacterial content, chemical reaction and composition, viscosity and many other properties [8].

A generic schematic for a measurement setup of a microwave sensor is reported in Figure 5.

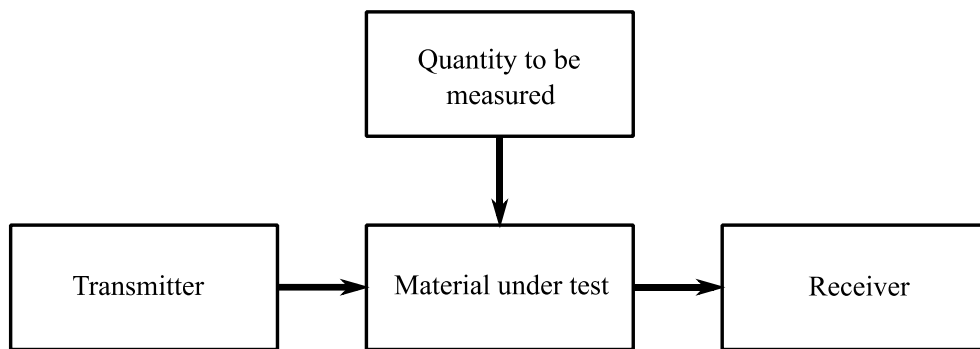


Figure 5 Working principle schematic for a microwave sensor

The majority of microwave sensors are characterized by a transmitter that generates the input signal, the MUT whose dielectric properties are affected by the quantity to be measured (gas, temperature, force...) and a receiver. Usually, instead of transmitter and receiver, a VNA is used for the determination of the material dielectric properties. The resonant frequency is strongly linked to the resonator geometry and the material permittivity, so that a variation in the resonant frequency can be related to a variation on the physical quantity that affects the MUT.

1.3.2 Microstrip resonators and applications

During last few years, several topologies of microstrip resonators were studied as antennas, filters or in sensing applications.

The microstrip is one of the most used transmission line in microwave applications. It is preferred to other transmission lines because of its low cost and good performance. Many microwave components such as antennas, filters, resonators can be realized with this technology. The disadvantages of microstrip

compared with other transmission lines (i.e., waveguides) are its lower power handling capacity and higher losses.

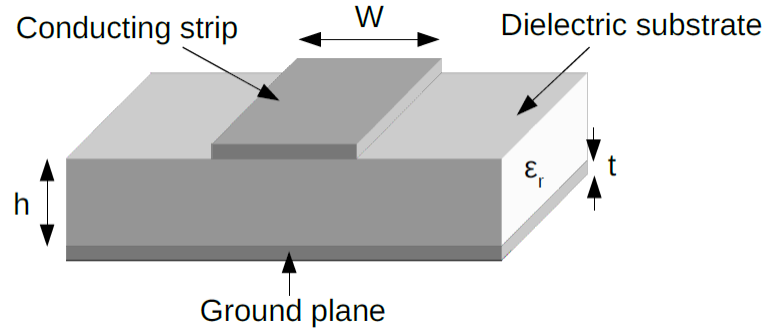


Figure 6 Microstrip structure. ' W ' is the microstrip width, ' h ' the substrate thickness, ' t ' the metallization thickness and ' ϵ_r ' is the substrate relative dielectric constant.

The geometry of a microstrip line is shown in Figure 6. It is made by a conductive ground plane on the bottom part, a dielectric layer of thickness h and dielectric constant ϵ_r in the middle and, finally, a conductive strip on the top. In the microstrip structure, the electric field lines go from the upper conductor to the ground plane passing through air and the dielectric material. The presence of two different materials (dielectric and air), complicates the study of microstrip line. However, in most of the cases, the dielectric thickness is very small compared to the wavelength ($h \ll \lambda$) so that the field distribution is very similar to the DC case. Instead of considering a dielectric-air interface in the field path, it is possible to consider the material uniform with an effective dielectric constant that satisfies the relation [3]:

$$1 < \epsilon_{eff} < \epsilon_r \quad (1.9)$$

It is possible to estimate the ϵ_{eff} from the ϵ_r value and the microstrip geometry. Formulas for such approximation are reported in [3].

Sensors based on microstrip resonators are preferred for less accurate and low cost applications. Rectangular, circular, triangular, disk sectors, rings are examples of geometries employed for the resonator design. Most of the time, they are capacitively coupled to a microstrip line that is connected to an excitation source like a signal generator or a transmitter. They can be realized using the same technology employed in the fabrication of Printed Circuit Boards (PCBs) and can be easily assembled into an electronic board or coupled to a patch antenna. Due to these advantages they are widely used in sensing applications, especially in gas detection [10], [11]. Generally, the working principle of a microstrip gas sensor is based on a change in the effective permittivity of a sensitive material covering part of a microwave resonator. When the target gas is adsorbed on the material surface, the effective permittivity changes and a variation in the resonant frequency is observed [12].

One of the most interesting microstrip sensors advantages is that they are fully compatible with the wireless technology. Especially during last few years, in which the wireless communications are spreading over and over in our everyday life, they are employed in wireless sensor networks as part of sensing nodes in environmental monitoring, industrial measurements, and security/medical applications. In these cases, a combination between a sensor and an antenna is needed for the wireless sensing node design and, most of the time, they are both fabricated using the same technology. Typically, they are made on the same substrate using the microstrip technology because of a relatively low cost and the easier fabrication process (photolithography). The design, fabrication and testing of a sensor-integrated antenna prototype is discussed in Chapter 3 of this thesis.

1.3.3 Cavity resonators and applications

A microwave resonator can also be made by waveguides of different shape and size [3]. Usually, they are closed at both ends (short circuited) forming the so called “resonant cavity”. The electromagnetic field energy is stored inside the closed box and different resonant modes can be established inside the cavity. The coupling is usually made through a small aperture in the conductive walls or using a probe or a loop as an antenna. Simple geometries like cylinder or sphere are well studied [13] and the analytical solution that provides all the modes inside the cavity is known. For other unusual geometries, no analytical solution is reported in literature so the Maxwell equations have to be solved with the right boundary conditions in order to calculate the cavity resonances. Usually this procedure is made numerically by a computer software using the Method of Moments (MoMs) or the Finite Element Method (FEM). A detailed description of this two different approaches can be found in [14]–[17].

Cavity resonators are used in gas detection [18] and for displacement measurements [19]. An interesting application of a cavity resonator is the “quasi-spherical resonator” used to measure the permittivity of a binary mixture of gases. From the permittivity value it is possible to calculate the polarizability of the mixture and so, the polarizability of the gas under test. A more detailed description of this instrument can be found in [20].

1.3.4 Dielectric resonators and applications

Dielectric materials can also be used as microwave resonators [3]. The working principle of such resonators is similar to that of cavities. High permittivities are typically employed in order to confine the electromagnetic field inside the dielectric shape. Conductor losses are absent because there are not metallic walls, but a small part of electromagnetic field propagates outside the resonator. This effect is known as field fringing and is the cause of radiation loss and a consequent worsening of

the resonator quality factor. This is the reason why dielectric materials with low losses are usually employed for the design and fabrication of such resonators.

Dielectric resonators are usually used as displacement sensors [21], crack detectors [22] and for liquid and gas detection [23], [24]. Usually, simple geometries like cubic or cylinder are employed because their electromagnetic behaviour is widely described in literature [13].

An important sub-category of dielectric resonators is represented by Whispering Gallery Mode (WGM) resonators. Their high stability and high quality factor make them useful in several fields like in oscillators development or in sensing applications. WGM resonators are used for force measurements, in gas detection and bio-sensing [24]–[31]. Moreover, they were successfully employed in the past for temperature measurements [1], [32] with a measurement uncertainty better than 10 mK. A more detailed discussion of Whispering Gallery Mode resonators is reported in Chapter 2 of this thesis.

1.3.5 Microwave Sensors: features

Mazierska *et al.* in his paper [7] summarised different microwave resonators according to the resonant frequency range and the Q factor (Table 1). According to his study [7], microstrip resonators have a Q factor of the order of few hundreds and they are usually employed at room temperature. Working at low temperatures, the Q factor can be increased by several orders of magnitude by employing whispering gallery modes (WGM) excited in low loss dielectric resonators made of sapphire [6]. These kind of resonators provide a very high Q factor that makes them one of the most sensitive electromagnetic instruments [7].

Table 2 Frequency range and Q factors of different microwave resonators

Resonator type	Frequency	Q-factor
Microstrip resonator	500 MHz – 10 GHz	100 – 300
Cavity Resonators	6 GHz – 40 GHz	$10^4 - 4 \times 10^4$
Cavity made of superconductor (T < 20 K)	6 GHz – 40 GHz	$10^8 - 10^{10}$
Dielectric resonators	1 GHz – 20 GHz	$10^4 - 5 \times 10^4$
WGM sapphire resonators	8 GHz – 50 GHz	$10^5 - 10^{10}$

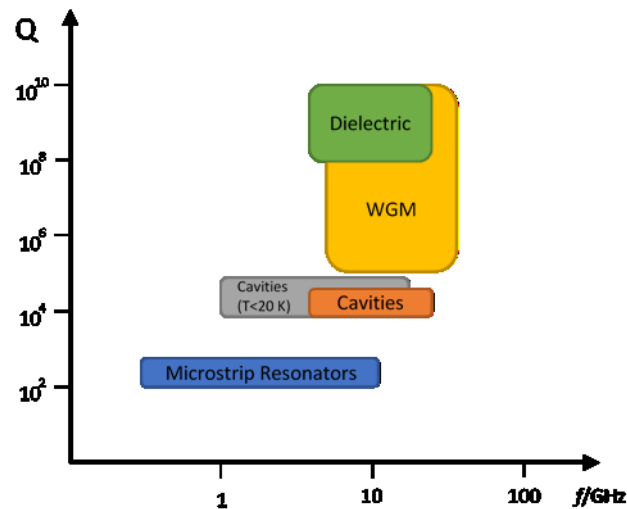


Figure 7 Resonators topologies working area

The most important advantages of employing microwave technology in sensing applications are listed below [33].

- for some configurations, microwave sensors do not need mechanical contact with the MUT;
- microwave energy penetrates all materials except for metals. The measured result therefore represents a volume of the MUT, not only the surface;
- microwave resonator sensors are inherently stable because the resonant frequency is related to the physical dimensions;
- at low frequencies (capacitive and resistive sensors), the dc conductivity often dominates the electrical properties of a material. The dc conductivity depends strongly on temperature and ion content. At microwave frequencies, the influence of the dc conductivity often disappears;
- at the power levels used for measurements with microwave sensors, microwaves are safe for the operator (contrary to radioactive radiation);
- the response of the microwave sensor to a change in the MUT is almost immediate;
- manufacturing cost of microwave sensors is generally not high.

However, there may be some disadvantages:

- the higher is the frequency, the more expensive are the electronic components;
- microwave sensors must be calibrated separately for different materials;
- the sensors are often adapted to a specific application, resulting in low universal applicability;
- due to the cells size and the wavelength of the microwave signals, the spatial resolution with microwave sensors is low;

- the sensors are sensitive to more than one variable. Additional sensors are therefore in some cases necessary for compensation.

These disadvantages have limited the applications of microwave sensors.

Chapter 2

Thermometry based on Whispering Gallery Mode Resonators

2.1 Introduction

The scope of the work described in this chapter is to exploit a microwave resonator as a thermometer, to evaluate its metrological performance and make a comparison with the Standard Platinum Resistance Thermometer (SPRT), the reference thermometer in precision industrial and scientific applications.

The Platinum Resistance Thermometer (PRT) was introduced for the first time in 1887 by Professor H. L. Callendar with the paper entitled “On the Practical Measurement of Temperature” [34], [35]. Before that time, the mercury thermometer was the instrument used for temperature measurement, it was fragile and had a very limited working range. In 1871, C. W. Siemens proposed the first resistance thermometer as an instrument able to measure temperature up to 1000°C. After the Callendar’s studies, the PRTs were employed in blast furnaces, annealing furnaces (1892) and later in chemical industry, food production and environmental control systems. The standard PRT (SPRT) is a special PRT used in for highly accurate laboratory measurements. It is used as the interpolating instruments for the realization and dissemination of the International Temperature Scale of 1990 (ITS-90). Still today, with the new definition of the kelvin, the SPRT is the reference thermometer in metrological and industrial applications. However, the SPRTs suffer from some limitations: they are sensitive to vibrations, mechanical shocks and thermal stress. Consequently, they need periodic recalibrations. Moreover, in some fields like aerospace, chemistry or weather stations, a measurement uncertainty less than 10 mK is often required [1], but this level of accuracy is hard to reach outside a laboratory using a platinum resistance thermometer.

Because of these limitations, other topologies of thermometers were investigated based on photonics [36] or microwave [1], [32]. In particular, an optical thermometer with nano-kelvin resolution is described in [38]. In this article,

the authors were able to employ an isotropic crystalline whispering gallery mode resonator to measure temperature with a resolution of $80 \text{ nK}/\sqrt{\text{Hz}}$. Another approach to measure the temperature with high resolution is reported in [37]. In this case, a superconducting quantum interference device (SQUID) magnetometer is employed as a nano-kelvin resolution thermometer. Although its performance in temperature measurements and its small size, this device can be used only at low temperature ($\sim 3 \text{ K}$) and it is not able to cover the SPRT temperature range.

In this thesis, a whispering gallery mode microwave resonator was developed for temperature measurements. Its performance as a thermometer was investigated and compared to that of SPRT finding very promising results. The resonator exhibited a temperature resolution better than $15 \text{ }\mu\text{K}$ and a measurement stability and repeatability five times better than a SPRT. Compared to the optical resonator previously described [38], the coupling in a microwave whispering gallery mode resonator is easier since a metallic antenna can be employed to excite the modes. Furthermore, the resonator roughness is not so stringent as required in optical resonators [39].

In the next sections of this chapter the microwave resonator design and its fabrication are described. Two calibration techniques are also reported with the associated uncertainty analysis. Finally, the developed thermometer is compared with the classical SPRT.

2.2 Whispering Gallery Mode Resonators

2.2.1 WGM theory

The St Paul's Cathedral in London is not famous only for its architecture and rich history, but also for of an exclusive feature that makes it unique: the whispering gallery that runs along the interior wall of its dome [40]. When weak sounds are generated close to the dome wall, the mechanical waves propagate through the walls and start to circulate many times before fading away. As a result, these sounds are audible to the opposite side of the dome. Several explanations were given to this physical phenomenon, but only in late 1870s John William Strutt, also known as Lord Rayleigh, described for the first time the Whispering Gallery Waves in his Theory of Sounds [41]. From a geometrical point of view [42], such waves are guided by means of repeated reflections which, neglecting losses, continue *ad infinitum* with no end. However, acoustic whispering gallery waves have no practical application because of the cavity size needed to sustain such acoustic modes. In 1961, Garrett *et al.* [43] observed whispering gallery modes in optical wavelength range where the resonator size could be reduced to the micrometer level. Nowadays, ultra-high Q Whispering Gallery Mode Resonators are employed as oscillators, filters or sensors. Moreover, they are receiving increasing attention due to their high potentials in quantum informatics, novel micro/nano sources, dynamic filters and in micro/nano sensors [44].

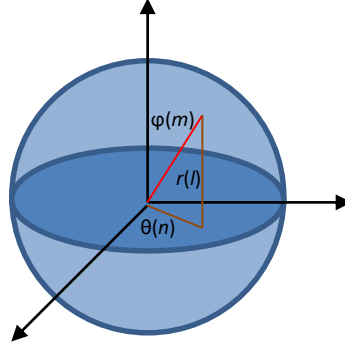


Figure 8 Whispering gallery mode in a spherical resonator

Microwave Whispering Gallery Mode (WGM) resonators are the main topic of this chapter. They are made by low loss dielectric material with a rotational symmetry like sphere or cylinder. In such geometries, the electromagnetic (EM) wave is trapped in a circular orbit very close to the external surface and circulate along the inner surface with small losses. As reported in the literature [44], WGMs in spherical coordinates are characterized by three mode numbers: l , n and m , which represent the radial, azimuthal and polar mode numbers, respectively. The mode number l is equal to the number of field maxima in the radial direction (r) of the sphere. The value $2n$ is equal to the number of field maxima in the azimuthal direction (θ) in the equatorial plane, and, finally, the value of $(n-m+1)$ indicates the number of field maxima in the polar direction (ϕ) around the equator.

Resonant frequencies for a spherical WGM resonator can be found by solving the following transcendental equation [42]:

$$\frac{[n_h x y_l(n_h x)]'}{y_l(n_h x)} = N \frac{[n_r x j_l(n_r x)]'}{j_l(n_r x)}, \quad (2.1)$$

where:

- $j_l(x)$ and $y_l(x)$ are spherical Bessel functions of the first and second kind
- $x = n_h \omega_0 R / c$ is called size parameter;
- R is the resonator radius;
- n_r and n_h are the dielectric refractive indexes of the resonator and the host medium respectively;
- c is the speed of light;
- N is a constant whose value depends on the mode polarization. $N=1$ for transverse electric (TE) polarized modes, $N = n_h^2 / n_r^2$ for transverse magnetic (TM) polarized modes.

As stated by Foreman in [42], an exact analytic solution of Eq 2.1 (or its analog in cylindrical or other highly symmetric systems) is generally not possible, so that resonances frequencies must be calculated either numerically or by means of analytical approximations. However, what is important to note from Eq. 2.1 is that it depends on the resonator size and its dielectric properties so, it is possible to claim

that resonances are set by the dielectric properties of the resonator and its environment and the resonator size [42]. Even if several analytical approximations were given for the whispering gallery problem, the use of such equations is limited. Approaches based on finite element methods are also prominent in the literature. Especially during the last few years, FEM simulations are improving their flexibility and accuracy with an increasing interest in their use for optimization of the WGM resonators geometry.

2.2.2 Sensing mechanism

As described for a generic microwave sensor (see Chapter 1), the working principle for a WGM sensor is to monitor its spectral properties that can be affected by some physical changes on its surface or close to it. As an example, a variation in the WGM resonances can be due to a change in pressure, temperature or by the introduction of gas into the resonator environment. The sensing principle is to record the resonance frequency shift induced by such physical changes.

Shifts in the WGM resonant frequency occur when the resonator size or refractive index varies. Actually, a frequency shift can be observed even if only the refractive index of the host material is changing. This behavior is due to the evanescent tail of WGM that extend in the environment outside the resonator dielectric material. A change in the host refractive index determines a change in the effective refractive index seen by the WGM along its path.

2.2.3 Mode Splitting on WGM resonators

Because of their physical properties, WGMs can be excited only inside cavities with a perfect rotational symmetry along one axis, like spheres, cylinders, rings. At resonance, two independent WGMs propagate in two opposite directions along the resonator inner surface accumulating the same phase shift thus creating a single resonance peak in the resonator spectrum. However, when the geometrical symmetry is broken, for example, because of a perturbation in the resonator surface, a reflected wave is produced coupling the two counter-propagating modes and introducing a difference in the two-phase shifts. As a consequence, the single resonant peak is divided into two different peaks. If their distance is of the order of their bandwidth, their spectrum is distorted lowering the resonator Q factor. This phenomenon is known as “mode-splitting” [45], [46]. Pierre-Yves Bourgeois and Vincent Giordano [45] developed a mathematical model for the description of the mode splitting effect in a WGM resonator. According to their studies, the coupling factors of the two modes depend on the angular position of the coupling probes and of the dominant perturbation causing the mode splitting. This means that for certain angles, the coupling can be eliminated or, at least, minimized reducing the mode splitting effect. The results obtained by Bourgeois and Giordano were confirmed by the FEM simulations performed in this thesis. Similarly to their work, a crystal

sapphire was considered as WGM resonators. A rod sapphire was placed inside a cylindrical metal cavity with two diametrically opposed antennas acting as exciting probes. A perturbation was included in the 3D model and several simulations were performed with the particle moving along the resonator surface. In particular, the perturbation included in the simulation was a hole in the sapphire surface with a diameter of $80\ \mu\text{m}$. The mode splitting is strongly dependent on the particle position, for certain angles it is negligible and one peak prevails on the other, for other particle angles, the mode splitting effect is maximized and a clear separation appears between the two peaks. For instance, Figure 9 (b) shows the microwave resonator spectrum when the perturbation is moving along the azimuthal direction (a). It is evident that the mode splitting effect is emphasized when the perturbation is along the equatorial plane, the area in which the EM field is maximum. For higher azimuthal angles, the perturbation is moved to regions in which the field amplitude is low and so the mode splitting becomes negligible.

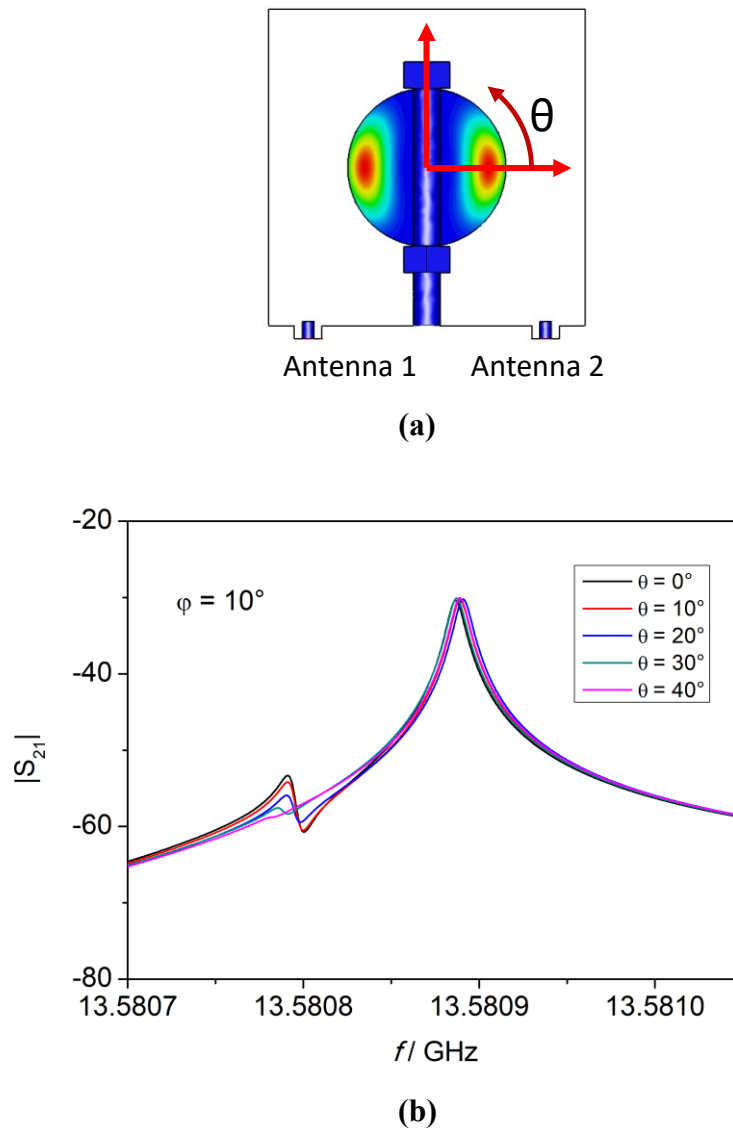


Figure 9 (a) perturbation azimuthal position; (b) resonator S_{21} magnitude at different perturbation azimuthal angles (θ) with $\varphi = 10^\circ$. The mode splitting is maximized when the perturbation is in the equatorial

plane. If the particle is far from the equator, it does not interfere with the electromagnetic field and the mode splitting disappears ($\theta = 40^\circ$, $\varphi = 10^\circ$).

The FEM simulations confirmed that for certain angles, even if the perturbation is in the equatorial plane, the mode splitting effect disappears. In Figure 10 the field distribution (a) and the spectrum (b) of a WGM at $f = 13.5$ GHz are reported. The mode splitting becomes negligible for $\varphi \in [0^\circ, 30^\circ, 60^\circ, 90^\circ]$, or for $\varphi = a_0 \cdot \pi/6$. In other words, the mode splitting effect disappears when the particle is placed close to the E-field maximum or minimum. For a generic WGM it is possible to claim that this angle is equal to:

$$\varphi = a_0 \frac{\pi}{2n}. \quad (2.2)$$

Where a_0 is an integer. For odd a_0 values a frequency shift was observed in the resonator spectrum.

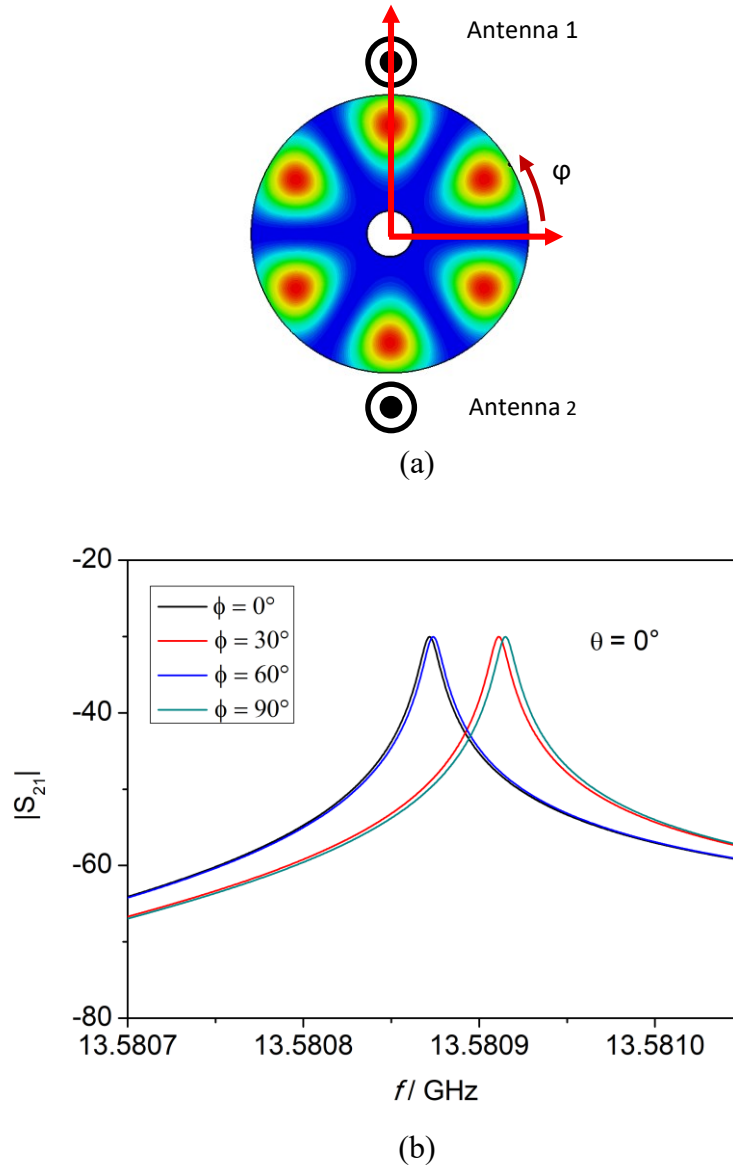


Figure 10 (a) Perturbation position along the equatorial plane. (b) Resonant peak when the particle is in the equatorial plane ($\theta = 0$). For WGM at 13.5 GHz, at $\varphi = 0^\circ, 30^\circ, 60^\circ, 90^\circ$, the mode splitting disappears.

Figure 11 reports the transmission coefficient (S_{21}) of the spherical sapphire resonator when the perturbation angular position is between 0° and 30° . For these ϕ angles, the mode splitting effect is not negligible.

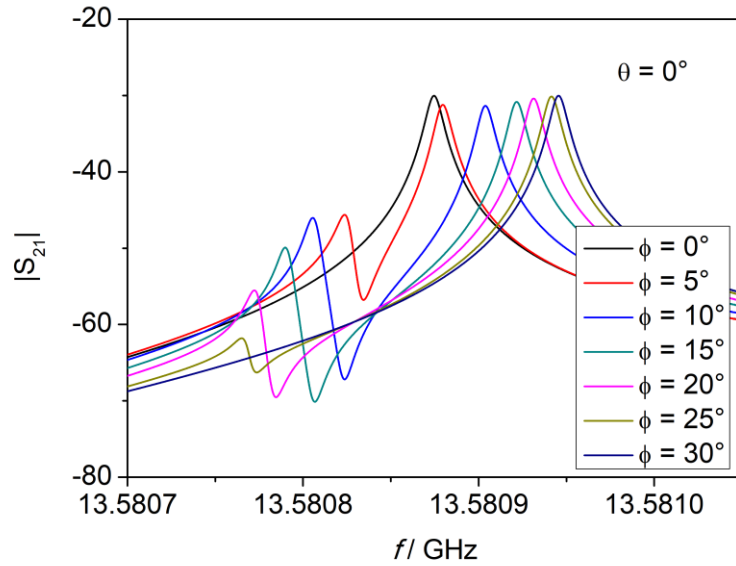


Figure 11 Mode splitting with the perturbation in the equatorial plane and $0^\circ < \phi < 30^\circ$.

Finally, some simulations were carried out with different perturbation size. If the perturbation size is small, it can be stated that the related impedance is reasonably small. On the contrary, a bigger perturbation can be represented by a larger impedance. If the presence of a bigger hole is simulated along the equatorial surface, the mode splitting effect is emphasized. On the contrary, for a smaller perturbation, the amplitude of one peak is always less respect to the other (Figure 12).

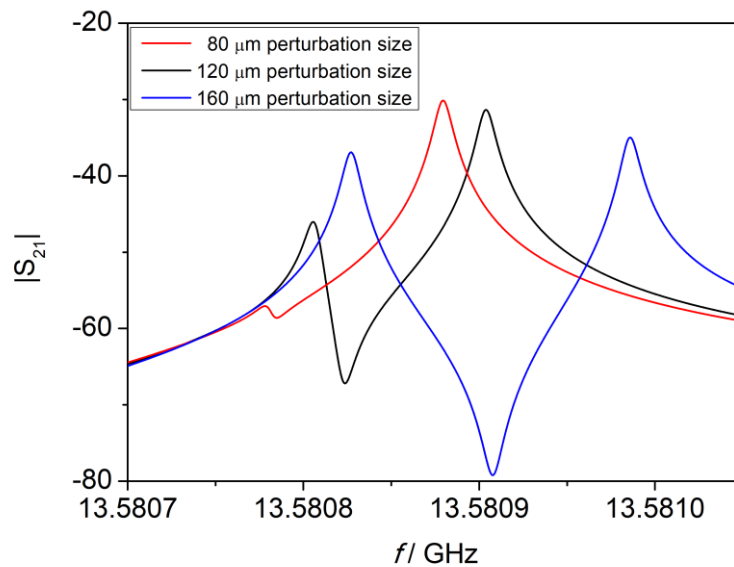


Figure 12 Mode splitting at different perturbation size ($\phi = 10^\circ$; $\theta = 0^\circ$)

The simulations confirmed the study of Bourgeois and Giordano [45]: the mode splitting effect is strongly related to the surface roughness. If a perturbation is present on the resonator surface, the mode splitting effect takes place. However, it can be minimized by rotating the resonator along its axis with an angular position given by eq. 2.2. Bourgeois and Giordano claimed that the case of more perturbations along the resonator surface can be studied as a unique equivalent perturbation. Simulation of such cases is not reported in this thesis because they are still under investigation.

2.3 WGM Thermometry – State of The Art

The first Sapphire Whispering Gallery Thermometer (SWGT) was developed by Strouse in 2007 [1]. He employed a monocrystalline sapphire disk as a dielectric resonator with whispering gallery modes in the bandwidth (14 – 20) GHz and with a quality factor (Q) as large as 90000. After the calibration procedure, Strouse's prototype was able to measure temperature in the range from 0 °C to 100 °C with a standard uncertainty of 10 mK ($k = 1$) [1]. According to Strouse and Tobar's studies, in a monocrystalline sapphire disk the frequency vs temperature dependence due to the thermal coefficient of the sapphire dielectric constant can be expressed as follows [1], [47]:

$$\frac{1}{f_0} \frac{\partial f_0}{\partial T} = \frac{1}{f_0} \left(\frac{\partial f_0}{\partial \varepsilon_{\perp}} \frac{\partial \varepsilon_{\perp}}{\partial T} + \frac{\partial f_0}{\partial \varepsilon_{\parallel}} \frac{\partial \varepsilon_{\parallel}}{\partial T} + \frac{\partial f_0}{\partial L_h} \frac{\partial L_h}{\partial T} + \frac{\partial f_0}{\partial a} \frac{\partial a}{\partial T} \right), \quad (2.2)$$

where:

- f_0 is the resonance frequency,
- T is the temperature,
- ε_{\perp} and ε_{\parallel} are the permittivities in the radial and axial direction respectively,
- L_h is the sapphire disk height and a is the disk diameter.

The fractional frequency change with temperature was estimated to be 40-to-70 ppm/K [48]–[50]. The frequency shift is due on one side to the temperature dependence of the sapphire permittivity, on the other side to the thermal expansion. However, the latter is one order of magnitude less respect to the first contribution [1], [49]–[51].

In 2012, Yu and Fernicola [32] developed a spherical-sapphire-based WGM resonator. Their prototype was based on a 12-mm spherical sapphire dielectric resonator and the whispering gallery mode at 13.6 GHz was explored in a temperature range from -40 °C to 85 °C. In this case, the quality factor was estimated to be 82000 with a measurement uncertainty better than 10 mK ($k = 1$). According to the literature [1], the SWGT is a good alternative to the PRT because of its smaller uncertainty in temperature measurements. However, still the main

limitation of these resonators is their mechanical instability [46]. If the sapphire is shifted from its equilibrium position or tilted, for example, because of thermal expansion mechanical stress, the resonator symmetry is broken, the resonator behavior is affected and it is not possible anymore to use it as a thermometer without a new calibration. Because of this important limitation, a new resonator design is needed in order to improve the SWGT performances.

In this chapter, the design, fabrication and testing of a new SWGT are reported. It is based on a 17.6-mm cylindrical sapphire resonator, similar to that exploited by Strouse in [1]. In order to improve the resonator mechanical stability, a new design for the copper cavity was given. Five whispering gallery modes were explored in the band (6 – 14) GHz in a temperature range from -40 °C to 0 °C. A bigger dielectric resonator made it possible to have a quality factor (>250000) higher than that previously measured by Strouse [1] and Yu [48]. By using the new cavity design, no mechanical instabilities were recorded even at the lowest investigated temperatures (e.g., -40 °C) where the thermal stress affects the resonator response [46]. The measurement standard uncertainty was evaluated to be 3 mK ($k = 1$) while the thermometer resolution was approximately 14 μ K.

2.4 Experimental activity

2.4.1 New Resonator design

Strouse and Yu's resonator designs are very similar: the crystal sapphire is suspended through a screw in the center of a copper cylindrical cavity. According to numerical optimizations [48], the cavity inner diameter and height are about twice the sapphire diameter. As shown in Figure 13, it is made by a central hollow body and two disks. Two coaxial cables protrude from one disk for the excitation of the whispering gallery modes. A vacuum pipe is also included in the design. The central body and the two disks are bolted together and sealed with two O-Ring gaskets.



Figure 13 Resonator cavity: old design with a central body and two disks

However, this configuration suffers from some mechanical instabilities especially at low temperatures ($< -20\text{ }^{\circ}\text{C}$). As highlighted by Ramella *et al.* in [46] the two main critical aspects of the design are the cavity assembly and the sapphire mounting. The authors claimed that the adoption of separate pieces bolted together to create the cavity, may lead to body-disks misalignments as a consequence of thermal expansion. This is equivalent to a shift of the sapphire resonator from the geometrical center of the cavity. According to these studies, even more critical is the different thermal expansion between the sapphire holding screw and the cavity. In this case the mechanical stress due to the different thermal expansion leads to small sapphire tilts respect to the cavity's vertical axis thus changing the frequency separation between two whispering gallery modes. This is reasonable because a tilt in the spherical sapphire changes the relative position of the main perturbation respect to the whispering gallery standing wave: the mode splitting is affected, a frequency shift of the main peak occurs (see Figure 11) and a recalibration is needed.

The new cavity design proposed in this thesis takes into account these issues trying to solve them. The issue related to the cavity assembly, that generates horizontal shifts in the sapphire position, was solved by designing the cavity's central body and the disk holding the crystal sapphire as a unique object. In this way, no bolts and O-Ring gaskets are needed and no mechanical movements are allowed. With this geometry the sensor assembly reproducibility is improved as well. As regards the sapphire tilts, they were reduced considering a holding screw that penetrates deeply inside the copper cavity. The new resonator design is depicted in Figure 14.

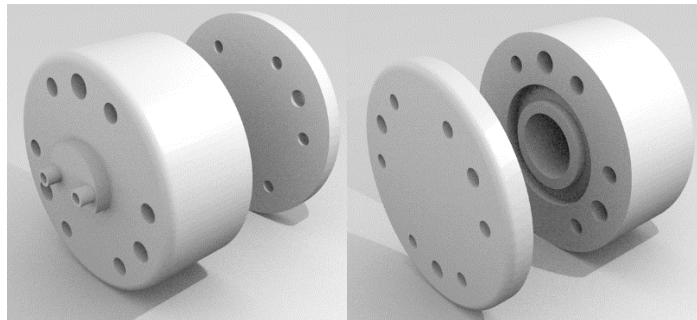


Figure 14 New cavity design, 3D model

Other smaller improvements were included in the new cavity design, such as:

- Six through-bolts instead of bolts in threaded holes ensure a better vacuum-sealing;
- Three additional 7-mm holes allow hosting SPRTs during the calibration procedure measuring the resonator temperature and, at the same time, giving an estimation of the temperature uniformity of the copper block;
- Two collars facilitate the soldering process of the coaxial cables.

The cavity design was made with Solidworks by Dassult Sistemes. Two kinds of cavities were designed, one smaller to host a 12-mm spherical/cylindrical sapphire, the other one bigger in order to host a 17.6-mm cylindrical sapphire. The cavities drawings are reported in Appendix A. After their validation, the drawings have been sent to the manufacturer for fabrication. They were realized starting from a unique copper block. After their first machining, a vacuum pipe and two coaxial cables were soldered in each cavity. In particular, before soldering, the coaxial cables were cut so that the inner connectors protrude inside the cavity by 6 mm acting as antennas. On the other side the coaxial cables were vacuum sealed with a Stycast Epoxy to avoid leakages through the cables and, finally, RF SMA connectors were soldered.

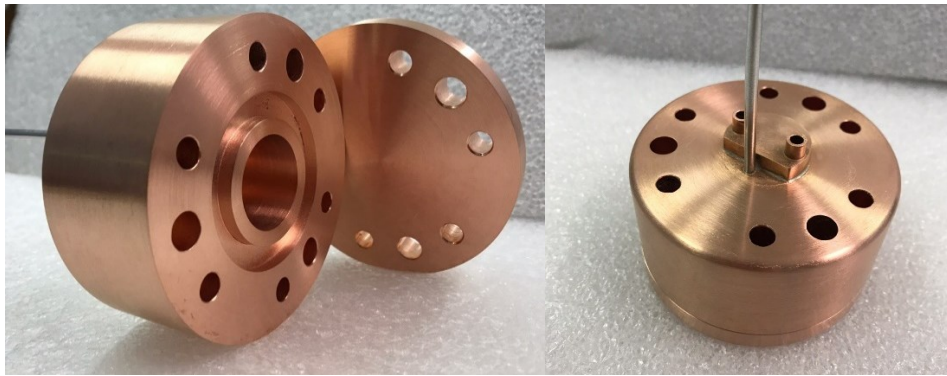


Figure 15 Copper cavities before the coaxial cables soldering and gold plating

After these assemblies, the cavities were polished, nickered and gold plated in order to avoid the copper oxidation. The nickel layer was needed to improve the gold adhesion on copper. The average gold thickness in the cavities was greater than 10 μm . The vacuum sealing was finally tested with a leak detector for all the fabricated cavities. Figure 16 shows the final resonator assembly.

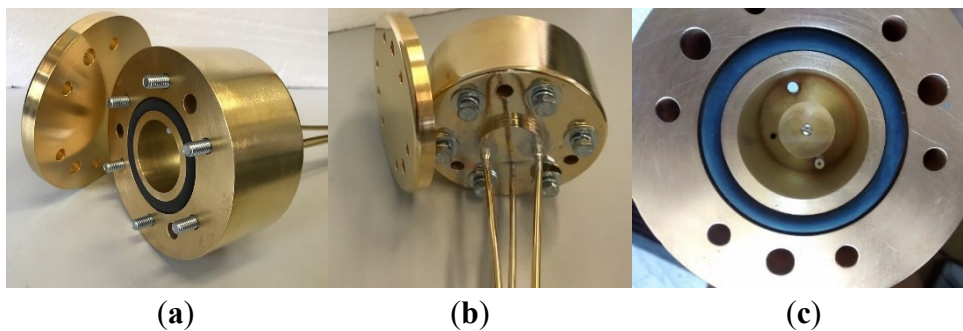
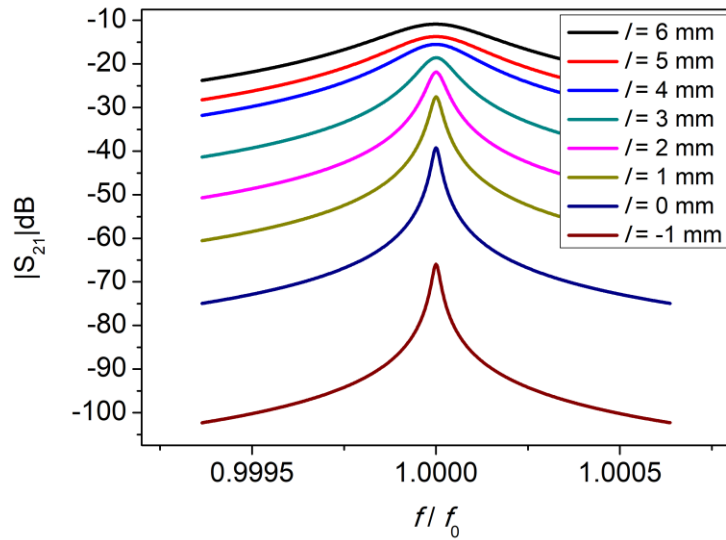


Figure 16 Copper cavity after its fabrication. Before the gold plating procedure, the copper cavity was nickel plated in order to improve the gold adhesion on copper. All the external edges were rounded to avoid the gold detachment from the cavity and so the copper oxidation. The three panels in this picture report three different views of the cavity: (a) bottom part of the hollow body with the cap; (b) top part of the cavity; (c) 17.6-mm cylindrical sapphire placed inside the cavity.

According to computer simulations, the sapphire resonator Q factor is maximized when the antenna length is minimum. The cavity design has two 6 mm antennas that, after the sapphire resonator placement, were cut in order to optimize the Q factor and the coupling. According to simulations, for long antennas, the coupling is high but the Q factor is low; on the other hand, if the antennas length is reduced, the coupling decreases but the resonant peak is sharp (i.e., higher Q factor). In Figure 17, the transmission parameter (S_{21}) is plotted at different antennas lengths (l). The antennae size was reduced from 6 mm to 0 mm in seven different steps. One more measurement was performed with the antennas 1 mm below the cavity base, this measurement is identified with $l = -1$ mm. As depicted in Figure 17, the Q factor remains lower than 20 % of its maximum value for $l > 4$ mm, then it starts to increase quite linearly with the antenna length reaching its maximum at $l = -1$ mm. For lower l no resonant peaks were recorded. As regards the peak amplitude, it is evident from Figure 17 how it becomes very small by decreasing l . Because of this issue, the final antenna size could not be so small: a value for l close to 0.5 mm was chosen as a good compromise between Q factor and peak amplitude.



(a)

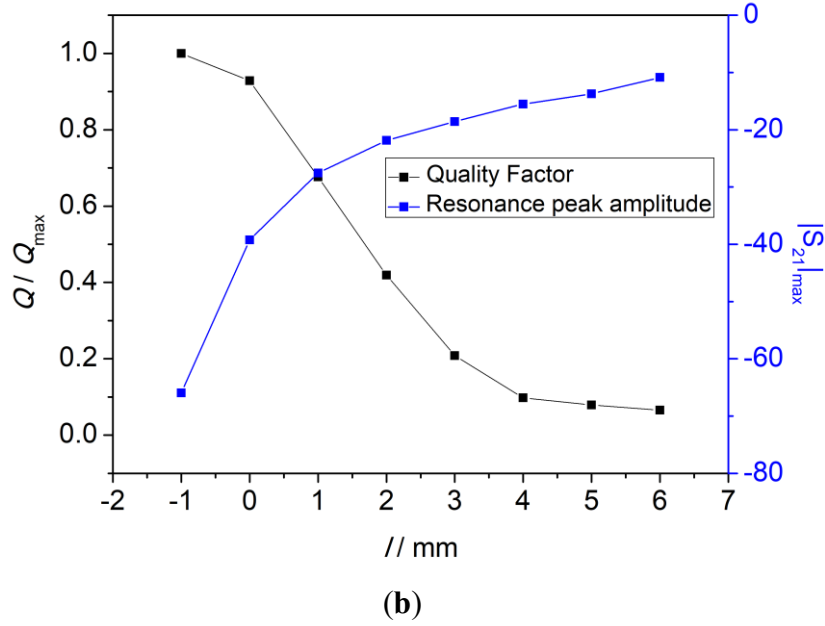


Figure 17 Measurements acquired at different antennas size: (a) S_{21} magnitude as a function of the antennas length; (b) Quality Factor as a function of the antennas length.

2.4.2 Measurements vs. Simulations comparison

A 3D model of the 17.6-mm cylindrical SWGT was built in CST Studio Suite in order to identify the whispering gallery resonances. The cavity was designed as a cylindrical object ($\epsilon_r = 1$, $\mu_r = 1$) with gold (*lossy*) along the external surface as a boundary condition. A cylindrical anisotropic sapphire with the same dimensions of that used in this thesis was placed inside with a permittivity of 9.391 along the x and y-axis, and 11.5869 along the z-axis [48]. The loss tangent was set to 1.45×10^{-5} in the x and y-axis, 6.05×10^{-6} along the z-axis [52]. Two waveguide ports were created in the 3D model simulating the presence of the two antennas. A good agreement between measurements and simulation has been observed in the resonant frequencies. The simulated Q factors are in a good agreement as well except for $\text{WGM}_{n=2}$ ($f = 6.5$ GHz). A comparison of these values is reported in Table 3. Figure 18 shows the electric energy densities at the resonant frequencies: the electric field is confined in a region close to the external surface and its distribution is the typical distribution of whispering gallery modes. From the number of E-field maxima (red regions in Figure 18) it is possible to determinate the order (n) of WGM.

Table 3: WGM with $n = 2, \dots, 6$. Simulated and measured resonant frequency (f) and Q factor.

WGM	f / GHz (sim. / meas.)	Q (sim. / meas.)
$n = 2$	6.580 / 6.581	88703 / 39690.6
$n = 3$	8.482 / 8.487	120890 / 111700.5
$n = 4$	10.375 / 10.383	141020 / 158276.7
$n = 5$	12.263 / 12.251	152130 / 173442.2
$n = 6$	14.121 / 14.105	151945 / 164025.3

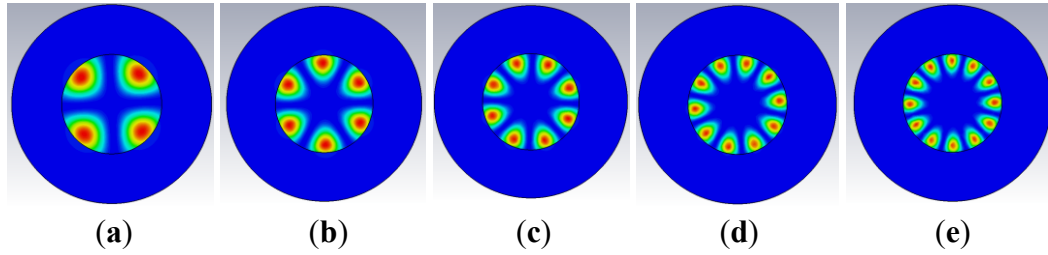


Figure 18 CST Simulation Results: electric energy densities at resonances. Five different WGMs are considered in this work: (a) WGM $n = 2$; (b) WGM $n = 3$; (c) WGM $n = 4$; (d) WGM $n = 5$; (e) WGM $n = 6$.

2.4.3 Experimental setup

In this work, only the 17.6-mm cylindrical sapphire was exploited as SWGT because of its higher Q factor respect to the 12-mm sapphire sphere used by Yu in [32]. Measurements in the range from 0 °C to 40 °C were performed placing the WGM resonator inside a thermostatic bath together with a SPRT as depicted in Figure 19. The resonator was not in contact with the bath, but suspended through a support in order to avoid the mechanical vibrations of the bath that could affect the measurements.

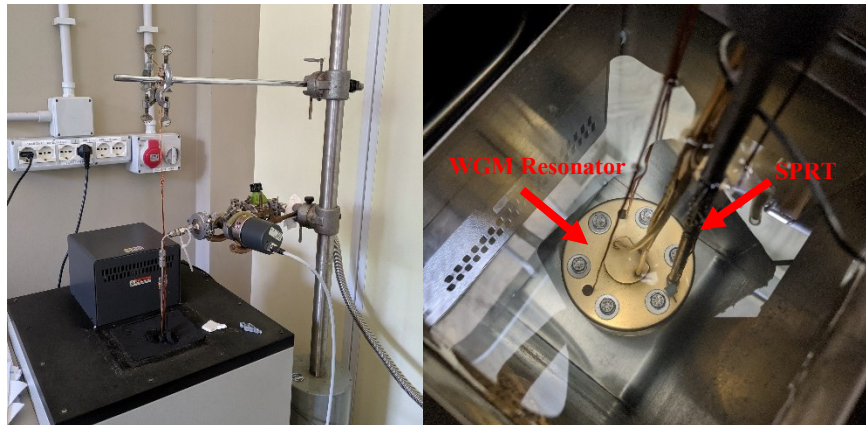


Figure 19 WGM resonator and SPRT inside the bath. The WGM resonator is suspended for the vibrations rejection.

The resonator cavity was connected to a vacuum pump in order to remove the pressure dependency of the resonant frequency and to avoid water vapor condensation at low temperatures. A pressure of about 1.6 mbar ($u = 0.1$ mbar) was

set inside the cavity. The resonance spectrum was monitored for the entire measurement process and the SPRT temperature was recorded as well. A more detailed description of the instrumentation setup employed in this work is reported in the following.

VNA R&S ZNB20

The VNA ZNB20 by Rohde&Schwarz was used for the acquisition of the transmission coefficient (S_{21} parameter) of the WGM resonator. It was connected to the resonant cavity through two RG402 semi-rigid coaxial cables. Central frequency, bandwidth, number of acquired points and other parameters were set using a specifically made interfacing software. A more detailed description of this software is reported in the next paragraph. Table 4 includes the main specification of the VNA used for these measurements [53].

Table 4 ZNB specifications from the datasheet

Impedance	50 Ω
Number of test ports	2
Frequency range	100 kHz to 20 GHz
Static frequency accuracy	(time since last adjustment x aging rate) + temperature drift + calibration accuracy
Relative aging per year	$\pm 10^{-6}$
Relative temperature drift (0 °C to +50 °C)	$\pm 10^{-6}$
Relative achievable initial calibration accuracy	$\pm 5 \times 10^{-7}$
Frequency resolution	1 Hz
Number of Measurement points	1 to 100,001
Measurement bandwidth	1 Hz to 1 MHz
Accuracy of transmission measurements (1 MHz – 20 GHz; -35 dB – -50 dB)	Magnitude: < 0.08 dB Phase: < 0.8°

SPRT and Fluke 1586A

One SPRT was used to measure the temperature of the cavity block. It was inserted in one of the three 7 mm holes designed in the resonator cavity. The thermometer was a 25.5 Ω platinum resistance calibrated at the ITS-90 temperature fixed points in the range 83.8058 K (triple point of argon) to 419.5270 °C (freezing point of zinc) with an uncertainty lower than 1 mK. The last 50 mm of the thermometer was inserted inside the cavity block in order to ensure that the entire sensitive part, usually the last 30 mm, was in contact with the metal block.



Figure 20 INRiM SPRT used in the experiment. The last 50 mm were inserted in the cavity metal block

In preliminary measurements, the SPRT resistance value was measured using a resistance bridge Fluke model 1586A. This is a 6½ digit DAQ with an accuracy of 0.8 mΩ in the measurement range from 0 Ω to 400 Ω. This corresponds to an accuracy of 8 mK for a 25.5 Ω SPRT. Other technical specifications can be found in the instrument datasheet [54]. The Fluke 1586A was used in the first part of the experimental activity in which all five WGMs in the range 6 GHz – 14 GHz were observed at different temperatures. Once the best WGM was selected in terms of sensitivity and Q factor another resistance bridge with higher resolution and better accuracy was used.

ASL F900 Precision Thermometry Bridge

Preliminary measurements indicated that for a good compromise between the SWGT sensitivity and resolution (Q factor), the WGM of order 5 ($f = 12.2$ GHz) should be selected. More information about the preliminary results are reported in Section 2.5. Once the best mode was selected, measurements were carried out using an ALS F900 Precision Thermometry Bridge. It is a primary standard resistance thermometry bridge specifically designed for resistance thermometry in order to provide the highest possible accuracy. This instrument is used by the INRiM calibration laboratories for SPRT calibration. As reported in the instrument technical document [55], the ASL F900 has a resistance ratio resolution of 10^{-9} and an accuracy of 2×10^{-8} . This bridge was used in conjunction with a temperature-controlled reference resistance of 25 Ω.



Figure 21 ASL F900 with the temperature-controlled reference resistance

Vacuum system

During the SWGT tests, the cavity was connected to a vacuum system through some Swagelok connectors. A Leybold DIVAC 0.8 T dry compressing vacuum pump was used for this purpose. The residual pressure inside the cavity was maintained to a value lower than 2 mbar. This was needed in order to remove the pressure dependence of the resonant frequency and the risk of water vapor condensation at low temperatures.

2.4.4 Software developed

Measurement data from Fluke 1586A, ASL F900 and R&S ZNB20 were acquired and recorded by a PC. Two software programs, developed in Python, were written for this purpose. The first one collected data from the instrument (RS232 protocol for Fluke 1586A or IEEE488 for ASL F900) and recorded in a file the timestamp, the resistance value and the corresponding temperature value according to the ITS-90 temperature scale. For this conversion, the calibration coefficients as reported in the SPRT certificate were used. A plot is also shown to the user with the resistance value as a function of time and some statistics (average value of resistance and standard deviation). The software allows the user to change the instrument setup. Figure 22 shows the GUI for the ASL F900 interfacing software. The excitation current, carrier frequency, gain, source impedance and other parameters described in the instruments datasheet [55] can be set.

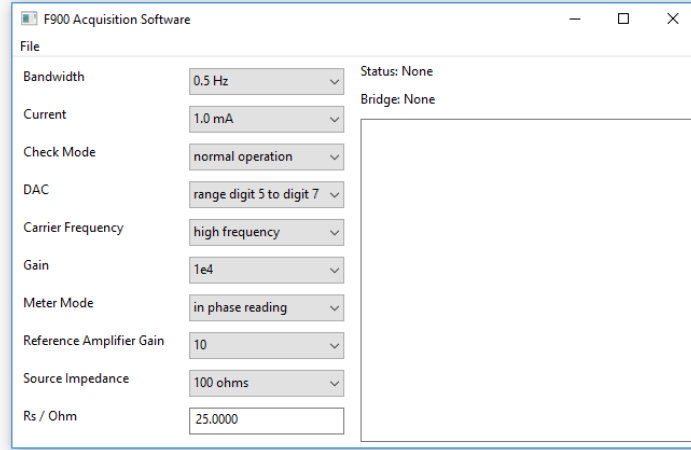


Figure 22 GUI for ASL F900 python program

The software written for the VNA interfacing acquires data of the transmission coefficient S_{21} and performs a Lorentzian fitting of the acquired frequency spectrum for proper identification of resonant frequency and Q factor of the peak. For this purpose, a fitting algorithm was developed based on the *Levenberg-Marquardt* method and using the Lorentzian function ($L(f)$) in the form [56], [57]:

$$L(f) = \frac{a_0 f}{f^2 - f_0^2}, \quad (2.3)$$

where a_0 and f_0 are complex quantities calculated by the algorithm in order to find the best fit. The value f_0 can be expressed as the following complex number:

$$f_0 = f_r + jg, \quad (2.4)$$

with f_r resonance frequency of the peak and g half-power bandwidth. The quality factor of the peak can be written as a function of f_0 and g :

$$Q = \frac{f_r/g}{2}. \quad (2.5)$$

In this work, Eq. 2.5 is used to calculate the quality factor instead of Eq. 1.6. Finally, a background signal was modeled with a complex function ($B(f)$) in the form [56], [57]:

$$B(f) = \sum_{n=0}^N b_n (f - f_r)^n, \quad (2.6)$$

where b_n are the complex coefficients to be found. Experimental measurements proved that $N = 4$ is enough for a good fitting. The final complex function $T(f)$ used for the Transmission coefficient fitting is:

$$T(f) = \frac{a_0 f}{f^2 - (f_r + jg)^2} + b_0 + b_1(f - f_r) + b_2(f - f_r)^2 + b_3(f - f_r)^3 + b_4(f - f_r)^4, \quad (2.7)$$

with eight parameters to be calculated for the best fit.

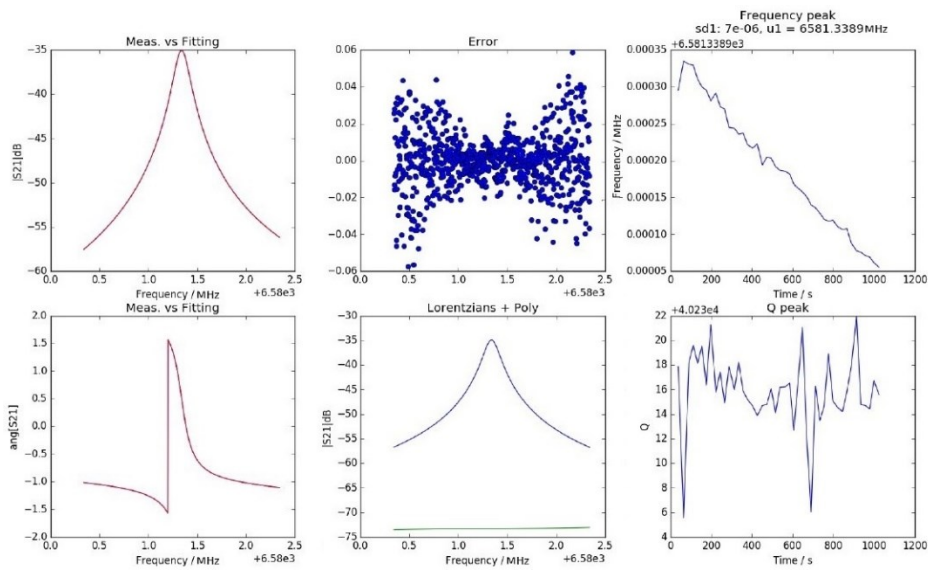


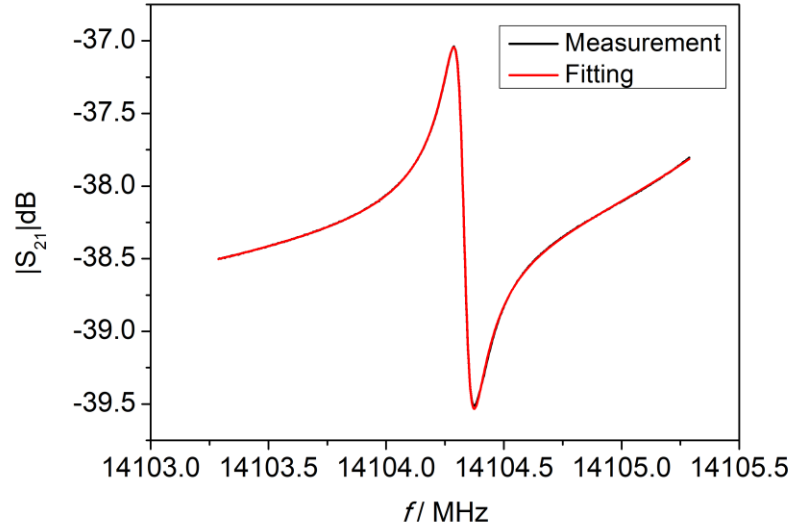
Figure 23 Plots displayed by the ZNB20 software. Acquisition of the $WGM_{n=2}$ at 6.58 GHz

The fitting process is performed in real-time at each acquisition and the main function takes about 4 s to converge with a Pentium IV processor. The same software is able to perform the fitting as a post-processing operation. In this case it can rely on parallel computing for the fitting algorithm: with the actual algorithm, an Intel Xeon E5 2699 processor is able to fit about 450 lorentzian functions per second (approximately 2 ms per fitting). The fitting performances are described in Figure 24, as shown in the graph (a) the acquired spectrum and the fitted function of the resonant peak at 14.1 GHz are perfectly over imposed. In plot (b) the fitting residuals are reported for the imaginary and real part, they are always less than 4×10^{-5} . This value corresponds to an error of approximately 0.1 % according to the following:

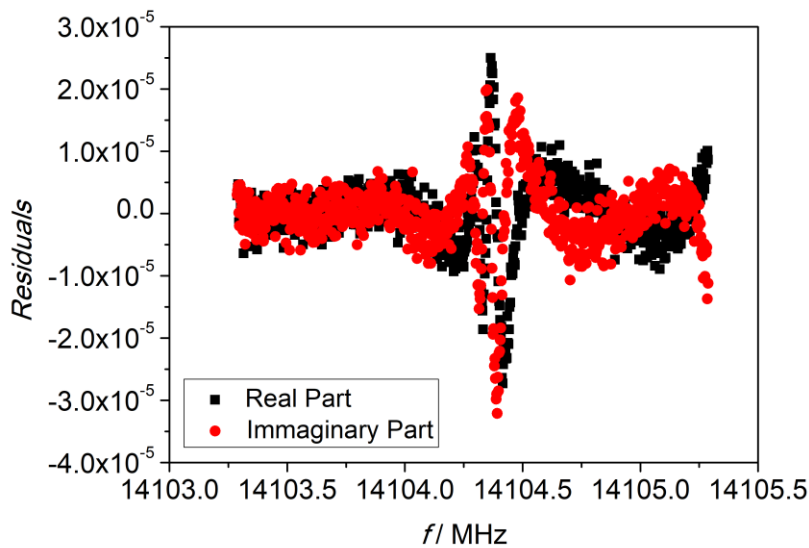
$$E_r = \frac{x_m - x_f}{x_m} \cdot 100 \quad (2.8)$$

Where E_r is the percentage error, x_m is the measured value and x_f is the fitting value.

The high performance of the implemented fitting is a good starting point for high-resolution measurements of the resonance frequency.



(a)



(b)

Figure 24 Lorentzian fitting algorithm performances: (a) the S_{21} magnitude acquired with the VNA and the fitted functions are reported in this plot, they are well over imposed; (b) The lorentzian fitting residuals for the real and imaginary part are reported in this graph. They are always less than 4×10^{-5} in magnitude.

A Telegram bot was finally created for the remote supervision of the measurements. Telegram is a cloud-based mobile and desktop messaging app [58], it allows exchanging text messages and media between two or more accounts. Bots are special Telegram accounts that are managed by software programs and offer several features like fully automated answers. In this work, a Telegram bot was employed as a logging system. For the entire measurement session, the end-user

was informed about all the acquisition steps and at the end of each session a screenshot of the desktop application (Figure 23) with some statistics (i.e., frequency average and standard deviation) were sent through the app. Figure 25 shows a screenshot of the mobile application.

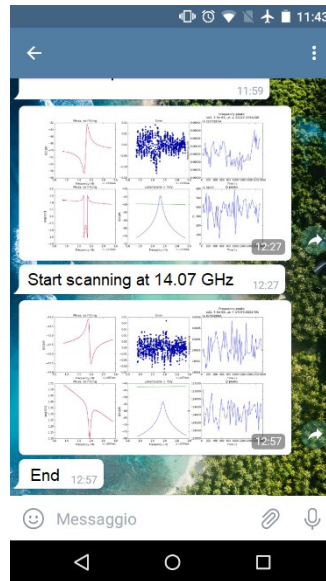


Figure 25 Telegram bot with data regarding two measurement sessions

2.5 Measurements and Results

Measurements were carried out in the temperature range starting from the triple point of mercury ($-38.8344\text{ }^{\circ}\text{C}$) to the melting point of gallium ($+29.7646\text{ }^{\circ}\text{C}$). In preliminary measurements the subrange from the triple point of mercury to the triple point of water ($0.01\text{ }^{\circ}\text{C}$) was considered.

2.5.1 WGM resonator: preliminary measurements

In preliminary measurements, the WGM resonator sensitivity to temperature was evaluated in the range between $-40\text{ }^{\circ}\text{C}$ and $0\text{ }^{\circ}\text{C}$ at 41 steps ($1\text{ }^{\circ}\text{C}$ each). All the whispering gallery modes in the bandwidth 6 GHz to 14 GHz were considered at this stage.

The thermostatic bath was filled with pure ethanol and both the SWGT and a reference SPRT were immersed. The bath temperature was changed every 4.5 hours, the first two hours were used for the temperature stabilization and then the data acquisition started. The SWGT design allows to host three SPRT in order to evaluate the heat flux and so the temperature uniformity into the microwave resonator. However, during this calibration procedure, only one SPRT was employed because of the relatively long time between two consecutive temperature set points.

Five different WGMs were monitored in the selected bandwidth; the acquisition time was about 30 minutes each. The Lorentzian fitting was performed

in real-time so that the resonant frequency and Q factor were monitored during the whole measurement process. The fractional change in f_0 ($(df_0/dT)/f_0$) as a function of temperature and the Q factors for the five WGMs is reported in Figure 26.

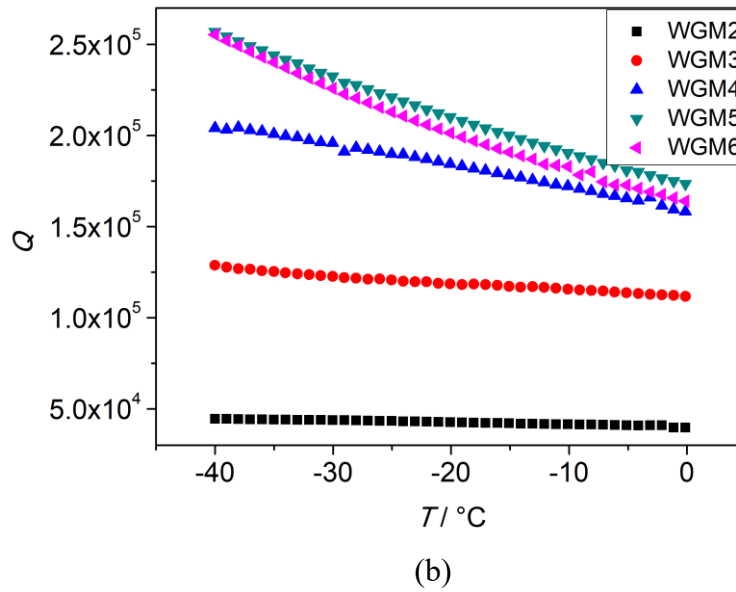
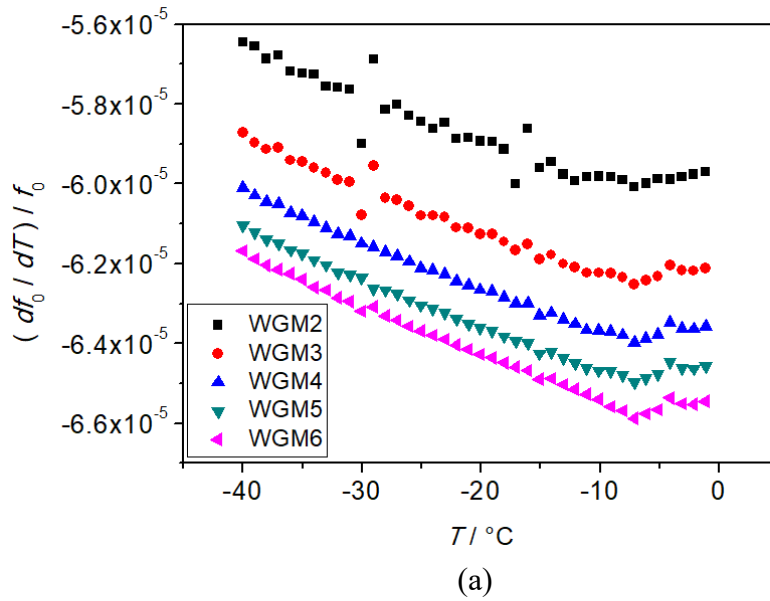


Figure 26 Measurements made on five different WGMs in the temperature range $-40\text{ }^{\circ}\text{C} / 0\text{ }^{\circ}\text{C}$. (a) Fractional change as a function of the temperature; (b) Quality Factor change with temperature, the highest Q factor is associated with the WGM5 ($f = 12.2\text{ GHz}$).

As shown in Figure 26, both the $(df_0/dT)/f_0$ and Q factor vary with the WGM considered. For instance, for WGM6 at 14 GHz the fractional change is -65×10^{-6} at $0\text{ }^{\circ}\text{C}$ and -62×10^{-6} at $-40\text{ }^{\circ}\text{C}$, these values are similar to that reported in the literature [1]. The highest Q factor is reached by the WGM5 at 12 GHz, its value is 173000 at $0\text{ }^{\circ}\text{C}$ and 257000 at $-40\text{ }^{\circ}\text{C}$. Because of its higher quality factor, the mode at 12 GHz was considered for the successive SWGT calibration. The WGM6 has a

good sensitivity and quality factor as well, but it is close to a cavity resonance and it was tricky to estimate its central frequency and quality factor with high accuracy.

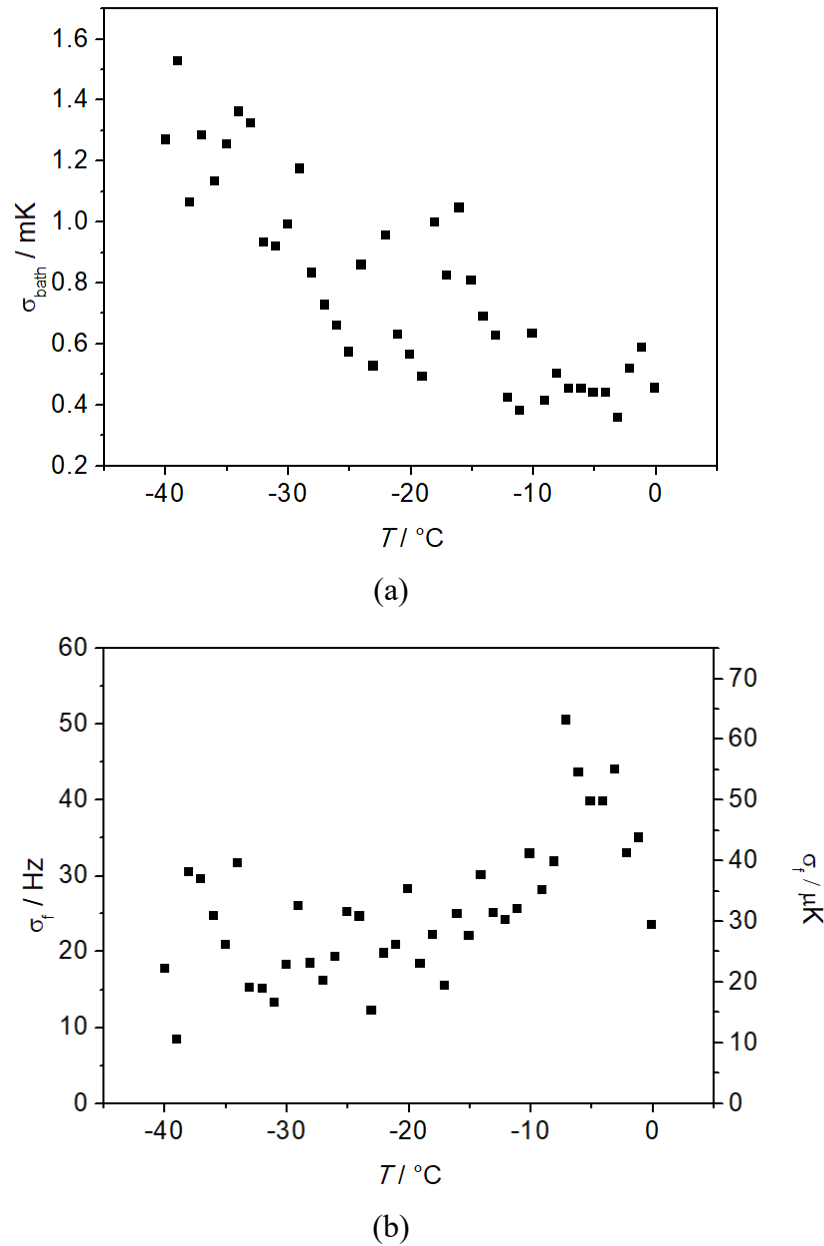


Figure 27 SPRT standard deviation at different temperatures (a), resonant frequency standard deviation as a function of temperature (b).

During the measurement process, the stability of the bath was better than 1.6 mK (Figure 27 a). The temperature fluctuations of the bath were further smoothed down thanks to the high thermal mass of the SWGT copper cavity so that a standard deviation of less than 50 Hz was observed through the SWGT resonance frequency measurements. Considering an SWGT sensitivity of approximately 0.8 MHz/°C, it corresponds to 63 μK or better (Figure 27 b).

2.5.2 WGM5: calibration against SPRT

After the preliminary measurements, the resonator was thermally characterized against an INRiM SPRT connected to the ASL F900 precision thermometry bridge with a temperature-controlled 25 Ω resistance as reference. As made before, the temperature range from -40 $^{\circ}\text{C}$ to 0 $^{\circ}\text{C}$ was explored in several steps of 1 $^{\circ}\text{C}$ each. Moreover, this range was extended above the melting point of gallium (30 $^{\circ}\text{C}$) with seven more points. A 5th order function was used to fit the resonance frequency f_0 of WGM5 ($f = 12.2$ GHz), the calibration curve and the fit residuals are reported in Figure 28.

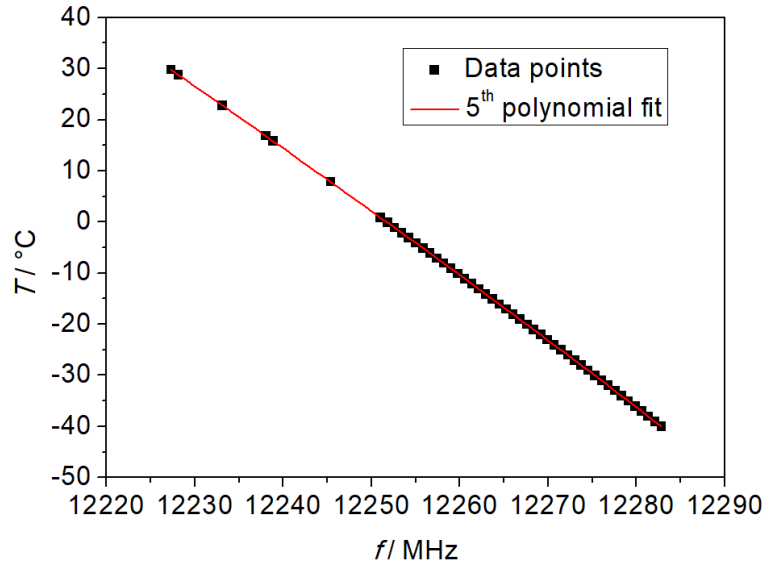


Figure 28 Fifth order polynomial calibration curve in the temperature range from -40 $^{\circ}\text{C}$ to 30 $^{\circ}\text{C}$

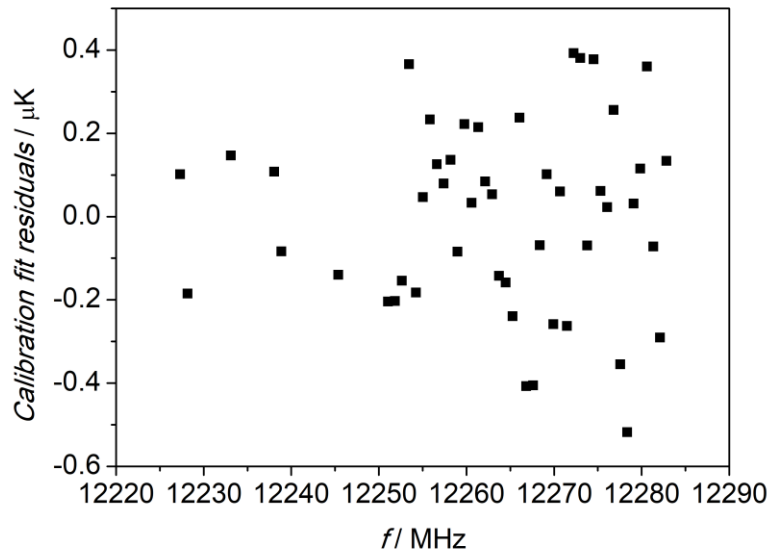


Figure 29 Calibration fit residuals. As shown in the plot, in the considered range they are always within ± 600 μK

As shown in Figure 29, the calibration fit residuals in the whole range from -40 °C to 30 °C are within ± 0.6 mK, approximately one order of magnitude better than that obtained by Yu [48] and Ramella [46] in the same measurement range. Moreover, the new resonator design did not exhibit the mechanical instabilities described in [46].

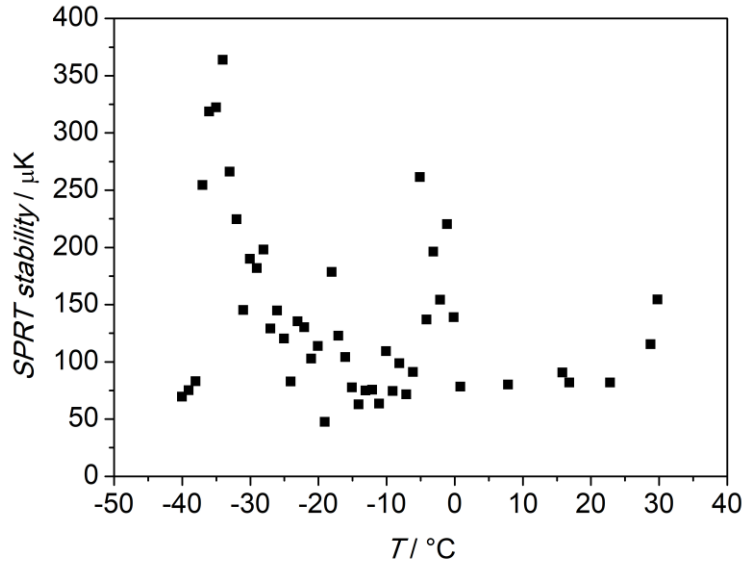


Figure 30 Standard deviation of the SPRT measurements. During the experiment, the SPRT was placed inside the copper block through the designed hole.

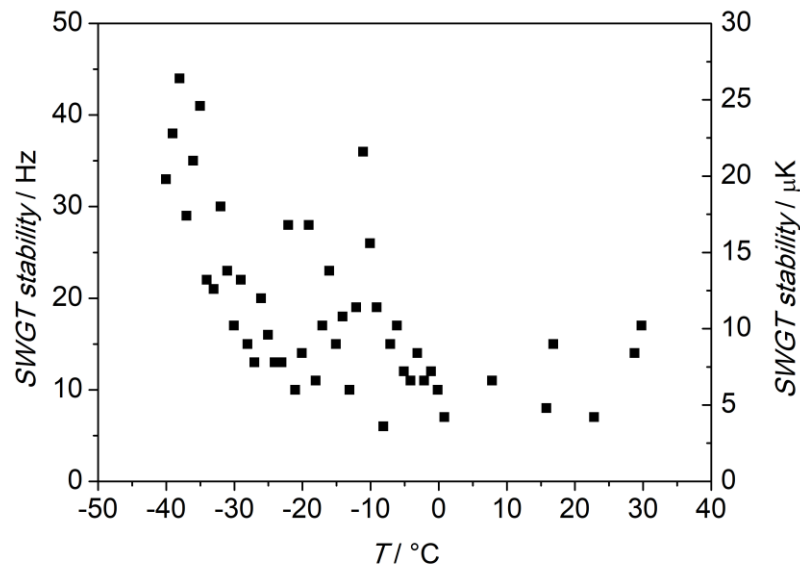


Figure 31 Standard deviation of the WGM frequency measurements at each temperature step.

2.5.3 WGM resonator: calibration using a deviation function

A novel approach is introduced in this thesis for the SWGT calibration. Similarly to the SPRT calibration defined in the text of the ITS-90 [59], a reference function for the generic SWGT is given and the fitting is performed on the difference between the calibration curve and the reference function.

In 2013, Yu *et al.* [60] analyzed the performance of several SWGTs and wrote down different calibration curves. In the calibration process she considered a 4th order polynomial in the form:

$$T = a_0 + \sum_{i=1}^4 a_i f^i. \quad (2.9)$$

She noticed that the a_i coefficients were almost the same for all the crystal sapphires, only the a_0 coefficients were quite different. This behavior allowed her to perform single-point calibrations, considering a_0 as the unique unknown, with a reproducibility of about ± 40 mK.

Her work proved that even if the resonance absolute value changes from sapphire to sapphire, and it depends on permittivity, size and other physical parameters, the temperature sensitivity is almost constant for different SWGTs. This is a good starting point for a definition of a generic reference function for the sapphire whispering gallery mode thermometer.

As reported in Section 2.3, the relationship between SWGT resonant frequency and temperature can be expressed according to the Eq. 2.2 that, for quasi-TM modes, can be approximated to [1]:

$$\frac{1}{f_0} \frac{\partial f_0}{\partial T} = -\frac{1}{2} \frac{1}{\varepsilon_{\parallel}} \frac{\partial \varepsilon_{\parallel}}{\partial T} - \alpha_{\perp}, \quad (2.10)$$

where:

- f_0 is the resonance frequency,
- T is the temperature,
- ε_{\parallel} is the permittivity in the axial direction,
- α_{\perp} is the sapphire thermal expansion coefficient along the radial direction.

Integration of Equation 2.10 results in the following equation:

$$\frac{f_0 - f_0|_{T_0}}{f_0|_{T_0}} = -\frac{1}{2} \left[\ln|\varepsilon_{\parallel}|_T - \ln|\varepsilon_{\parallel}|_{T_0} \right] - \int_{T_0}^T \alpha_{\perp}(T) dT, \quad (2.11)$$

where:

- T is the temperature at each measurement point,
- $T_0 = 0$ °C

The above equation gives an explicit formulation of the resonant frequency as a function of temperature with known $\epsilon_{||}$ and a . Even if analytical expressions for the sapphire permittivity and thermal expansion are not available, measurements of these two quantities are reported in the literature as a function of temperature. Egorov and Volovikov published an article in 2001 about the measurements of the dielectric permittivity of sapphire in the temperature range $-180\text{ }^{\circ}\text{C}$ to $70\text{ }^{\circ}\text{C}$. Their results are in a fairly good agreement with that obtained previously by Krupka [52] and Shelby [50]. Figure 32 reports these measurements as well as the 3rd order fitting.

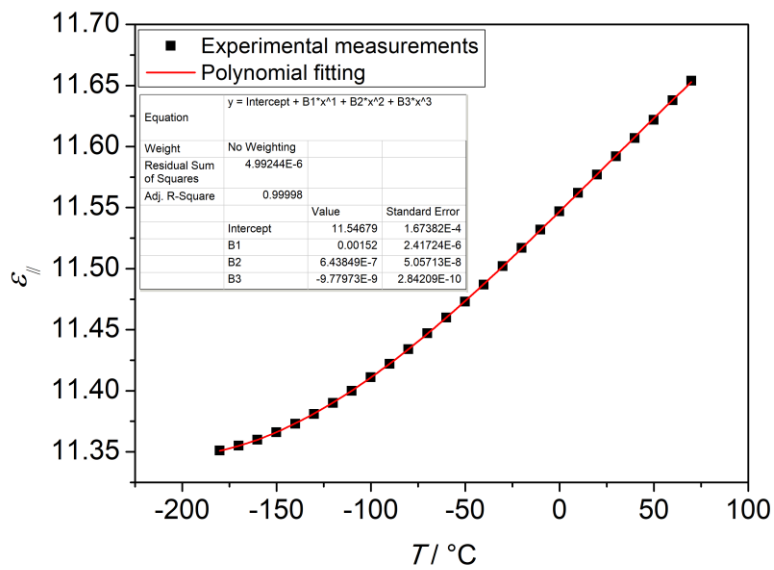


Figure 32 Sapphire permittivity as a function of temperature. Third-order fitting performed on Egorov and Volovikov data.

The same approach can be used for the measurements of the sapphire thermal expansion carried out by Guy K. White [61].

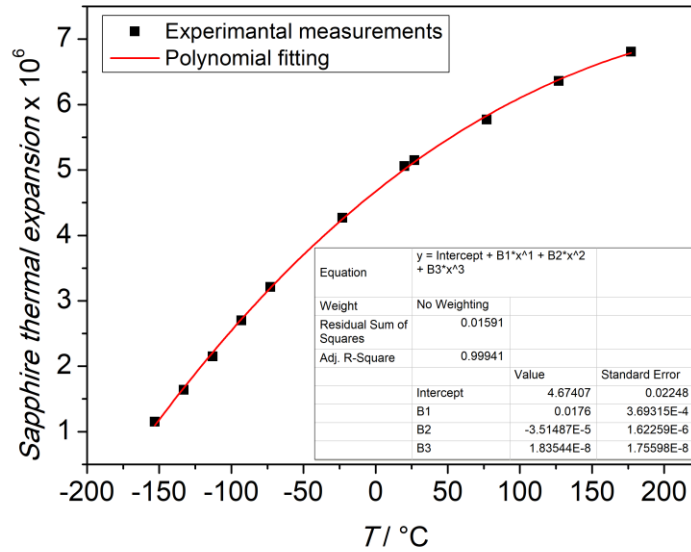


Figure 33 Sapphire thermal expansion coefficient along the crystallographic z-axis as a function of temperature. Third-order fitting on White raw data, a subrange of White measurements is considered.

White [61] performed measurements in the temperature range from -253 °C to 727 °C. For the fitting, only the interval from -153°C to 177 °C was taken into account in order to consider a lower order polynomial function and a range similar to that considered for sapphire permittivity.

By using the polynomial expressions for the sapphire permittivity and thermal expansion, it is possible to calculate the normalized frequency shift from Eq 2.11. The plot in Figure 34 shows both the calculated (S_s , calibration function) and measured (S_m , reference function) SWGT normalized shift in the relevant temperature range from -40 °C to 30 °C.

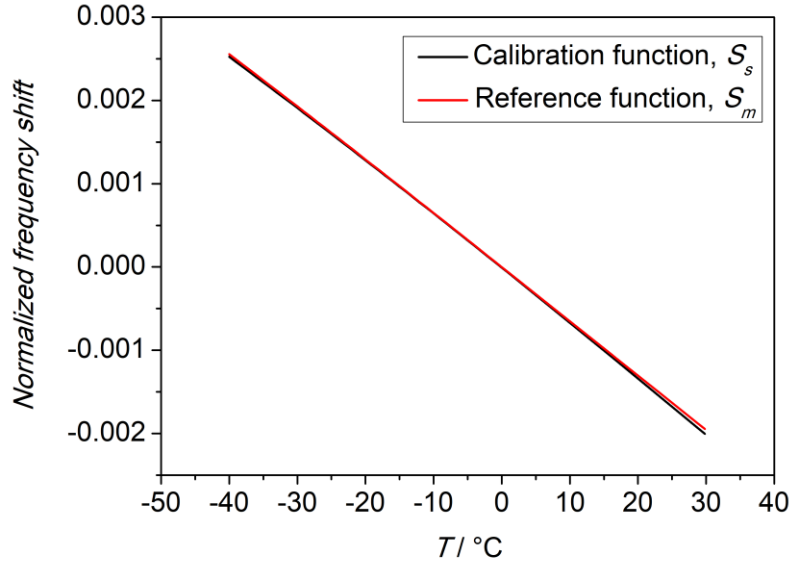


Figure 34 Comparison between the measured (Calibration function) and calculated (Reference function) normalized frequency shift.

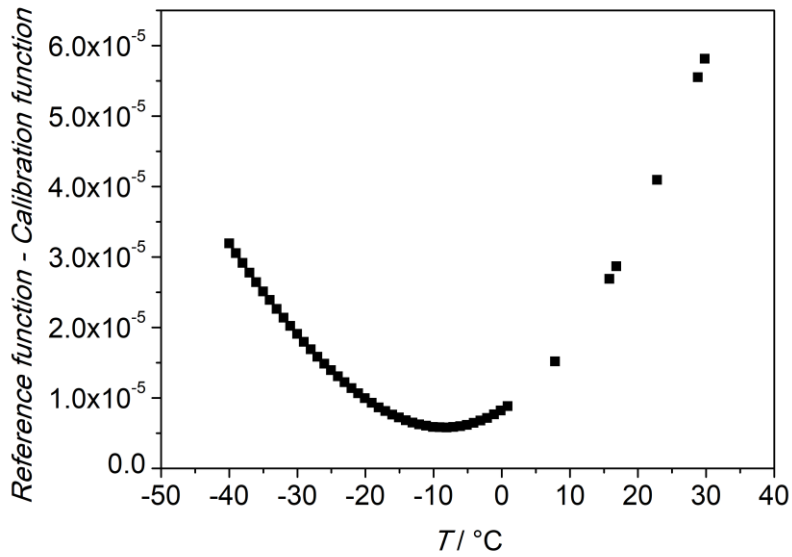


Figure 35 Difference between Calibration function and Reference function

S_s is the reference function of a generic SWGT and it comes from the eq. 2.11, S_m is the measured shift and represents the calibration function of a specific SWGT under test. It comes from experimental measurements. It is possible to define a deviation function S_d (Figure 35) as:

$$S_d = S_s - S_m \quad (2.12)$$

This is something similar to the deviation function defined in the International Temperature Scale ITS-90 for the SPRT and can be written as:

$$S_d = a_0 + \sum_{i=1}^N a_i T^i \quad (2.13)$$

Where $(N+1)$ is the number of calibration points and the a_0, a_i terms are calculated during the calibration procedure. In ITS-90, this method is used to reduce the number of SPRT calibration points. Indeed, to represent the function $R(T)$ of any SPRT a twelve-order polynomial function should be required. This involves at least thirteen fixed points that is absolutely not practical. A deviation function is so defined as the difference between a reference function and the calibration curve of the SPRT under test. For ITS-90 compliant SPRTs the deviations are small and can be represented by low-degree polynomials defined in the text of the ITS-90 [59].

Experimental measurements showed that for the SWGT used in this thesis a fifth-order polynomial is needed to fit, with sub-millikelvin residuals, the deviation function. This is the first attempt to apply this calibration approach to a WGM resonator. In Figure 36 the calibration residuals are reported.

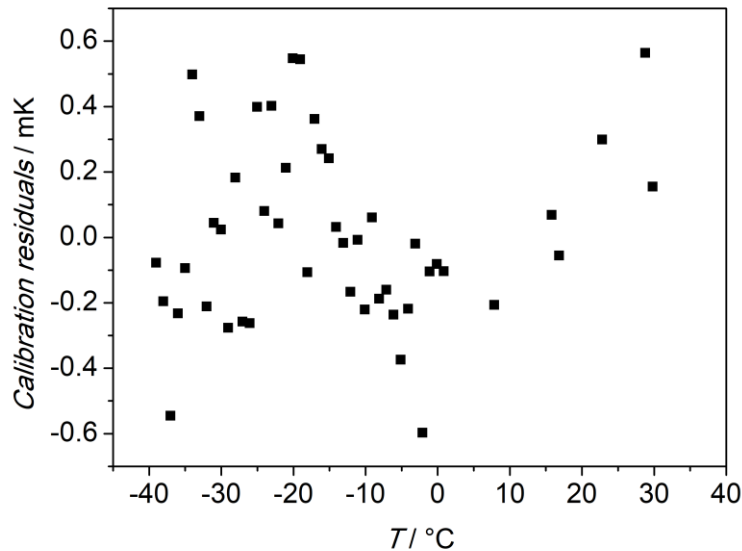


Figure 36 SWGT residuals when a deviation function is used for the calibration

The residuals reported in Figure 36 are very similar to those obtained in the previous section. This proves that, at least, the performance of the two calibration methods is equivalent. A thermal characterization of a higher number of SWGT would provide a better reference function so that only a few calibration points would be needed.

2.5.4 WGM resonator: calibration using the thermodynamic temperature scale

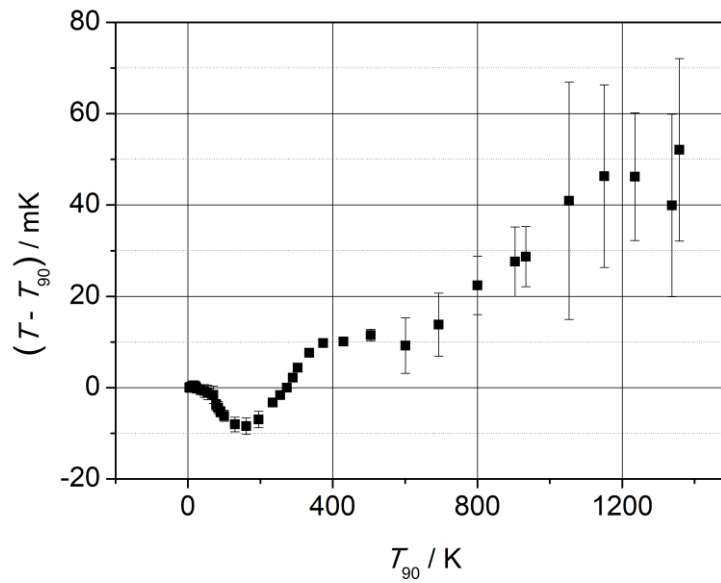
Previously, the SWGT was calibrated using a calibrated SPRT as a reference thermometer so, the temperature was measured according to the ITS-90 scale and not according to the thermodynamic temperature scale.

Instead of using the SPRT as a thermometer, it is possible to use it as a comparator in order to relate the SWGT resonance frequency to the thermodynamic temperature of the fixed-points: the SPRT resistance at fixed-points is known from the calibration certificate. The deviation of the ITS-90 temperature (T_{90}) of these points from the thermodynamic temperature (T) is also well known [62], [63]. On the contrary, the difference $T-T_{90}$ between two consecutive fixed points with high resolution is still under discussion.

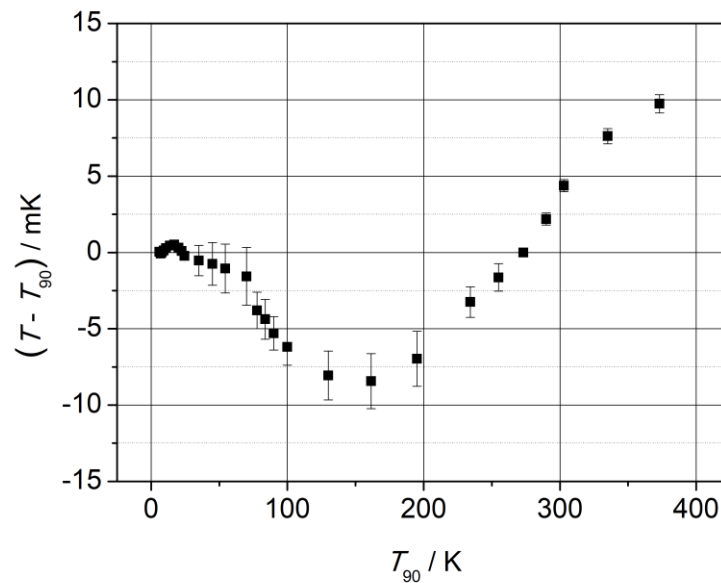
Table 5 T and T_{90} temperatures for the explored fixed points. The INRiM SPRT resistance is also reported in the table

Temperature fixed point	$T_{90} / ^\circ\text{C}$	$T / ^\circ\text{C}$	INRiM SPRT resistance / Ω
Triple point of Mercury	-38.8344	-38.8377	21.3509
Triple point of water	0.01	0.01	25.2924
Melting point of gallium	29.7646	29.7690	28.2812

Once the fixed point temperature is reproduced inside the thermal bath by comparing the SPRT resistance to the value reported into the calibration certificate (see Table 5), the thermodynamic temperature T is considered in the calibration process. In this work, beside this three fixed points, additional points were considered in the calibration procedure. In this case, the $T-T_{90}$ deviations reported in the literature [62] were considered. Figure 37 reports the $T-T_{90}$ data reported in the literature [62].



(a)



(b)

Figure 37(a) Differences between thermodynamic temperatures and the ITS-90. In (b) a subrange is reported. Data published in [62].

After the SWGT calibration, measurements were carried out with the SWGT and SPRT inside the temperature bath so that the T_{90} temperature value of the SPRT was compared with T value estimated from the SWGT calibration curve. Such deviations are reported in Figure 38 and compared with other estimations reported in the literature [62], [63].

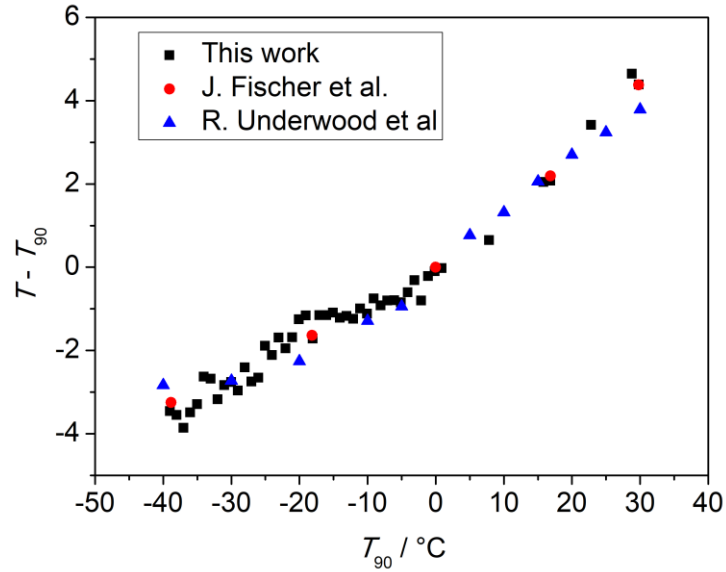


Figure 38 The estimated values of $T - T_{90}$ are compared with the estimations reported in the literature by J. Fischer and R. Underwood

2.5.4 SWGT resonant frequency vs. SPRT resistance

In a final experiment, the SWGT resonance frequency was compared with the SPRT resistance at different temperatures. This is something different to the analysis carried out in Section 2.5.3 in the following aspects:

- previously, the SWGT was calibrated against the SPRT. The temperature value was calculated starting from the platinum resistance by using the SPRT coefficients reported in the certificate.
- Now, just the SPRT resistance value is considered and compared with the corresponding resonant frequency. In this way it is possible to overcome the SPRT calibration and the polynomial function used to fit the SPRT calibration data.

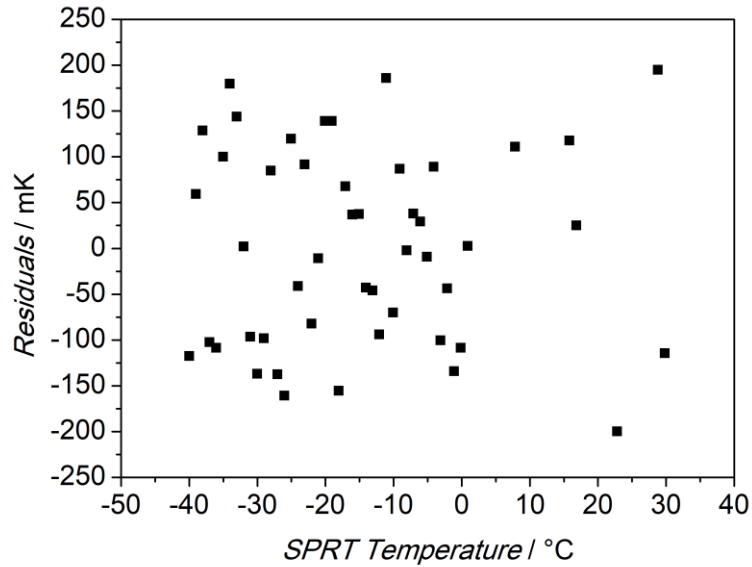


Figure 39 Residuals from the SWGT resonant frequency vs SPRT resistance fitting. The SPRT resistance in the plot was expressed in terms of its corresponding temperature in order to improve the legibility of the plot. The residuals were converted in temperature as well by considering the SWGT sensitivity to temperature variations.

A 5th order polynomial function was used to fit the frequency against the SPRT resistance. As shown in Figure 39, the frequency residuals as converted in temperature unit are within $\pm 200 \mu\text{K}$, a value slightly higher than $60 \mu\text{K}$ obtained by Corbellini *et al.* in [56]. However, because of mechanical instabilities, Corbellini considered a narrow temperature range from $-20 \text{ }^\circ\text{C}$ to $30 \text{ }^\circ\text{C}$. In this thesis the whole temperature interval from the triple point of mercury ($-38.8344 \text{ }^\circ\text{C}$) to the melting point of gallium ($29.7646 \text{ }^\circ\text{C}$) was investigated with promising results.

The narrow scatter of the fitting residuals proves that the relationship between the SWGT resonance frequency and the SPRT resistance can be modeled quite well with a 5th order polynomial function. The performances of the two instruments are, at least in the above temperature range, compatible. Of course, by considering the SPRT as a reference, it is not possible to prove that the SWGT performance is better. However, it is possible to independently evaluate the SWGT measurements stability and repeatability and compare them with the SPRT performance. The next section contains a detailed description of these measurements.

2.5.5 SWGT stability and repeatability of the ice melting point

In order to evaluate the SWGT stability, some measurements were performed with the resonator placed inside a melting ice bath. The experimental setup was the same described previously but, in this case, a dewar with melting ice was used as shown in Figure 41 to get rid of the small temperature oscillations due to the bath control system. In a period of about 30 minutes, the SWGT resonance frequency was fluctuating around its average value with a peak-to-peak fluctuation of $\pm 30 \text{ Hz}$

and a standard deviation of 11 Hz that corresponds to approximately 14 μK in temperature unit (Figure 40). Such a small standard deviation estimate proves the capability of the system to perform measurements with a very high resolution.

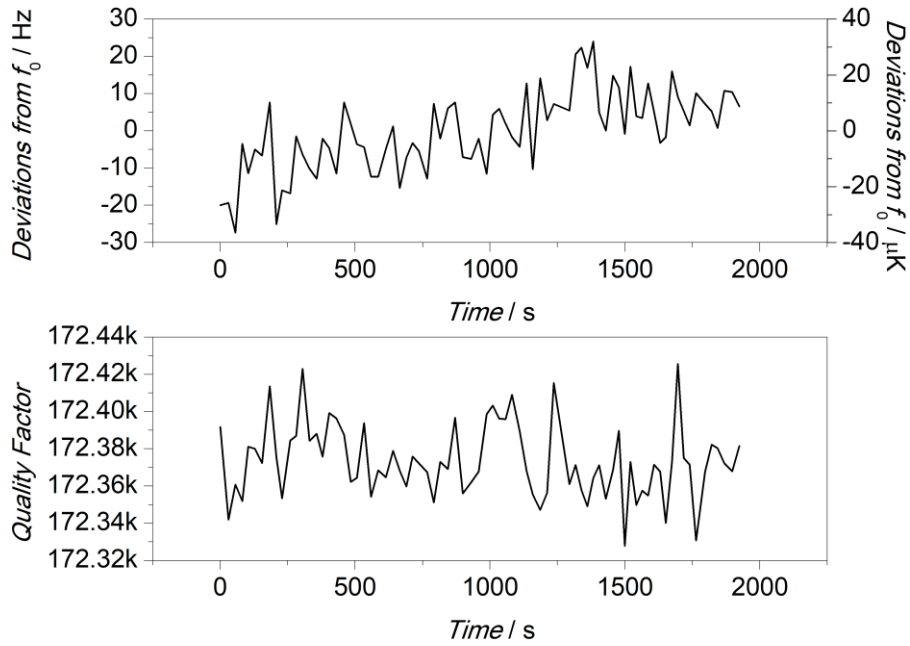


Figure 40 SWGT resonance frequency and quality factor deviations with the resonator placed inside the melting ice bath



Figure 41 SWGT inside the dewar with melting ice

Finally, the SWGT temperature stability was compared to that of the SPRT in the same condition. For this comparison, the temperature fluctuation as detected by the SPRT were converted in a frequency unit (by the resonator sensitivity according to Eq. 2.12) and an “equivalent” resonance frequency deviation for the SPRT was calculated.

$$\Delta f = \Delta T_{SPRT} \cdot S_{SWGT} \quad (2.14)$$

This step is needed in order to normalize the scales for the SPRT and SWGT measurements.

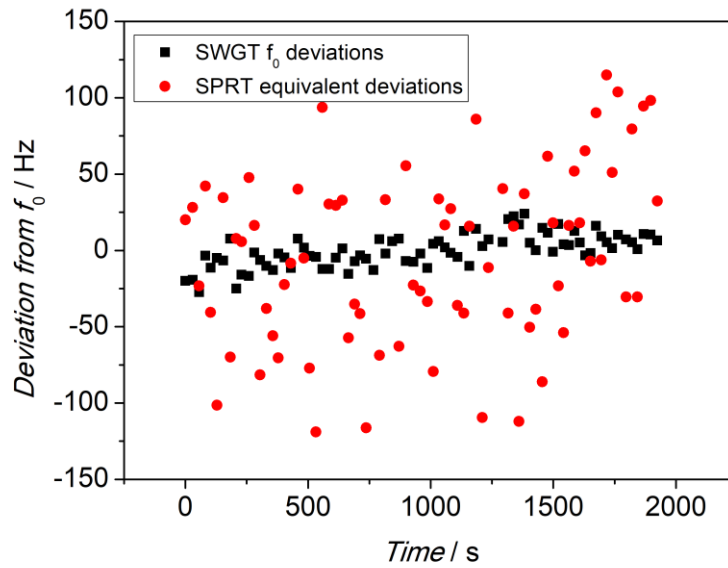


Figure 42 SWGT and SPRT stability comparison

As shown in Figure 42, the SWGT stability is at least five times better than the equivalent SPRT stability. This result is in line with the measurements carried out by Corbellini *et al.* in [56], so confirm the good performance of a SWGT temperature measurements.

The ice melting point repeatability was evaluated by placing the SWGT and SPRT in the ice bath several times. The results are reported in Figure 43. Also in this case, the SWGT performs the better measurement standard deviation of the SWGT is lower than 0.4 mK, while for the SPRT the estimate is about 2.3 mK, again more than five times better.

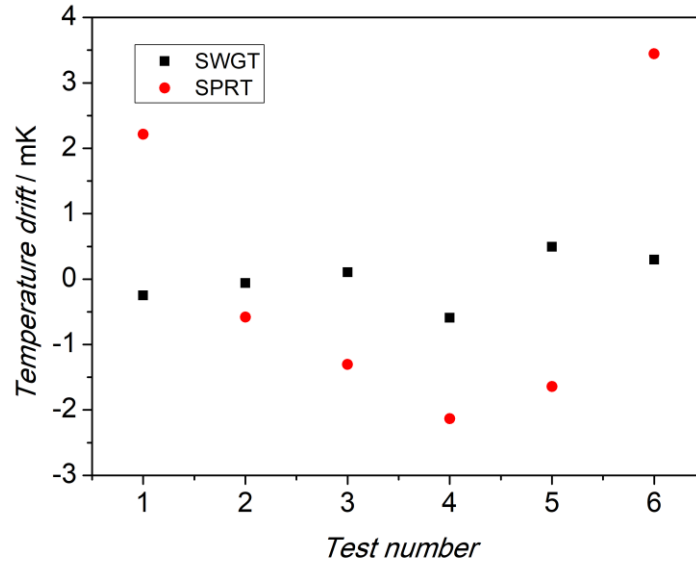


Figure 43 SWGT and SPRT measurement repeatability comparison

From the stability and repeatability analysis, the microwave-based thermometer exhibited better performances in comparison to a standard platinum thermometer. This confirms the SWGT as a good candidate for temperature measurements at least in a limited temperature range with metrological performance which may exceed the SPRT.

2.5.6 Uncertainty Budget Analysis

For the estimation of the overall measurement uncertainty in SWGT temperature measurement, an uncertainty analysis was carried out in the explored range. The major uncertainty contributions in SWGT measurements are reported in Table 6.

Table 6 Main uncertainty contributions from the SWGT calibration. The values in the gray cells refer to the uncertainty contributions of the microwave sensor

Uncertainty contribution	Value
Frequency measurement ¹	45 μ K
Measurement stability	14 μ K
Measurement repeatability	0.4 mK
SWGT calibration (5 th order fitting)	0.2 mK
Thermostatic bath stability	0.4 mK
Thermostatic bath uniformity ²	3 mK

SPRT Calibration	1 mK
ASL F900 Thermometry bridge	10 μ K

¹ The uncertainty contributions due to the frequency measurements are listed in Table 6.

² The value reported in datasheet

Table 7 Uncertainty contributions due to the frequency measurements.

Uncertainty contribution	Value
Lorentzian fitting reproducibility	10 μ K
VNA accuracy	< 5 μ K
10 MHz frequency reference stability	23 μ K
VNA resolution	< 5 μ K

Considering all the uncertainty contributions reported in Table 2, the combined measurement uncertainty ($k = 1$) is 3 mK. A normal distribution was considered for each individual contributory factors. The thermostatic bath used in the calibration process gives the main contribution to the present measurement uncertainty. An improvement of this value, e. g., by using a fixed point calibration approach, would considerably reduce the SWGT measurement uncertainty.

2.6 Conclusions

A sapphire-based whispering gallery mode resonator (SWGT) was exploited as a thermometer. Its design was based on Strouse and Yu studies and some improvements were added. In particular, the mechanical instabilities that the previous design exhibited are now solved with the new cavity geometry. This enabled an improvement of the SWGT performance and, at the same time, an extension of the resonator working range. The prototype described in this thesis was calibrated with a combined standard uncertainty of 3 mK. The uncertainty contribution of the whispering gallery sensor was estimated to be 0.4 mK.

The prototype exhibited a temperature sensitivity of approximately 1 kHz/mK with a resolution lower than 14 μ K and a measurement repeatability of better than 0.4 mK. The measurements carried on in this work confirmed what reported in the literature [1], [32], [56]: the microwave thermometer performs better with respect to the classical platinum resistance thermometer, at least in the investigated temperature range. Nevertheless, the SWGT still suffers from some limitations:

- It is massive with a very high thermal mass. This means that the response time is very big (hours);

- Up to now the SWGT was used in the temperature range from -40 °C up to 100 °C. The SPRTs are usually employed from -200 °C to above 500 °C;
- The expensive VNA should be used for the resonance frequency measurement. On the contrary, a low cost bridge can be used for the resistance thermometer;

Of course these disadvantages limit the SWGT applications. However, they are not crucial and can be partially solved.

The response time is not a critical limitation especially in some metrological applications (e.g., temperature calibrations). It is true that up to now the SWGT was used in a small temperature range, but it does not mean that its working range is restricted. The sapphire melting point (2030 °C) is higher respect to that of the platinum (1768 °C). In the work described in this thesis, the lower and upper temperature limits were set by some materials and mechanical features, e.g., the O-Ring materials (from -45 °C to 200 °C) and the coaxial cables (from -40 °C to 125 °C). By using metallic O-Rings and high temperature range cables or waveguide, it would be possible to cover the whole SPRT temperature range.

Another limitation is related to the instrumentation employed. A VNA is an expensive instrument (20/30 k€), however it is possible to develop an ad-hoc hardware [64], [65] whose price is orders of magnitude lower. The price of a good resistance bridge (accuracy of 8 mK) for the SPRT measurement is approximately 1000 / 2000 €, but if a higher accuracy is needed, the bridge price can overcome the 50 k€ (e.g., ASL F900, see section 2.5.3). So, for very accurate temperature measurements, the SWGT is cheaper than the SPRT.

Although is not always convenient to replace the SPRT with a microwave resonator, in some applications the use of a SWGT can bring some advantages. For instance, it can be employed in the laboratory to replace the fixed point calibration. The results presented in section 2.5.4 proved that the relationship between SPRT resistance and SWGT resonance frequency can be modelled as a 5th order polynomial function with very small residuals (< 0.2 mK) in a wide temperature range. If the SWGT resonance frequency at fixed points is known, the same temperatures can be reproduced in a thermostatic bath recording the resistance values of SPRT. From this readings it is possible to calibrate the platinum thermometer according the ITS-90 standards [59]. This, procedure can significantly reduce the SPRT calibration time and cost.

Chapter 3

Sensor-Integrated Aperture Coupled Patch Antenna for Humidity Measurements

3.1 Introduction

Microstrip resonators exhibit a very low quality factor (100 – 300), however their fabrication is cheap. Usually they are employed as sensors in low cost applications or when measurement accuracy is not an issue. The biggest advantage in using microstrip sensors is that they are intrinsically compatible with the wireless technology.

Nowadays, many objects used in everyday life are combined with sensors. For instance, smartwatches, cell phones and cars host several sensors like accelerometers, magnetometers, proximity sensors or environmental monitoring sensors. Metal oxide semiconductors and nanomaterials [66]–[71] are employed in the development of new sensors designed for healthcare, air quality monitoring or in industrial manufacturing. Usually, the technology behind such sensors is based on microwave measurements. Microwave resonators, or antenna-based sensors are becoming more attractive during the past years, they exploit the change in the resonant frequency, e.g., as an indicator for the gas detection [72]–[78]. Moreover, they can rely on fast response time and small power consumption in comparison with the other categories and their fabrication cost is very low. Microwave resonators can be used at ambient temperature and they can be easily integrated into a WSN by combining the sensing element, the antenna and the electronic board into a single device (sensing node).

When a sensor is included in a wireless sensor node, it needs to be coupled to an antenna. The major problem in the integration process is that usually the antenna is loaded by the sensing element and is detuned out of its working bandwidth. Moreover, power gain, return loss and radiation pattern are often affected by the

presence of the sensor and the overall performance of the sensing node are reduced. The integration of a sensing element into antennas is widely described in the literature [72]–[77]. For instance, novel antenna designs using a carbon nanotube (CNT) based sensing material, have been studied as gas sensors using the return loss variation [73] or the resonance frequency shift [72]–[75] as a marker. However, after the sensing material deposition the radiation efficiency is reduced from 99 % to 50 % with a frequency shift of about 200 MHz [74], [75]. The shape and position of the integrated sensor should be designed such that a low mutual coupling is established between the antenna and the sensing element.

Usually, a microwave gas sensor is made by a resonant structure, such as a disk or an IDC, covered by a sensing material. When the sensor is exposed, the target gas is adsorbed on the surface of the sensing material changing the surface permittivity. As a consequence, the resonant frequency varies so that it is possible to relate the frequency shift to the concentration of the gas target.

In this chapter, a novel design for a microwave gas sensor is proposed. It overcomes the antenna lowering performance that emerges after sensor integration. In particular, an interdigitated capacitor (IDC), acting as a sensing element, is coupled to a rectangular patch antenna through an aperture in the ground plane so that a low mutual coupling is established between the antenna and the interdigitated structure. It was proved [79] that, because of this weak coupling, the antenna performances are not affected by the sensor and, on the other hand, the sensor properties are not compromised by the presence of the antenna. The design of the Aperture Coupled Patch (ACP) antenna is reported in the next section.

After its design and fabrication, the sensor integrated antenna was tested and the experimental measurements were compared with the simulation results. Afterwards, a sensing material was deposited on the IDC so that a variation in the material permittivity was transduced into a variation of the antenna resonant frequency. The design and fabrication of such a novel sensor integrated ACP antenna is reported. The combined system was tested as a water vapour sensor at different temperatures and relative humidity.

3.2 Antenna design and fabrication

Pozar in 1985 introduced for the first time the ACP antennas [80]. Unlike the classical coupling of printed antennas, in which a microstrip feedline is directly connected to the patch radiator, the aperture coupling involves two different substrates separated by a ground plane. The antenna element is placed in the first substrate, coupled through a small aperture in the ground plane to a feedline, placed in the second substrate. The geometry is represented in Figure 44 and it has been employed in several applications [81], [82].

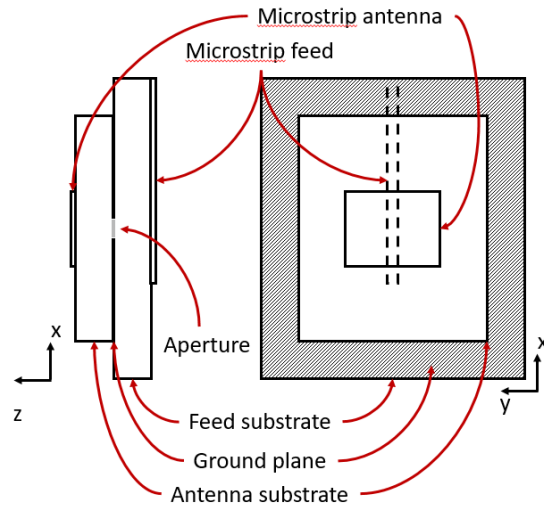


Figure 44 Side view and top view of an ACP antenna coupled to a microstrip line

This configuration ensures some advantages [80]:

- Since the antenna and the feeding network are in two different substrates, it is possible to optimize the antenna for a particular substrate and design the feeding network in another substrate (usually with a higher dielectric constant).
- Because of the ground plane between the two substrates, the main radiation pattern of the antenna is not compromised by the radiations from the feed network.
- A direct connection of the antenna with the feedline is avoided. In this way, problems like large probe self-reactance or wide microstrip lines respect to the antenna size are avoided.

The first study of a sensor integrated into an ACP antenna is reported in [83]. In that paper some electromagnetic simulations were carried out considering an interdigitated capacitor at the end of the microstrip line, covered by a sensing material modelled as a surface impedance. The results from simulations proved that a good isolation was reached between the IDC and the antenna. Nevertheless, no measurements on a fabricated prototype were reported.

In this piece of work, the design of sensor-integrated ACP antenna is carried out and reported. The configuration employed is very similar to that used in [79]: an IDC is designed as a sensing element at the end of the feeding line, just behind the rectangular radiator. The antenna was designed to work in the ISM band (2.45 GHz) on Rogers RO4003C substrate (thickness $h = 1.52$ mm, $\epsilon_r = 3.38$, $\tan\delta = 0.0027$). The antenna length (L_a) and width (W_a) were calculated from the following equations [84]:

$$W_a = \frac{c}{2f_0 \sqrt{\frac{\epsilon_r + 1}{2}}} \quad (3.1)$$

$$L_a = \frac{c}{2f_0\sqrt{\epsilon_{eff}}} - 0.824h \left(\frac{(\epsilon_{eff} + 0.3) \left(\frac{W_a}{h} + 0.264 \right)}{(\epsilon_{eff} - 0.258) \left(\frac{W_a}{h} + 0.8 \right)} \right) \quad (3.2)$$

Where ϵ_{eff} is defined as [84]:

$$\epsilon_{eff} = \frac{\epsilon_r + 1}{2} + \frac{\epsilon_r - 1}{2} \left[\frac{1}{\sqrt{1 + 12 \left(\frac{h}{W_a} \right)}} \right] \quad (3.3)$$

It is the effective dielectric constant of the substrate (see Chapter 1).

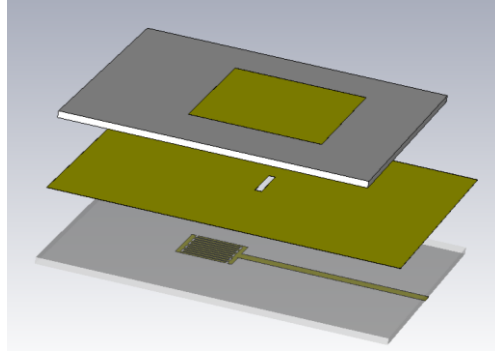


Figure 45 ACP Antenna in the computer simulator (3D exploded view)

The antenna design consists of two RO4003C substrates: one of them hosting a rectangular patch antenna and a ground plane with a rectangular aperture, the other one is characterized by a microstrip line (feed line) ended with an IDC and a ground plane with an aperture. Similarly to [79], the IDC was placed at the end of the feedline, approximately a quarter wavelength far from the aperture center. This guarantees a low mutual coupling with the antenna element [79] reducing the detuning effect after the gas exposure (Figure 46). The two substrate are joint together so that the ground planes are in contact each other with the two apertures perfectly aligned. The rectangular aperture in the ground plane couples the microstrip line to the rectangular antenna placed in the other substrate. The classical coupling for rectangular patch antennas is made with a direct connection of the microstrip line to the patch radiator, however this configuration is not suited for a sensor integrated antenna [12]. A weak coupling is needed between the feedline and the patch so that after the sensing material deposition on the IDC surface, the radiation pattern, power gain and return loss are not compromised.

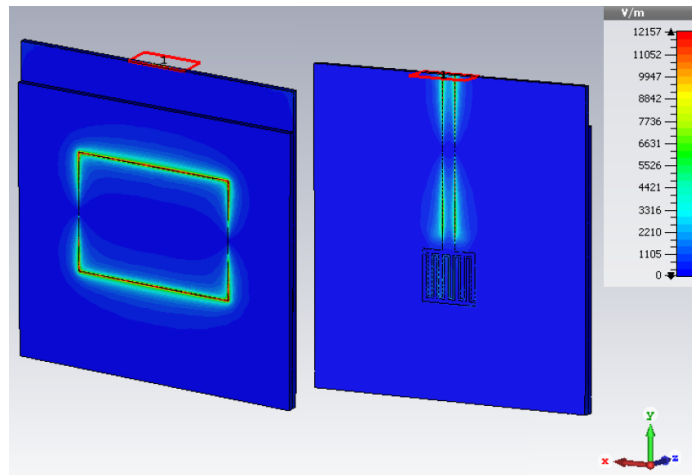


Figure 46 Simulation results: Electric energy density on rectangular patch and IDC at 2.45 GHz. The electric energy density is higher along the patch radiator boundaries and the feedline. On the contrary, its value is low between the IDC fingers because of the weak coupling.

The IDC represents the sensing element. For gas sensors, once a sensitive material is deposited between its fingers, the adsorption of gas molecules on the material surface will change its effective permittivity. Because of the coupling with the patch radiator, this is transduced to a shift in the antenna resonant frequency and the shift amount is related to the gas target concentration.

A first design for the ACP antenna was made starting from Eq. 3.1-3 and then all the dimensions were optimized using finite element electromagnetic simulations. CST Studio Suite was used for this scope. A 3D model for the ACP antenna + IDC was created and loaded into the computer simulator. The boundary conditions were set to “open – add space” in order to simulate a free space neglecting the reflections of the environment. The selected background was “Normal”, that in CST stands for vacuum ($\epsilon_r = 1$, $\mu_r = 1$). The “Copper” material was used for all the metallization and a lossy “RO4003C” for the substrate material. The “Frequency Domain Solver” was chosen with a tetrahedral mesh for both antenna and substrate. A finer mesh was selected for antenna, microstrip and IDC, while the background was modelled with a rougher mesh in order to reduce the computational cost.

For the dimensions’ optimization, the “parameter sweep” tool was employed. Width and length for rectangular patch and slot aperture were optimized for the highest return loss at resonance frequency. The microstrip line was designed for an input impedance of 50Ω while the IDC dimensions were optimized compatibly with the resolution of the CNC used for its fabrication. The main prototype dimensions after the optimization process are reported in Table 8 [12].

Table 8 Prototype dimensions after the optimization process

<i>Parameter</i>	<i>Dimension (mm)</i>
Substrate width / length	75 / 80
Rectangular patch width / length	30 / 41
Microstrip line width / length	3.3 / 40
IDC finger width / length	1 / 11.5
IDC finger pitch	1.5
Aperture width / length	1.5 / 12.4

The computer simulator found a resonant frequency for the antenna of 2.453 GHz with a return loss of 54.65 dB, a radiation efficiency of -0.77 dB and a realized gain of 6.35 dB. The input impedance was estimated to be 49.9 Ω . The main simulation results are summarized in table 3.2 [12].

Table 9 ACP + IDC simulation, main results

<i>Parameter</i>	$\varphi = 0^\circ$ (xz plane)	$\varphi = 90^\circ$ (yz plane)
Main lobe magnitude (Realized Gain)	6.35 dB	6.35 dB
Main lobe magnitude (Directivity)	7.12 dBi	7.12 dBi
Main lobe direction	0.0°	-1.0°
Angular width (3 dB)	80.9°	84.9°
Side lobe level	-18.5 dB	-18.2 dB

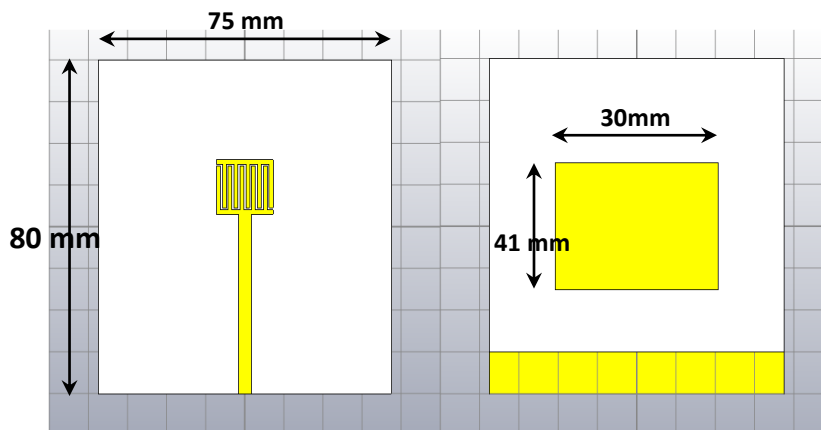


Figure 47 IDC + ACP antenna 3D model, bottom view (left) and top view (right)

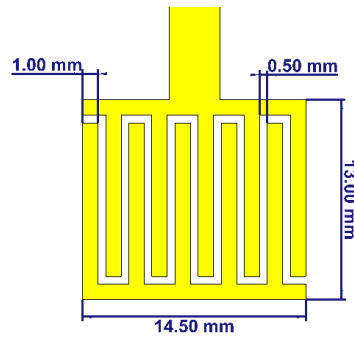


Figure 48 Integrated IDC dimensions

After the design and optimization procedure, the two boards constituting the ACP+IDC prototype were fabricated by using the PCB milling machine LPKF Protomat S103 and an SMA connector was soldered at the end of the microstrip line as excitation port. A plastic frame was also realized with a 3D printer, it allows joining the two boards together, as described in the previous paragraph, with the two apertures in the ground plane aligned in order to reach the highest return loss. Some screws in the plastic frame allows moving one board respect to the other along the x and y direction and, finally, set them in the best position in terms of return loss. According to the simulations performed, while the antenna resonant frequency is related to the patch size, the return loss is strongly influenced by the alignment of the two boards (or by the slot aperture size and positioning). A photo of the fabricated prototype and its frame is reported in Figure 49 and Figure 50.



Figure 49 Fabricated prototype. Top view and bottom view of each board.

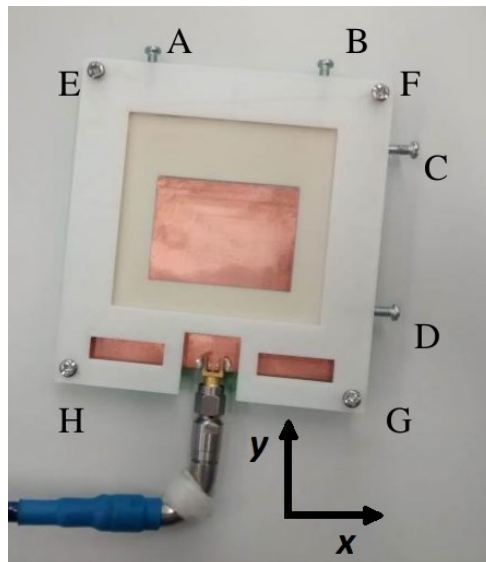


Figure 50 ACP Antenna into its plastic frame. The two screws A and B move the antenna substrate along the y direction. Screws C and D move the antenna along the x direction. Screws E, F, G, H are used to stop the two substrates in the position chosen.

After its fabrication, the prototype was tested using a VNA. Before the measurement session, the VNA was calibrated using the SOLT (Short-Open-Load-Thru) procedure and was connected to the microstrip SMA connector through a coaxial cable. The reflection coefficient (S_{11}) acquired is reported in Figure 51 with the simulated one. They are in a very good agreement: the return loss is almost the same and the measured resonant frequency is 6 MHz lower, probably because of the tolerances in the fabrication process.

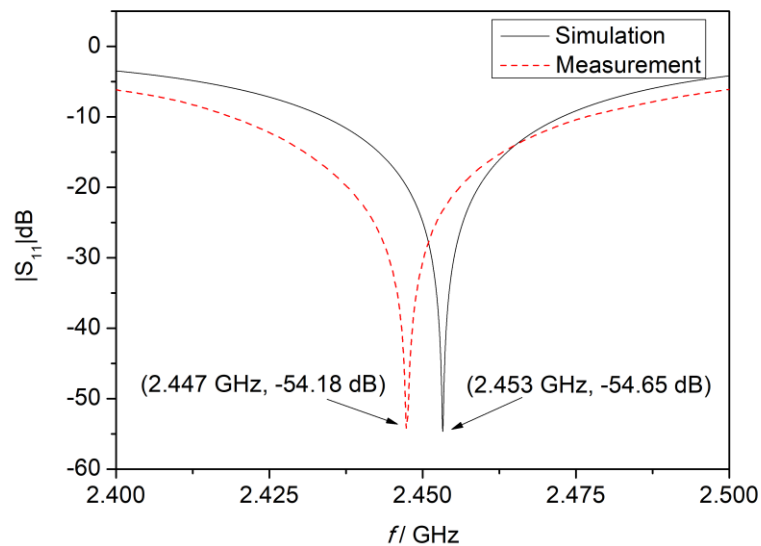


Figure 51 Simulated and measured $|S_{11}|$ at resonance (2.45 GHz).

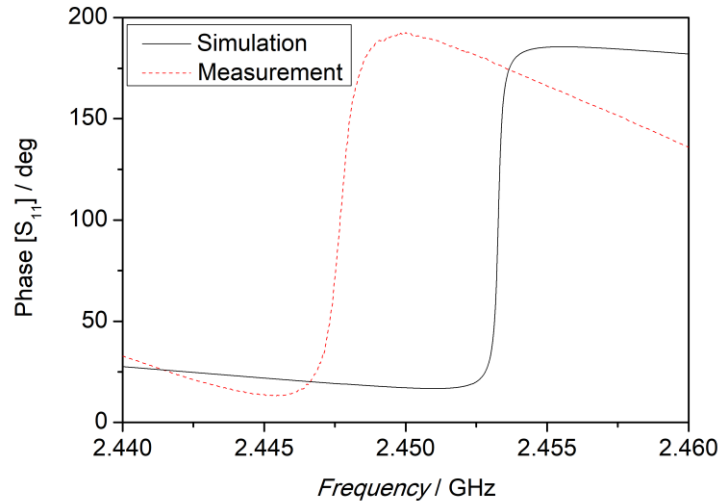


Figure 52 Simulated and measured S_{11} phase at resonance (2.45 GHz)

3.3 Preliminary measurements

The main goal of this piece of work was the development of a novel sensor-integrated antenna working in the ISM band (2.45 GHz) to be employed as a humidity sensor. Before the sensing material deposition (i.e., the sensor functionalization), the prototype was characterized at different temperature and relative humidity concentrations. This preliminary check is useful to highlight the sensing properties before and after the sensing material deposition. Two measurements setups were built for this purpose, one for temperature measurements and another for humidity testing and calibration. The setups are described below.

Humidity measurements

In order to test the prototype sensitivity to humidity variations, the combined antenna was placed inside a plastic box connected to the humidity generator Thunder Scientific 2500. The antenna temperature was monitored during the entire duration of the test and was 24 °C with a measurement uncertainty of 1 °C. Three different steps of relative humidity (dry air, 50 %rh, 90 %rh) were set, approximately one hour each. In the meanwhile, the antenna resonance frequency was recorded by the ZNB20 R&S VNA through a software very similar to that described in the previous Chapter. Figure 53 reports the results of this preliminary test. It is evident that the IDC + ACP antenna (no sensing material deposited yet) is insensible to humidity variations. A frequency shift of only 200 kHz was observed for a humidity variation from 0 %rh to 100 %rh (at 24 °C), showing a sensitivity of about about 2 kHz / %rh. Total shift correspond to 0.01 % of the operating frequency.

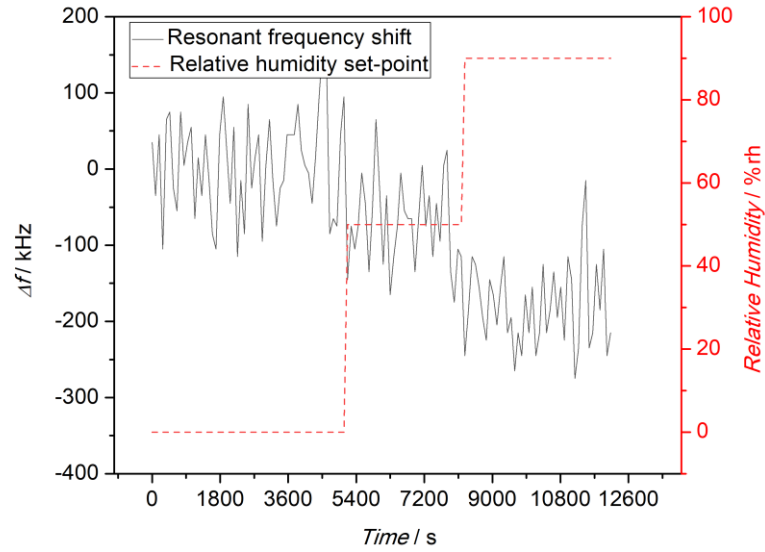


Figure 53 IDC + ACP frequency shift at different humidity concentrations. The shift is relative to the resonant frequency in dry air (0 %rh). This test was carried out at room temperature (24 °C)

Temperature measurements

For the temperature test, the prototype was placed into a foam box in contact with a heater made by a copper plate and connected to a Proportional-Integral-Derivative (PID) controller. A thermometer was placed in contact with the antenna board, far from the patch radiator to avoid interferences. The thermometer employed during this test was a calibrated Pt100 (5-mm diameter) whose resistance was converted into a temperature value using the calibration coefficients reported in the calibration certificate. The antenna resonant frequency was monitored using the ZNB20 R&S VNA at five temperature steps, from 25 °C up to 70 °C. The experimental setup for temperature tests is reported in Figure 54.



Figure 54 Experimental setup for the temperature measurements.

The antenna substrate is in contact with a hot plate connected to a PID controller. Antenna and heater are placed inside a foam box in order to avoid fast temperatures variations.

Unlike humidity measurements, in this test a not negligible temperature sensitivity was observed. It is about 32 kHz/°C. There is not a single explanation to this frequency shift. Certainly as the temperature increases, the thermal expansion increases the patch dimensions thus lowering the resonance frequency (Δf becomes more negative) [85]. On the other hand, a substrate thermal expansion of (11, 14, 46) ppm/°C in (x, y, z) directions, respectively [83] and the thermal coefficient of the dielectric constant (40 ppm/°C) [83] should be taken into account as well. The results for temperature measurements are depicted in Figure 55.

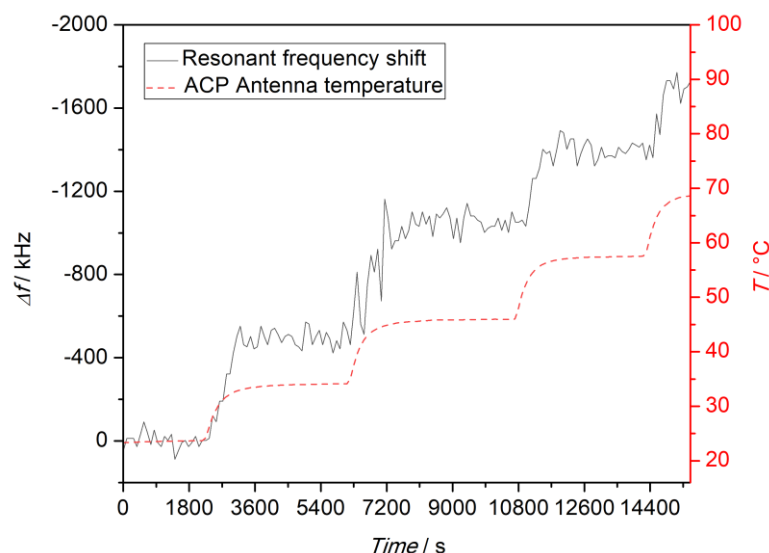


Figure 55 Antenna frequency shift, test at different temperatures. Measurements performed without any sensing material deposited on the IDC

3.4 Sensing material synthesis

After the antenna fabrication, the sensing material was deposited to the IDC surface. A nano-powder of barium titanate with urea coating ($\text{BaTiO}(\text{C}_2\text{O}_4)_2/\text{CO}(\text{NH}_2)_2$) was selected for this project. Its synthesis is similar to that reported in [86], [87].

The $\text{BaTiO}(\text{C}_2\text{O}_4)_2/\text{CO}(\text{NH}_2)_2$ synthesis was made according the following procedure. Barium Chloride (BaCl_2) was added to 300 ml of water whose temperature was 60 °C. The compound was mixed for few minutes in order to stabilize the BaCl (solution A). Another solution (solution B) was made starting from 300 ml of water at 60 °C mixed with oxalic acid ($\text{H}_2\text{C}_2\text{O}_4$). After the solubilisation, the titanium tetrachloride (TiCl_4) was added. The two solutions A and B were finally mixed together for one hour at 60 °C. The product was then filtered, washed with water and placed inside an oven at 80 °C for 12 hours. The dried precipitate was dispersed in a solution of urea (ratio 1/3) and the compound was kept stirring for 30 minutes. Finally, the product was filtered, washed and dried

in oven for 12h at 80 °C. From the reaction, 55 g of barium titanate are created as final product.

A SEM (Scanning Electron Microscopy) analysis of a sample highlighted the presence of agglomerates of nanoparticles whose size is less than 5 µm. These agglomerates have a spherical shape and consist of primary crystals with nanometric size. Afterwards, a TEM (Transmission Electron Microscopy) analysis proved that each crystal was characterized by an inner core made of BaTiO(C₂O₄)₂ and an external amorphous coating of urea with a thickness of 3-5 nm. The material produced looks like white powder.

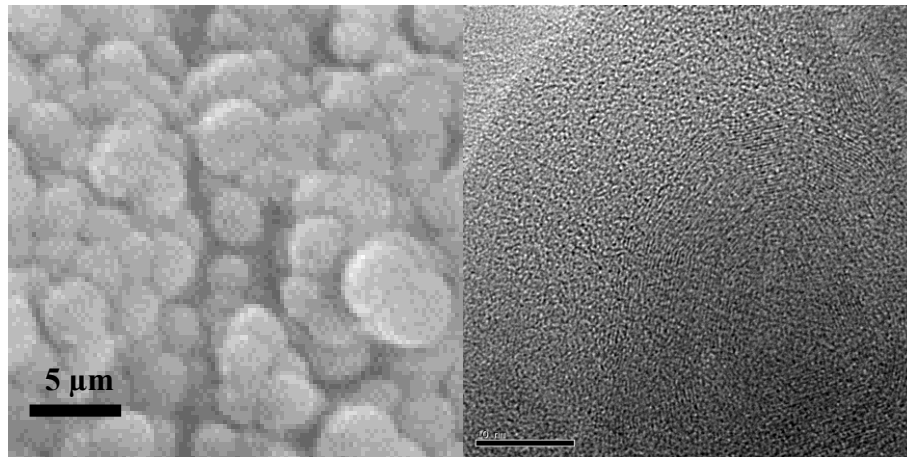


Figure 56 SEM and TEM analysis of the BaTiO(C₂O₄)₂/CO(NH₂)₂ nanoparticles

The material synthesis and analysis was performed at University of Messina by Prof. Giovanni Neri and his team.

3.5 Sensing material deposition and testing

The BaTiO₃ based nano-powder described in the previous section was mixed with water and deposited on the IDC fingers using the drop-coating technique. After the deposition, the excess material was removed so that only the BaTiO₃ between the fingers remained with a thickness of about 35 µm. At the end of the process, the IDC board was dried for about 10 minutes at 80 °C.

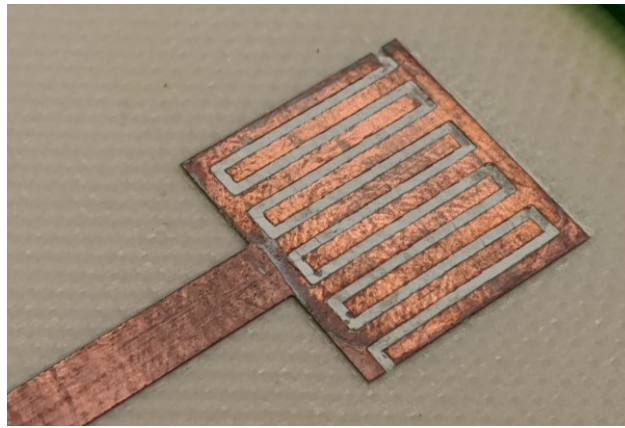


Figure 57 BaTiO₃ nano-powder between the fingers of the IDC

Once the sensing material was deposited at the top of the IDC sensing structure, the sensing properties were evaluated once again by characterizing the prototype in terms of its response to humidity and temperature variation.

The sensor-integrated antenna was firstly tested at different relative levels of humidity by using the same humidity generator employed during the preliminary measurements (Thunder Scientific 2500). Relative humidity was changed in five different steps: 10, 20, 40, 80 and 95 %rh with a constant temperature of 23 °C. The humidity was varied so that the next pulse was approximately two times the previous one; in this way it was possible to evaluate the linearity in the sensor response. At the end of each pulse, the humidity concentration was set to 10 %rh in order to check if the sensor was able to return to its baseline.

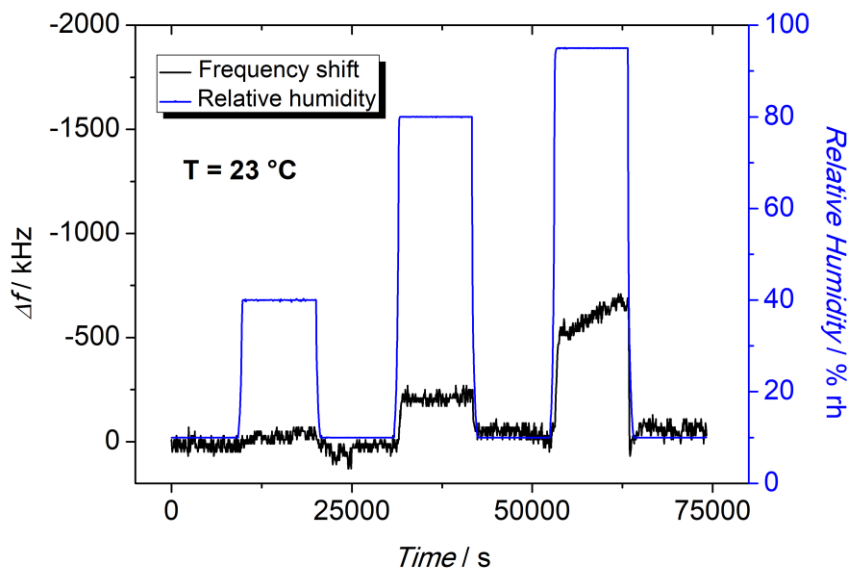


Figure 58 Resonant frequency shift for different humidity concentration values. Measurements carried out at 23 °C

According to the measurements captured in Figure 58, when the relative humidity was lower than 40 %rh, no significant frequency shifts were observed.

For higher humidity, the antenna showed a frequency shift proportional to the relative humidity change. For instance, a shift in the resonant frequency of about 500 kHz was recorded as a consequence of a relative humidity variation between 40 %rh and 95 %rh. This means a sensitivity of about 10 kHz / %rh (considering a linear response). It is evident that the BaTiO₃ on the IDC improved the sensing.

Shifts in the resonant frequency of hundred kHz or few MHz during the detection process proves that the coupling between sensor and antenna is weak, so the antenna is not detuned out of its working band.

The same measurements were repeated at different temperatures, considering the same relative humidity steps (10, 20, 40, 80, 95 %rh). The results are reported in the following plots. For $T = 1\text{ }^{\circ}\text{C}$ no frequency shifts were recorded.

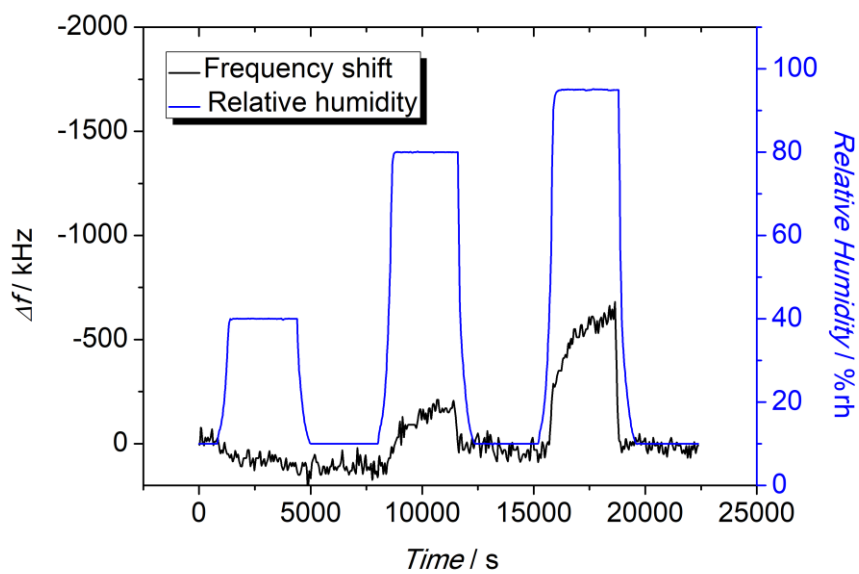


Figure 59 Resonant frequency shift for different humidity concentration values. Measurements carried out at 10 °C

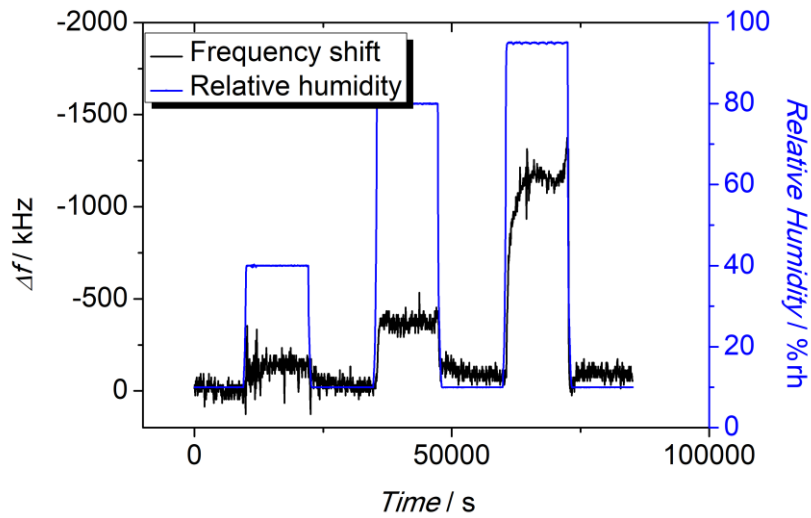


Figure 60 Resonant frequency shift for different humidity concentration values. Measurements carried out at 30 °C

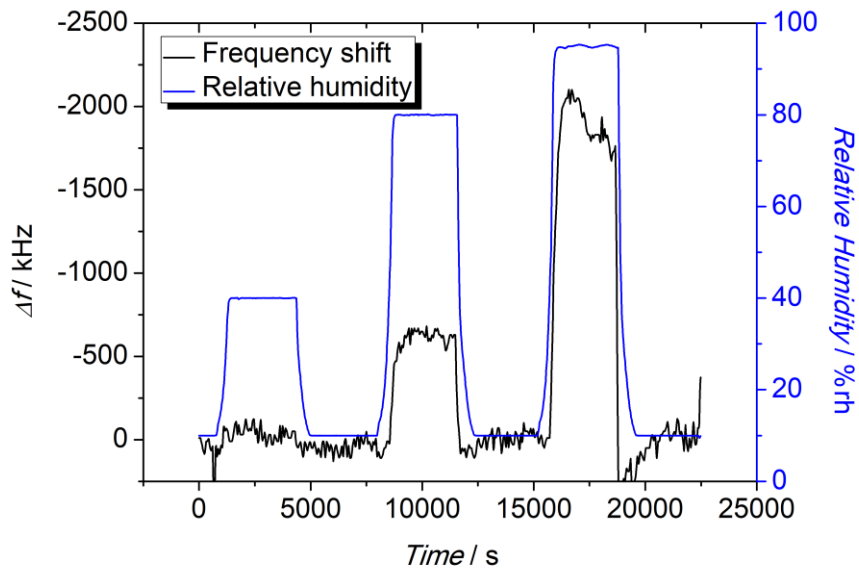


Figure 61 Resonant frequency shift for different humidity concentration values. Measurements carried out at 40 °C

The sensitivity varies with temperature and the reason of this behavior is explained here. When the sensing material is exposed to humid air, the water molecules are adsorbed by the BaTiO₃ sensing material surface thus changing the effective material permittivity. With “effective” we mean that only the material surface is affected by the water molecules, not the bulk. However, it is still possible to consider the material as isotropic with a different permittivity or, in other words, with an effective permittivity. The weak mutual coupling between the IDC and the patch antenna is responsible of the small frequency shift. The higher is the relative humidity at constant temperature, the higher is the number of water molecules

adsorbed on the BaTiO₃ surface. This causes a higher variation in the material permittivity that is converted into a variation of the antenna resonant frequency.

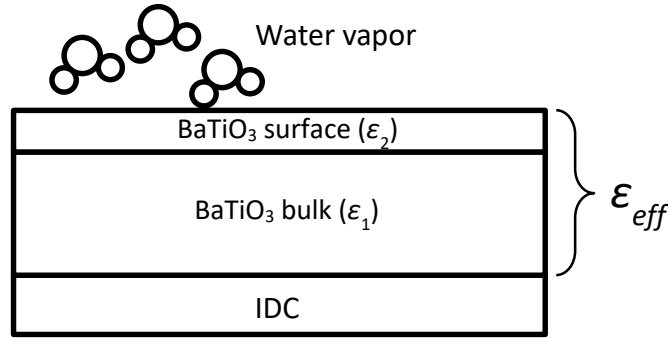


Figure 62 Sensing mechanism schematic

In a gas mixture (e.g., air), the water vapor increases the gas pressure by a certain amount called “vapor pressure”. At a certain temperature, the vapor pressure can increase up to the saturation limit (saturation pressure): this is the point in which the water vapor starts to condensate. The relative humidity is defined as:

$$\%rh = 100 \cdot \frac{P}{P_s} \quad (3.5)$$

Where:

- %rh is the relative humidity value
- P is the partial pressure
- P_s is the saturation pressure at a certain temperature

When the number of water molecules in the gas mixture is constant (P is constant) but the temperature is increasing, the relative humidity decreases because of the dependence of the water vapor saturation pressure with the temperature. This is the reason why the prototype sensitivity increases with the temperature: at higher temperatures for the same %rh values, the number of water vapor molecules in the environment is higher and so, the number of water vapor molecules adsorbed by the BaTiO₃ is higher.

3.6 Data analysis

Data reported in the previous section were used to develop a mathematical model for the description of the sensor prototype. In Figure 63 the resonance frequency variations were reported as a function of the relative humidity. A moving average filter was implemented with a window of ten minutes in order to reduce the noise contribution, this allowed to improve the signal to noise ratio of the measurements. Four different plots are reported, one for each test temperature. Data were fitted with an exponential function of the form:

$$\Delta f = a \cdot \exp(bx) \quad (3.6)$$

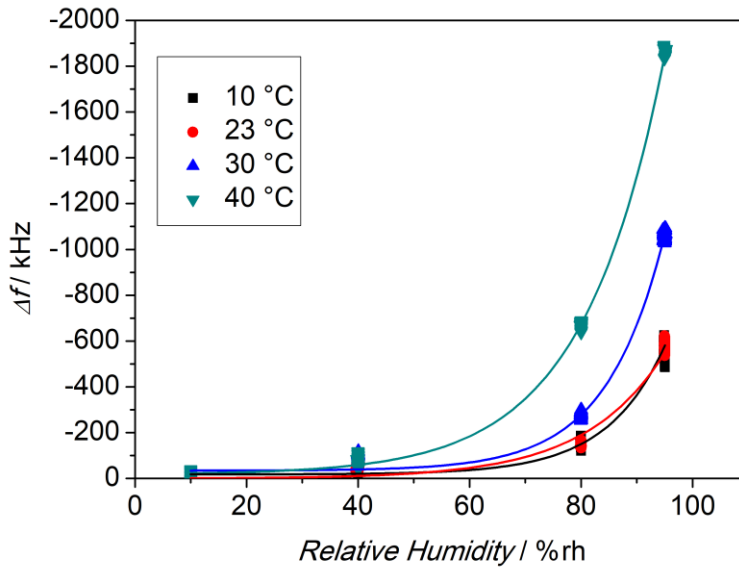


Figure 63 Frequency shift as a function of relative humidity. Each line represents the sensor response at different temperatures. Experimental data fits very good with an exponential function.

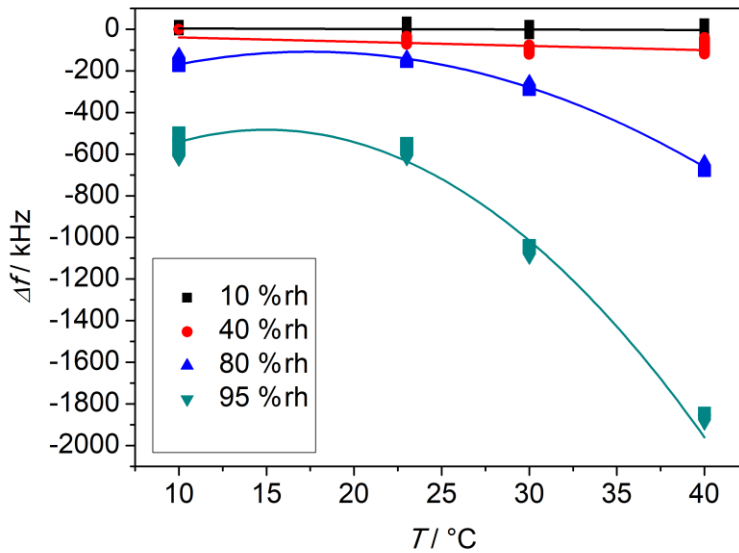


Figure 64 Frequency shift as a function of the operating temperature. Each color represents the sensor response at different relative humidity values.

In Figure 64 the antenna resonance frequency shift is plotted as a function of the temperature. Data points were fitted using a second order polynomial function. For relative humidity lower than 40 %rh, no significant temperature dependence was observed.

After the evaluation of the individual humidity sensitivity and temperature cross-sensitivity, a two dimensional calibration was carried out. The sensing node frequency shift was plotted as a function of the relative humidity (x axis) and temperature (y axis), as shown in Figure 65, and a two dimensional function was used to fit the experimental data. For this purpose, the Levenberg-Marquardt algorithm was employed. The function used in the fitting process can be written as:

$$\Delta f = a \cdot \exp\left(\frac{b}{\%rh} + \frac{c}{f(T)}\right) \quad (3.7)$$

Where:

- a , b and c are three coefficients calculated by the fitting algorithm
- $\%rh$ is the relative humidity value
- $f(T)$ is a function that describes the temperature cross-sensitivity. In this work a second order polynomial function was used.

The fitting curve and the calibration fit residuals are depicted in Figure 65 and Figure 66 respectively.

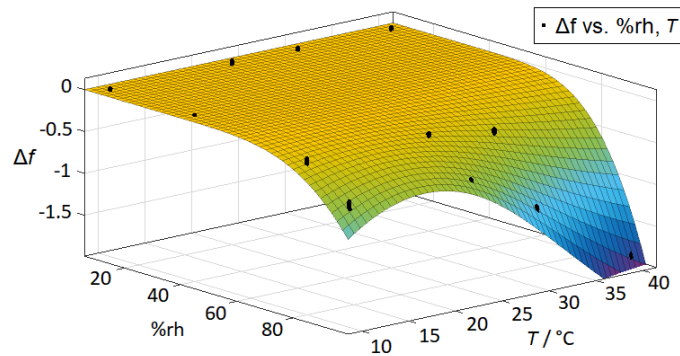


Figure 65 Resonance frequency variations as a function of relative humidity and temperature. A two dimensional calibration function was used to describe the sensor behavior.

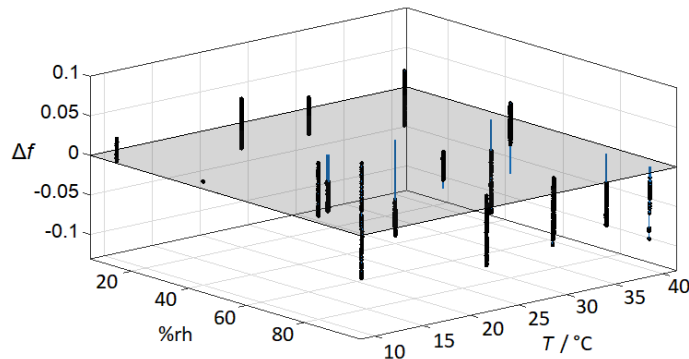


Figure 66 The calibration fit residuals reported in the graph are within ± 0.1 MHz. This value corresponds to approximately 1 %rh ($T = 40^\circ\text{C}$, $\%rh > 40\%$)

The goodness of the fitting (R-square) is 98 % while the Root Mean Squared Error (RMSE) is about 50 kHz, that correspond to 0.5 %rh at $T = 40\text{ }^{\circ}\text{C}$ for %rh > 60 %.

3.7 Conclusions

The design, fabrication and testing of an interdigitated sensor integrated into an ACP antenna is reported. The sensing element was made by an IDC, placed at the end of the antenna feedline, with a BaTiO_3 – based sensing material deposited between its fingers. Measurements carried out during this experiment highlighted the performance sensor after the sensing material deposition. The aperture coupling and the sensing element position ensured a weak coupling between the IDC and the patch radiator. This configuration overcame the antenna detuning issues that characterize the classical configuration. The developed prototype was characterized in terms of relative humidity and cross-sensitivity to temperature variations was evaluated as well. A frequency shift of 2 MHz was observed at $40\text{ }^{\circ}\text{C}$ for a relative humidity change between 10 %rh and 95 %rh. At room temperature, the frequency shift was in the order of few hundred kHz. This relatively small shift in the antenna resonant frequency during the detection process proved the weak coupling between the sensing element and the patch radiator. In other words, the antenna is not detuned out of its working band even after strong variations in humidity and temperature values.

The sensor prototype developed is still under investigation. A further sensor characterization need to be carried out by evaluating the sensing properties (selectivity, hysteresis, detection limits) as well as the antenna performance. However, the promising results reported in here confirm the possibility to use this device for wireless sensor nodes development.

The BaTiO_3 – based nano-powder exhibited an interesting behavior to water vapor adsorption and the change in its effective permittivity was transduced in a resonant frequency shift. However, a different sensing material can be deposited between the IDC fingers making the device selectively sensitive to a particular gas or volatile compound (oxygen, carbon dioxide, acetone). In such a way different kind of sensing node can be developed and potentially employed all together in wireless sensor networks for environmental monitoring.

Chapter 4

Conclusions and future perspectives

Recent developments in microwave sensing technology have resulted in a rapid and significant increase of their potential applications. Microwave sensors are today successfully employed in industrial applications, healthcare and air quality monitoring. They are preferred to other typologies of sensors because, generally, they are characterized by a fast response time, low power consumption and they are relatively low cost. Two examples of microwave sensors are reported in this thesis: the two different devices have been employed in thermal measurements with the aim to give some improvements beyond the State of the Art.

In the first case, a Sapphire-based Whispering Gallery Mode resonator was exploited as a thermometer and its metrological performances were improved compared to the previous prototypes described in the literature. This device is proposed as a good alternative to the SPRT. For this reason, it was compared in terms of performances with the SPRT and from this comparison, the microwave resonator confirmed its high potentials in temperature measurements as highlighted by Strouse in [1]. Because of its high sensitivity to temperature variations and its high measurement resolution, it was presented as a potential interpolating instrument between temperature fixed points, and it could be potentially employed in the SPRT calibration. Besides, the SWGT was also described as a promising substitute to the SPRT in the temperature unit dissemination.

In particular, experimental measurements proved that the microwave resonator performance in terms of measurement repeatability and reproducibility are at least five times better to that of the SPRT. Table 10 reports a comparison between the SWGT and the more classic SPRT. Data reported in the table refers to the experimental measurements carried out in this research activity. Pros and cons in the employment of SWGTs instead of SPRT for temperature measurements were discussed in the second Chapter of this thesis.

Table 10 Comparison between the Sapphire Whispering Gallery Thermometer (SWGTT) and the Standard Platinum Resistance Thermometer (SPRT)

	SWGTT	SPRT
Operating Temperature Range	-40 °C to 150 °C	-200 °C to >500 °C
Response time	minutes	Seconds
Measurement Repeatability	14 μ K	36 μ K
Experimental Reproducibility	0.4 mK	2.3 mK

Alternatively, the SWGT was also described as a good candidate for the thermodynamic temperature scale dissemination. For thermodynamic temperature measurements, a primary thermometer is needed. It is an instrument whose working principle is based on well-known physical laws in which the temperature value can be derived from the measurement of other quantities. Unfortunately, for SWGT there is still no analytical equation that relates the resonant frequency to the sapphire thermodynamic temperature without having to introduce temperature – dependent terms. This means that, at least for now, it is not possible to employ the SWGT as a primary thermometer. The acoustic resonator, for example, is used for this purpose. A more detailed description of this instrument and its working principle can be found in [88]–[90].

Primary thermometers are usually not practical and the measurement process is time consuming, so that the International Temperature Scale provides some procedures for the realization and dissemination the unit in an easier and reproducible way. In 2010, a workshop named “New kelvin dissemination” was held at NPL (National Physical Laboratory, England) with the aim to evaluate the implication of the kelvin redefinition for the realization and dissemination of the new temperature unit [91]. One of the possible proposal was to use the SWGT in the temperature range from 80 K to 750 K as a practical temperature standard (secondary thermometer) replacing the conventional platinum resistance that is at the limit of its capability. Research on this side is going on and this thesis set some improvements beyond the State of the Art in the Whispering Gallery Thermometry.

The second microwave device described is a relative humidity sensor integrated into an ACP antenna. In this case, the detuning issue, that affects this kind of devices during the detection mechanism, was solved by reducing the mutual coupling between the sensing element and the antenna. The novel design employed and the

promising preliminary results make this device useful for Internet of Things (IoT) applications.

The number of connected devices is increasing year by year. As shown in Figure 67, in 2014 they were 13 billion and considering their growing trend, in 2022 they will exceed 39 billion [92]. The biggest contribution to this growth is given by IoT devices. These devices are computing systems connected to a wireless network and able to transmit data. It is expected that in 2020 the total spend on such systems will be \$1 trillion, 20 % more than 2018. Of course, the research interest on this topic is increasing as well.

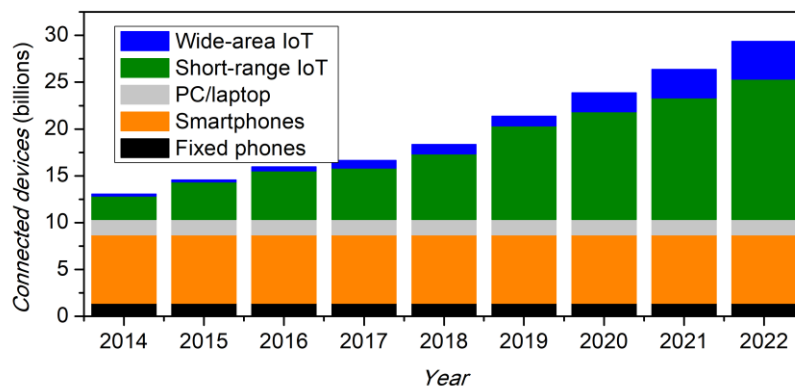


Figure 67 Number of connected devices (billions) between 2014 and 2022. Data from www.ericsson.com.

Microwave sensors have attracted considerable attention also because they are inherently compatible with the wireless technology and they can be easily integrated into a WSN or in IoT devices. In this case the sensing element needs to be coupled to the antenna and the resonance frequency shift is related to the sensor response.

The new sensor-integrated antenna design reported in this thesis helps to overcome the main problems that usually occur after the sensor integration. Among others, the antenna detuning is one of the most important issues that should be taken into account. If a wireless sensing node is designed to work in ISM band (i.e., from 2.4 GHz to 2.5 GHz with a bandwidth of 100 MHz) it is not allowed that, after the sensor integration, the antenna is detuned out of its working band. In this thesis an ACP antenna was employed in order to establish a weak coupling between the patch radiator and the sensing element. The latter was an IDC covered by a nanostructured sensing material placed at the end of the antenna feedline. Through experimental measurements, it was proved that by using this configuration, even after the gas exposure (water vapor) the antenna frequency shift was in the order of hundreds kHz up to few MHz. So the antenna detuning issue was solved. The prototype was characterized in terms of relative humidity variations and the cross-sensitivity to temperature variations was also evaluated. The sensing performances and the antenna properties of the developed prototype are still under investigation. However, the promising results described in this work make this device potentially

useful for IoT applications or as a sensing node in a WSN for environmental monitoring.

References

- [1] G. F. Strouse, ‘Sapphire Whispering Gallery Thermometer’, *Int J Thermophys*, vol. 28, pp. 1812–1821, 2007.
- [2] N. Fitzgerald, *Microwave Theory and Its Application*, vol. 15. 2000.
- [3] D. Pozar, *Microwave Engineering*, 4th ed. .
- [4] G. Galilei, *Dialogues Concerning Two New Sciences*. 1638.
- [5] D. M. Jones and L. Flaxman, *The resonance key: Exploring the links between vibration, consciousness, and the zero point grid*. .
- [6] A. M. Niknejad, ‘Review of Resonance’.
- [7] J. Mazierska, J. Krupka, M. Bialkowski, and M. V. Jacob, ‘Microwave resonators and their use as measurement instruments and sensors’, in *Third IEEE International Workshop on Electronic Design, Test and Applications (DELTA’06)*, 2006, pp. 5 pp.–167.
- [8] E. Nyfors and P. Vainikainen, *Industrial microwave sensors*. IEEE MTT-S Digest, 1991.
- [9] K. Iniewski, *Smart sensors for industrial applications*. CRC Press Taylor & Francis Group, 2013.
- [10] J. Rossignol *et al.*, ‘Development of Gas Sensors by Microwave Transduction with Phthalocyanine Film’, *Procedia Eng.*, vol. 47, pp. 1191–1194, 2012.
- [11] G. Bailly *et al.*, ‘Influence of the Design in Microwave-based Gas Sensors: Ammonia Detection with Titania Nanoparticles’, *Procedia Eng.*, vol. 168, pp. 264–267, 2016.
- [12] G. Gugliandolo, K. Naishadham, N. Donato, G. Neri, and V. Fericola, ‘Sensor-Integrated Aperture Coupled Patch Antenna’, in *2019 IEEE International Symposium on Measurements & Networking (M&N)*, 2019, pp. 1–5.
- [13] *Technique of Microwave Measurements*, First. C. G. Montgomery, 1947.
- [14] S. S. Rao, *The finite element method in engineering*. 2017.
- [15] M. Salazar-Palma, L. E. García-Castillo, and T. K. Sarkar, ‘The finite element method in electromagnetics’, in *European Congress on Computational Methods in Applied Sciences and Engineering, ECCOMAS 2000*, 2000.
- [16] W. C. Gibson, *The method of moments in electromagnetics*. 2007.
- [17] L. P. Hansen, ‘Method of Moments’, in *International Encyclopedia of the Social & Behavioral Sciences*, 2001.
- [18] L. Zipser and A. Peter, ‘Binary gas sensor based on acoustic cavity resonator’, *Procedia Eng.*, vol. 5, pp. 1478–1481, 2010.
- [19] V. Etxebarria *et al.*, ‘Very High Sensitivity Displacement Sensor Based on Resonant Cavities’, *IEEE Sens. J.*, vol. 10, no. 8, pp. 1335–1336, Aug. 2010.

- [20] R. Cuccaro, ‘Hygrometric applications of microwave quasi-spherical resonators’, Politecnico di Torino, 2012.
- [21] A. V. Praveen Kumar and A. K. Ojha, ‘A Microstrip Coupled Cylindrical Dielectric Resonator as a Displacement Sensor’, *IETE J. Res.*, pp. 1–7, Mar. 2019.
- [22] Q. Wang *et al.*, ‘High-Sensitivity Dielectric Resonator-Based Waveguide Sensor for Crack Detection on Metallic Surfaces’, *IEEE Sens. J.*, vol. 19, no. 14, pp. 5470–5474, Jul. 2019.
- [23] A. Iqbal, A. Smida, O. Saraereh, Q. Alsafasfeh, N. Mallat, and B. Lee, ‘Cylindrical Dielectric Resonator Antenna-Based Sensors for Liquid Chemical Detection’, *Sensors*, vol. 19, no. 5, p. 1200, Mar. 2019.
- [24] H. Hallil, P. Menini, and H. Aubert, ‘Novel millimeter-wave gas sensor using dielectric resonator with sensitive layer of TiO₂’, in *2009 IEEE Sensors*, 2009, pp. 226–228.
- [25] C. Lemieux-Leduc, R. Guertin, M.-A. Bianki, and Y.-A. Peter, ‘Gas Sensing with SU-8 Whispering Gallery Mode Resonators’, in *2018 International Conference on Optical MEMS and Nanophotonics (OMN)*, 2018, pp. 1–2.
- [26] V. R. Dantham, S. Holler, V. Kolchenko, Z. Wan, and S. Arnold, ‘Taking whispering gallery-mode single virus detection and sizing to the limit’, *Appl. Phys. Lett.*, 2012.
- [27] R. P. Mann *et al.*, ‘Whispering Gallery Mode Biosensor’, in *Encyclopedia of Nanotechnology*, 2012.
- [28] G. C. Righini and S. Soria, *Biosensing by WGM microspherical resonators*. 2016.
- [29] A. Weller, F. C. Liu, R. Dahint, and M. Himmelhaus, ‘Whispering gallery mode biosensors in the low-Q limit’, *Appl. Phys. B Lasers Opt.*, 2008.
- [30] S. Arnold, S. I. Shopova, and S. Holler, ‘Whispering gallery mode bio-sensor for label-free detection of single molecules: thermo-optic vs reactive mechanism’, *Opt. Express*, 2010.
- [31] H. Hallil, P. Ménini, and H. Aubert, ‘New microwave gas detector using dielectric resonator based on a Whispering-Gallery-Mode’, in *European Microwave Week 2009, EuMW 2009: Science, Progress and Quality at Radiofrequencies, Conference Proceedings - 39th European Microwave Conference, EuMC 2009*, 2009.
- [32] L. Yu and V. Fernicola, ‘Spherical-sapphire-based whispering gallery mode resonator thermometer’, *Rev. Sci. Instrum.*, vol. 83, no. 9, pp. 2–7, 2012.
- [33] E. Nyfors, *Cylindrical microwave resonator sensors for measuring materials under flow*. 2000.
- [34] H. L. Callendar, ‘On the Practical Measurement of Temperature’, 1887.
- [35] R. Price, ‘The Platinum Resistance Thermometer’, *Platin. Met. Rev.*, vol. 3, no. 3, pp. 78–87, 1959.
- [36] Z. Ahmed *et al.*, ‘Towards Photonics Enabled Quantum Metrology of Temperature, Pressure and Vacuum’, Mar. 2016.
- [37] P. B. Welander, M. Barmatz, and I. Hahn, ‘A new small nano-Kelvin resolution thermometer for low temperature experiments’, presented at the Conference Record - IEEE Instrumentation and Measurement Technology Conference, 2000, vol. 49, p. 3.
- [38] W. Weng, J. D. Anstie, T. M. Stace, G. Campbell, F. Baynes, and A. N. Luiten, ‘PHYSICAL REVIEW LETTERS’, *Nano-Kelvin Thermometry and Temperature Control: Beyond the Thermal Noise Limit*, vol. 112, p. 5, 24-Apr-2014.

- [39] D. V. Strelakov, C. Marquardt, A. B. Matsko, H. G. L. Schwefel, and G. Leuchs, ‘Journal of Optics’, *Nonlinear and quantum optics with whispering gallery resonators*, 16-Nov-2016.
- [40] M. Ornigotti and A. Aiello, ‘Theory of Anisotropic Whispering Gallery Resonators’, pp. 1–16, 2011.
- [41] J. W. Strutt, *Theory of sound*. 1877.
- [42] M. R. Foreman, J. D. Swaim, and F. Vollmer, ‘Whispering gallery mode sensors’, *Adv. Opt. Photonics*, vol. 7, no. 2, p. 168, Jun. 2015.
- [43] C. G. B. Garrett and W. L. Bond, ‘Stimulated emission into optical whispering modes of spheres’, *Phys. Rev.*, vol. 124, pp. 1807–1809.
- [44] H. Quan and Z. Guo, ‘Analytical Solution of Whispering-Gallery Modes’, in *ASME 2007 InterPACK Conference, Volume 1*, 2007, pp. 489–497.
- [45] V. Giordano, P. Y. Bourgeois, N. Bazin, and Y. Kersalé, ‘Simple model for the mode splitting effect in whispering gallery mode resonators’, *19th Eur. Freq. Time Forum EFTF 2005 - Proc.*, vol. 53, no. 10, pp. 124–129, 2005.
- [46] C. Ramella, S. Corbellini, M. Pirola, L. Yu, and V. C. Fericola, ‘Investigations on instability effects in a sapphire-based whispering gallery mode thermometer’, *I2MTC 2017 - 2017 IEEE Int. Instrum. Meas. Technol. Conf. Proc.*, 2017.
- [47] M. E. Tobar, J. Krupka, E. N. Ivanov, and R. A. Woode, ‘Dielectric frequency-temperature-compensated microwave whispering-gallery-mode resonators’, *J. Phys. Appl. Phys.*, 1997.
- [48] L. Yu and V. C. Fericola, ‘Spherical-sapphire-based whispering gallery mode resonator thermometer’, *REVIEW OF SCIENTIFIC INSTRUMENTS*, vol. 83, p. 6, 2012.
- [49] R. Wang, G. Dick, and W. Diener, *Proceedings of the 2004 IEEE International Frequency Control Symposium*. IEEE New York, 2004.
- [50] R. Shelby, J. Fontanella, and C. Andeen, ‘The low temperature electrical properties of some anisotropic crystals’, *J. Phys. Chem. Solids*, 1980.
- [51] S. Corbellini, C. Ramella, L. Yu, M. Pirola, and V. Fericola, ‘Whispering gallery mode thermometry’, *Sens. Switz.*, vol. 16, no. 11, pp. 1–13, 2016.
- [52] J. Krupka, K. Derzakowski, M. Tobar, J. Hartnett, and R. G. Geyer, ‘Complex permittivity of some ultra low loss dielectric crystals at cryogenic temperatures’, *Meas. Sci. Technol.*, 1999.
- [53] ‘R&S ZNB Vector Network Analyzer - Specifications’. Rohde&Schwarz.
- [54] ‘1586 Super - DAQ Precision Temperature Scanner, Extended Specifications’. Fluke Calibration.
- [55] ‘F900 Precision Thermometry Bridge’. ASL.
- [56] S. Corbellini, C. Ramella, L. Yu, M. Pirola, and V. C. Fericola, ‘Whispering Gallery Mode Thermometry’, *Sensors*, vol. 16, no. 1814, p. 13, 2016.
- [57] J. B. Mehl, ‘Analysis of resonance standing-wave measurements’, *The Journal of the Acoustical Society of America*, vol. 64, no. 1523, 1978.
- [58] ‘<https://telegram.org>’.
- [59] ‘Guide to the Realization of the ITS-90 - Platinum Resistance Thermometry’. BIPM.
- [60] L. Yu and V. Fericola, ‘A temperature sensor based on a whispering gallery mode resonator’, *AIP Conf. Proc.*, vol. 1552 8, no. 1, pp. 920–924, 2013.
- [61] G. K. White, ‘Reference materials for thermal expansion: certified or not?’, *Thermochim. Acta*, vol. 218, no. C, pp. 83–99, 1993.

- [62] J. Fischer *et al.*, ‘Present estimates of the differences between thermodynamic temperatures and the ITS-90’, *Int. J. Thermophys.*, vol. 32, no. 1–2, pp. 12–25, 2011.
- [63] R. Underwood *et al.*, ‘Estimates of the difference between thermodynamic temperature and the International Temperature Scale of 1990 in the range 118 K to 303 K’, *Philos. Trans. R. Soc. Math. Phys. Eng. Sci.*, vol. 374, no. 2064, 2016.
- [64] S. Corbellini, C. Ramella, M. Pirola, and V. Fericola, ‘A low-cost instrument for the accurate measurement of Whispering-Gallery resonances up to 19 GHz’, in *Conference Record - IEEE Instrumentation and Measurement Technology Conference*, 2015.
- [65] S. Corbellini, C. Ramella, M. Pirola, V. C. Fericola, and A. Cappella, ‘Low-Cost Instrument for Whispering Gallery Mode Thermometry up to 19 GHz’, *IEEE Trans. Instrum. Meas.*, 2016.
- [66] R. Binions and A. J. T. Naik, ‘Metal oxide semiconductor gas sensors in environmental monitoring’, in *Semiconductor Gas Sensors*, 2013.
- [67] L. Rassaei, F. Marken, M. Sillanpää, M. Amiri, C. M. Cirtiu, and M. Sillanpää, *Nanoparticles in electrochemical sensors for environmental monitoring*. 2011.
- [68] M. I. Baraton and L. Merhari, ‘Advances in air quality monitoring via nanotechnology’, *J. Nanoparticle Res.*, 2004.
- [69] E. Bekyarova, I. Kalinina, M. E. Itkis, L. Beer, N. Cabrera, and R. C. Haddon, ‘Mechanism of Ammonia Detection by Chemically Functionalized Single-Walled Carbon Nanotubes: In Situ Electrical and Optical Study of Gas Analyte Detection’, *J. Am. Chem. Soc.*, vol. 129, no. 35, pp. 10700–10706, Sep. 2007.
- [70] S. Colindres, K. Aguir, F. Cervantes Sodi, L. Vargas, J. Salazar, and V. Febles, ‘Ozone Sensing Based on Palladium Decorated Carbon Nanotubes’, *Sensors*, vol. 14, no. 4, pp. 6806–6818, Apr. 2014.
- [71] D. Ziegler, E. Bekyarova, A. Marchisio, J.-M. Tulliani, and K. Naishadham, ‘Highly Selective Ozone Sensors Based on Functionalized Carbon Nanotubes’, in *2018 IEEE SENSORS*, 2018, pp. 1–4.
- [72] S. Chopra, A. Pham, J. Gaillard, A. Parker, and A. M. Rao, ‘Carbon-nanotube-based resonant-circuit sensor for ammonia’, *Appl. Phys. Lett.*, vol. 80, no. 24, pp. 4632–4634, Jun. 2002.
- [73] Li Yang, Rongwei Zhang, D. Staiculescu, C. P. Wong, and M. M. Tentzeris, ‘A Novel Conformal RFID-Enabled Module Utilizing Inkjet-Printed Antennas and Carbon Nanotubes for Gas-Detection Applications’, *IEEE Antennas Wirel. Propag. Lett.*, vol. 8, pp. 653–656, 2009.
- [74] H. Lee, K. Naishadham, M. M. Tentzeris, and G. Shaker, ‘A novel highly-sensitive antenna-based smart skin gas sensor utilizing carbon nanotubes and inkjet printing’, in *2011 IEEE International Symposium on Antennas and Propagation (APSURSI)*, 2011, pp. 1593–1596.
- [75] H. Lee *et al.*, ‘Carbon-Nanotube Loaded Antenna-Based Ammonia Gas Sensor’, *IEEE Trans. Microw. Theory Tech.*, vol. 59, no. 10, pp. 2665–2673, Oct. 2011.
- [76] M. Dragoman *et al.*, ‘Coplanar waveguide on graphene in the range 40 MHz–110 GHz’, *Appl. Phys. Lett.*, vol. 99, no. 3, p. 033112, Jul. 2011.
- [77] K. Naishadham, E. Bekyarova, and P. Savi, ‘Passive nanotechnology based sensors for the remote detection of environmental pollutants impacting public health’, in *2017 IEEE SENSORS*, 2017, pp. 1–3.

- [78] G. Gugliandolo, A. Mirzaei, M. Bonyani, G. Neri, M. Latino, and N. Donato, ‘Electrical Characterization of Microstrip Resonators Based on Nanostructured Sensing Materials’, 2018, pp. 29–34.
- [79] K. Naishadham, A. Bayat, and P. Savi, ‘Antenna integration with nanotechnology-based thick-film circuits for sensor applications’, in *2017 International Conference on Electromagnetics in Advanced Applications (ICEAA)*, 2017, pp. 1711–1714.
- [80] D. M. Pozar, ‘Microstrip Antenna Aperture-Coupled To A Microstripline’, *Electron. Lett.*, 1985.
- [81] D. M. Pozar, ‘A review of aperture coupled microstrip antennas: History, operation, development, and applications’, *Univ. Mass. Amherst*, 1996.
- [82] M. Civerolo and D. Arakaki, ‘Aperture coupled patch antenna design methods’, in *2011 IEEE International Symposium on Antennas and Propagation (APSURSI)*, 2011, pp. 876–879.
- [83] ‘RO4000 Series High Frequency Circuit Materials - Datasheet’. Rogers Corporation.
- [84] A. Ahamed, Md. Maruf; Bhowmik, Kishore; Suman, ‘Analysis And Design of Rectangular Microstrip Patch Antenna On Different Resonant Frequencies For Pervasive Wireless Communication’, *Int. J. Sci. Technol. Res.*, 2012.
- [85] J. W. Sanders, J. Yao, and H. Huang, ‘Microstrip Patch Antenna Temperature Sensor’, *IEEE Sens. J.*, vol. 15, no. 9, pp. 5312–5319, Sep. 2015.
- [86] W. Wen, X. Huang, S. Yang, K. Lu, and P. Sheng, *The giant electrorheological effect in suspensions of nanoparticles*. 2003.
- [87] X. ping ZHANG, L. li XU, and Q. liang WANG, ‘Electro-rheological Effect of Barium Titanate Particles Coated with Urea and Suspended in Methyl Silicone Oil’, *J. China Univ. Min. Technol.*, 2007.
- [88] L. Pitre, M. R. Moldover, and W. L. Tew, ‘Acoustic thermometry: New results from 273 K to 77 K and progress towards 4 K’, *Metrologia*, 2006.
- [89] L. Pitre, F. Sparasci, D. Truong, A. Guillou, L. Risegari, and M. E. Himbert, ‘Measurement of the Boltzmann constant k_B using a quasi-spherical acoustic resonator’, *Int. J. Thermophys.*, 2011.
- [90] J. B. Mehl, M. R. Moldover, and L. Pitre, ‘Designing quasi-spherical resonators for acoustic thermometry’, *Metrologia*, 2004.
- [91] G. Machin *et al.*, ‘New kelvin dissemination workshop held at NPL on 27-28 October 2010’, in *Metrologia*, 2011.
- [92] ‘Data from www.ericsson.com’.